Coarse-Grained Molecular Monte Carlo Simulations of Liquid Crystal-Nanoparticle Mixtures

by

Grigoriy Kimaev

A thesis
presented to the University of Waterloo
in fulfillment of the
thesis requirement for the degree of
Master of Applied Science
in
Chemical Engineering

Waterloo, Ontario, Canada, 2015

I hereby declare that I am the sole author of this thesis. This is a true copy of the thesis, including any required final revisions, as accepted by my examiners.

I understand that my thesis may be made electronically available to the public.

Abstract

Liquid crystals are a unique and complicated class of phases of matter, also called "mesophases", which exhibit properties such as solid-like elasticity and anisotropy, and liquid-like flow. The industrial application of liquid crystals in display technology has revolutionized our lives. Most notably, it has enabled the development of thin light displays presently found in many portable devices such as digital watches (and smartwatches), cellphones, laptops, desktop computer monitors and large screen televisions. With the recent advances in nanotechnology, liquid crystals have attracted much interest as a medium for dispersing and organizing nanoparticles, the presence of which also alters the properties of the liquid crystal host and gives rise to new composite materials. The possible applications of these new materials reach far beyond displays. However, in order to understand how to design devices based on liquid crystal-nanoparticle mixtures, it is first essential to understand the structure of the latter at molecular resolution. To this end, computer simulation can provide invaluable insights.

This thesis presents a study using a pairwise intermolecular potential capable of describing interactions between liquid crystal molecules and nanoparticles in a liquid crystal-nanoparticle mixture. The so-called Zewdie-Corner potential is a Lennard-Jones type anisotropic pairwise potential where strength (energy scale) and range (length scale) parameters are expanded in terms of an orthogonal basis set of functions with respect to relative orientation and separation distance. This molecular coarse-grained methodology has been employed to represent liquid crystal molecules with cylinder-like shapes and nanoparticles with spherical shapes. Equilibrium structures of domains comprised exclusively of liquid crystal molecules, as well as domains with varying number fractions of liquid crystal molecules and nanoparticles, have been investigated using the Monte Carlo simulation technique in the isobaric-isothermal ensemble. Thermodynamic observables have been calculated and used to draw conclusions as to the molecular-scale structure and thermodynamics of the simulated liquid crystal-nanoparticle mixtures.

Acknowledgements

I would like to thank Professor Nasser Mohieddin Abukhdeir for his persevering guidance and help, Ryan Neufeld for his contributions to the simulation code, post-processing code and many discussions, Fred Fu for his work on domain visualization and contributions to the simulation code, and Tanyakarn Treeratanapitak for her patient responses to my numerous questions about the open-source code base ("SPPARKS", Stochastic Parallel PARticle Kinetic Simulator) upon which my simulation software was developed. Special thanks go to the Natural Sciences and Engineering Research Council of Canada (NSERC) and the Waterloo Institute for Nanotechnology (WIN) for their financial support and to the Shared Hierarchical Academic Research Computing Network (SHARCNET) for the use of their High Performance Computing (HPC) facilities.

Dedication

This is dedicated to my Creator and Redeemer, my immediate family (my mother, my stepfather and my brother), and my Kitchener-Waterloo Seventh-day Adventist church family, all of whom have continuously encouraged me to persevere in my graduate studies. I am also grateful for the example of academic diligence set early in my life by my father.

Table of Contents

List of Tables

List of Figures

Chapter 1

Introduction

Liquid crystal (LC) phases have been utilized to develop a wide variety of technology ranging from displays [1] to tunable lasers [2]. Many different types of LC phases exist where upon cooling from a disordered liquid phase, a phase-ordering transition is observed into a liquid crystalline phase which possesses properties that are both liquid-like (flow) and solid-like (elasticity, anisotropy). Phase-order can involve purely orientational order, called *nematic* LC phases, where molecules conform to an average orientational axis. Phase-order can also include translational order, in addition to orientational order, which include both *smectic* and *columnar* LC phases. Fig. 1.1 shows schematics of molecular order observed in some of the more common LC phases, also known as *mesophases* (given this name because they have properties of both liquids and crystalline solids).

The vast majority of technology applications involving LC mesophases use precisely engineered confining geometries and surface interactions that result in macroscopic liquid crystal structure and dynamics. Recent advances, for example ferroelectric display technology [4], involve applications which utilize the inherent nanoscale structure and dynamics of LC phases. Additionally, recent research advances have attributed the observation of "memory effects" to the presence of nanoscale structure in LC domains [5]. Thus further progress, both fundamental and applied, requires the resolution of both nanoscale structure and dynamics of LC phases. The nanoscale nature of LCs poses serious challenges to direct experimental observation and design of LC phenomena and devices. Subsequently, simulation-assisted design has played a key role in LC display technology advancements over the past decade.

Existing simulation-based design of LC devices has predominantly relied on continuum models, such as the Frank-Oseen director model [6] and the Landau-de Gennes tensor model

Figure 1.1: Schematics of a (left) disordered liquid, (centre) nematic mesophase, and (right) smectic mesophase, taken from [3].

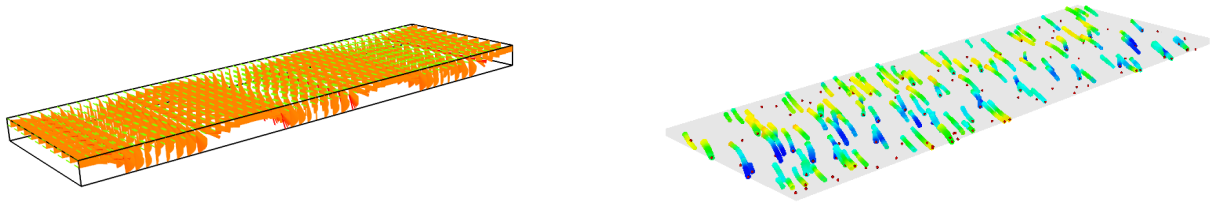

Figure 1.2: Examples of nematic LC simulation results using (left) Frank-Oseen director theory and (right) Landau-de Gennes tensor theory. Figures courtesy of Anindya Mitra.

[7], which are able to bridge the nano-to-macro scales involved in LC phases (Fig. 1.2). These models are phenomenological and thus require the measurement and/or estimation of material properties, many of which are challenging or infeasible to determine through experimental methods. Furthermore, much of LC research is focused in areas where the continuum approximation breaks down, for instance the synthesis of new LC molecules and mixtures of LCs and other compounds such as surfactants and nanoparticles [8].

In order to address these issues and enable truly predictive simulations, more fine-grained theory and methods must be used such as quantum mechanical, atomistic [9] (Fig. 1.3), and coarse-grained molecular simulations [9] (Fig. 1.3). These simulations are, in many cases, truly predictive in nature and able to capture inherently discrete phenomena such as local polarization of mesogens and the formation of nanoparticle (NP) networks. With the enhanced predictive capabilities of microscopic models comes additional compu-

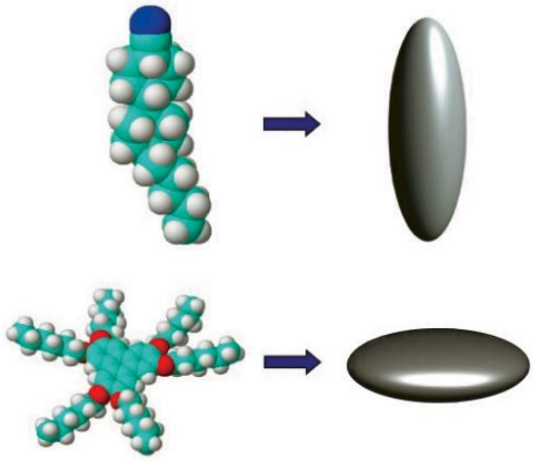

Figure 1.3: Examples of molecular coarse-graining from [10] for (top) rod-like and (bottom) disk-like mesogens.

tational complexity. This is exacerbated for LC phases in that the length scales on which they form, specifically the *coherence length* [7], can be on the order of hundreds of nanometres, which poses significant computational challenges due to the inclusion of hundreds to thousands of molecules in order to resolve LC phases. Thus the most employed microscopic simulation methods involve coarse-grained molecular simulations where molecules are treated as individual particles with the assumption of pairwise interactions [9], as opposed to multi-body interactions. To date, the standard coarse-grained molecular interaction potentials have lacked the flexibility to represent complex molecular interactions predicted through quantum mechanical and/or atomistic simulations.

1.1 Objectives

The overall objective of this research project is to identify and evaluate a suitable coarse-grained molecular interaction potential for the simulation of nanoscale LC structure and phase behaviour. To complete this overall objective, the following specific objectives have been identified:

1. Identification of a coarse-grained pairwise potential which is formulated using an expansion of an appropriate orthogonal basis.

2. Determination of a suitable parameter set for the potential for simulation of liquid crystal-nanoparticle (LC-NP) mixtures.

3. Analysis of the nanoscale structure and phase behaviour of both pure component LCs and LC-NP mixtures for different thermodynamic conditions and mixture compositions.

1.2 Thesis Organization

Chapter 2 provides a brief introduction to LC phases, nanoparticles, and coarse-grained simulation methods for LCs. Chapter 3 provides a review of recent progress in the development of coarse-grained potentials for mesogens and research on LC-NP mixtures. Chapters 4-5 present and discuss the results of the thesis. Chapter 4 presents an appropriate coarse-grained interaction potential, the Zewdie-Corner potential [11], derives a set of parameters representing LC-NP interactions, and presents the results of varying mesogen energetic interactions and formation of LC phases. Chapter 5 presents simulation results for LC-NP mixtures for various thermodynamic conditions and mixture compositions. Finally, Chapter 6 summarizes the conclusions from this research project and discusses possible future work.

Chapter 2

Background

This chapter presents the background knowledge one would need to understand the work conducted in this thesis. We proceed first by discussing what are liquid crystal phases, what types of them are known to exist and what methods are commonly used to analyze them. A brief discussion of nanoparticles follows afterwards. It is succeeded by a summary of common simulation techniques, an outline of how interactions between molecules (isotropic and anisotropic) are described by pairwise potentials, and a discourse on the foundational ideas of Monte Carlo.

2.1 Liquid Crystal Phases

Liquid crystals are a unique and complicated type of condensed matter formally classified as soft matter; rather than being a particular material, they are the fourth phase or state of matter, in addition to solid, liquid and gas. Liquid crystals are found in a vast array of physical systems and substances. A diagram of different areas of liquid crystal science has been presented in figure 2.1.

This fourth phase is thermodynamically stable and it occurs between the transition from liquid to solid and vice versa [12]. Liquid crystals possess optical activity [12] (i.e. they interact with light) and the capability of self-assembly [13, 14] (they arrange themselves in larger functional structures spontaneously). Both of these properties enabled their application in display technology that revolutionized our world and enabled the creation of large and small area displays. Figure 2.2 contains a schematic of a "twisted-nematic" display pixel operation. Because of this combination of properties from liquid and solid

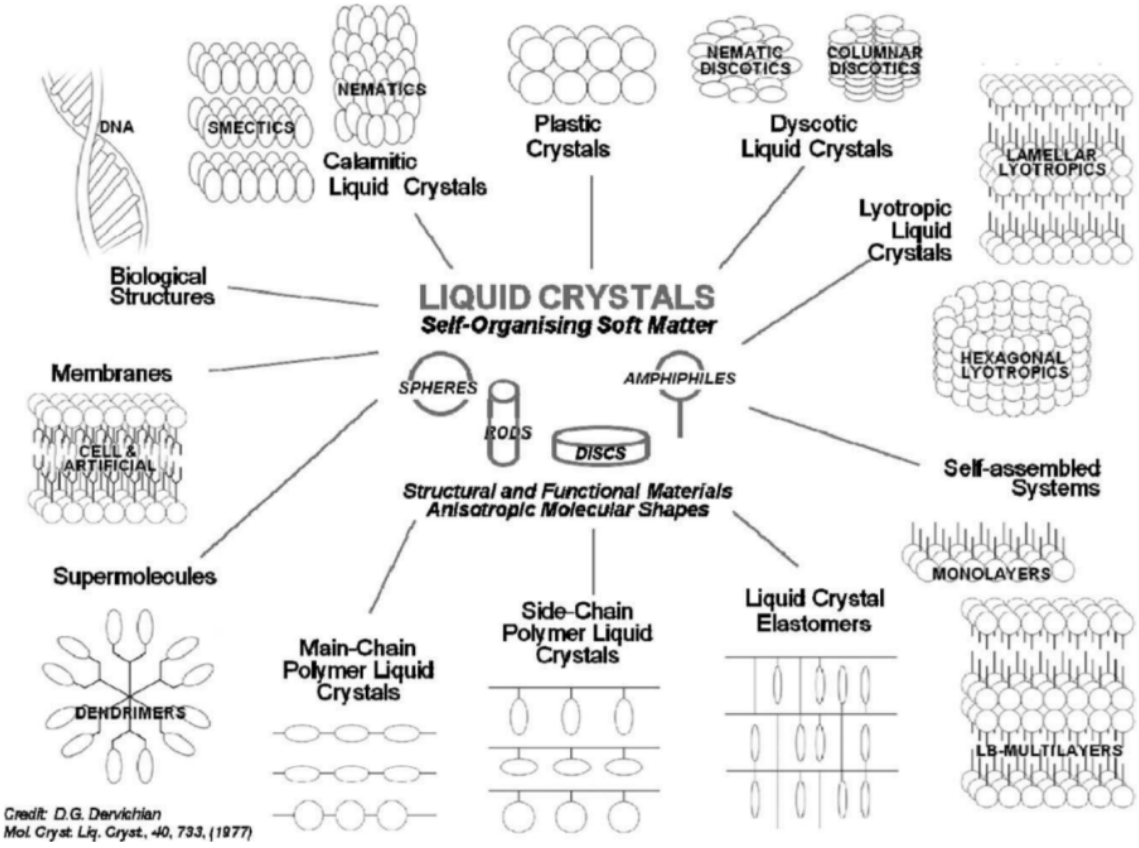

Figure 2.1: Areas of liquid crystal science [16].

phases, liquid crystal phases are called "mesophases" [12] and the molecules of materials that exhibit LC phases are called "mesogens" [15].

As already mentioned, LCs have the flow of liquids, but they also exhibit anisotropic mechanical, optical and electromagnetic properties of solids that arise due to some amount of order (orientational and even positional) still present in LC phases. However, the latent heat of transition from LC phase to isotropic (liquid) phase is about 50 times less than the latent heat of transition from solid to LC [1]; thus, an LC phase contains much less order than the solid (crystal) phase and is closer to a liquid in this respect. Unlike regular liquids, LCs are opaque to light and exhibit various textures under a polarized light microscope (as in figure 2.3). Molecules in an LC phase exhibit a statistically preferred direction as they self-diffuse through the phase. When the directions of all molecules are averaged over the entire sample, the unit vector resulting from this calculation is called

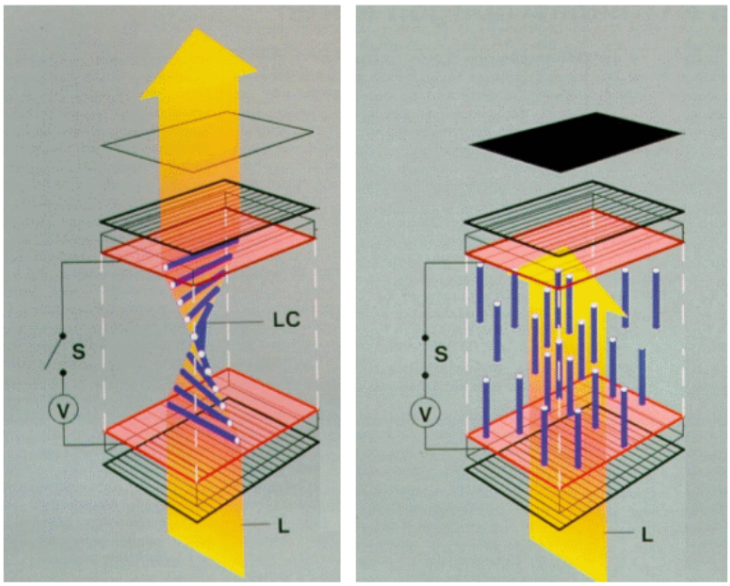

Figure 2.2: Schematic of a "twisted nematic" (TN) display pixel operation from [17]. When no voltage is applied, the liquid crystal domain has a "twist" due to anchoring of the mesogens at each cross polarizer, so that the plane polarized light entering the pixel can be rotated by 90°and exit the pixel, thereby giving the appearance of an "on" state to the pixel. Application of voltage disrupts the "twist" and prevents plane polarized light from going through the output cross polarizer, giving the black colour (appearance of an "off" state) to the pixel.

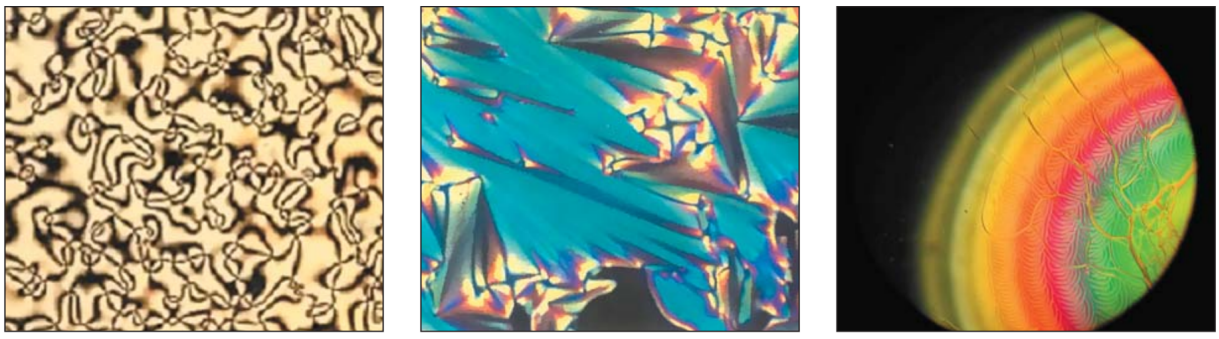

Figure 2.3: Typical liquid crystal textures under a polarized light microscope [18]. From left to right: texture of a nematic, smectic and cholesteric liquid crystals.

Figure 2.4: The director (a unit vector) of a nematic calamitic liquid crystal is represented by **n** [8].

the "director" (schematically represented in figure 2.4). Among those anisotropic properties are the dependence of viscosity on the direction of applied force with respect to the director, and birefringence, which is the dependence of refractive index on direction within the material. A consequence of birefringence is optical retardation - different planes of polarized light will grow out of phase while they propagate through the LC material. Additionally, anisotropy in electric and magnetic susceptibility and permittivity, as well as in polarisation and magnetisation, are exhibited.

Commercialization of materials with LC phases has led to a widespread use of thin displays, both compact and large-scale. However, rapid development of display technology and technology using LCs in general creates a demand for greater understanding of LC phases, especially their molecular structure. Data obtained from computer simulations of mesophases is invaluable to that end [15], because insight into the arrangement of mesogens

within the material is difficult to obtain from laboratory experiments alone. Once the data is obtained, order parameters [19] are used in order to gain information about molecular packing and therefore establish what type of phase was formed by the simulation at the set temperature and pressure.

2.1.1 Types of Mesogens

As a general rule of thumb, to enable the formation of LC phases, mesogens should possess anisotropic shapes with a rigid core (e.g. two aromatic rings joined together) and flexible tails (e.g. alkane chains). Recently it has been shown that LC phases are also exhibited when a flexible spacer carbohydrate chain is used to connect two rigid units made of two benzene rings each (cyanobiphenyls, as in [20]). The balance of attractive and repulsive forces (van der Waals interactions) between the mesogens causes self-assembly to occur, and at the appropriate ambient temperature anisotropy of the shape causes a preferred direction to be adopted by the molecules which then form a thermotropic LC phase (note that when mesogen concentration in a solute plays the key role in forming an LC phase, the phase is called lyotropic).

There are several major types of mesogens that can form LC phases: calamitic, discotic and bent-core mesogens, amphiphilic molecules and polymers (linear and branched) with mesogenic units, as depicted in figures 2.5 and 2.6.

Calamitic mesogens resemble rods by their shapes because one molecular axis is significantly longer than the other two equivalent axes. Some of the most popular ones are 5CB (4-cyano-4´-pentylbiphenyl) and 8CB (4´-n-octyl-4-cyano-biphenyl), shown in figure 2.7. Discotic mesogens are like disks - one molecular axis is significantly shorter than the other two, which are again equivalent to each other. Both calamitic and discotic mesogens are called "uniaxial" since only one axis plays a role in generating the peculiar properties described earlier in this chapter. Polymers with mesogenic units (see figure 2.6) either in the backbone or in the branches (for branched or grafted polymers) are also capable of forming LC phases at certain temperature intervals.

Bent-core mesogens have the "banana" or "boomerang" shape (see figure 2.8) and lower symmetry than cylindrical or disk-like particles [23]; usually the angle of the "bent" core is 120°. If the mesogen is comprised of a rigid core, the core has to be synthesized such that the "banana" shape is present due to how the benzene rings in the core are connected. However, as mentioned a bit earlier, the core can also be a flexible hydrocarbon chain (a flexible spacer) and the rigid biphenyl units can be attached at its ends, and bent-core mesogens will be formed nonetheless [20]. All of their three axes are different, but since

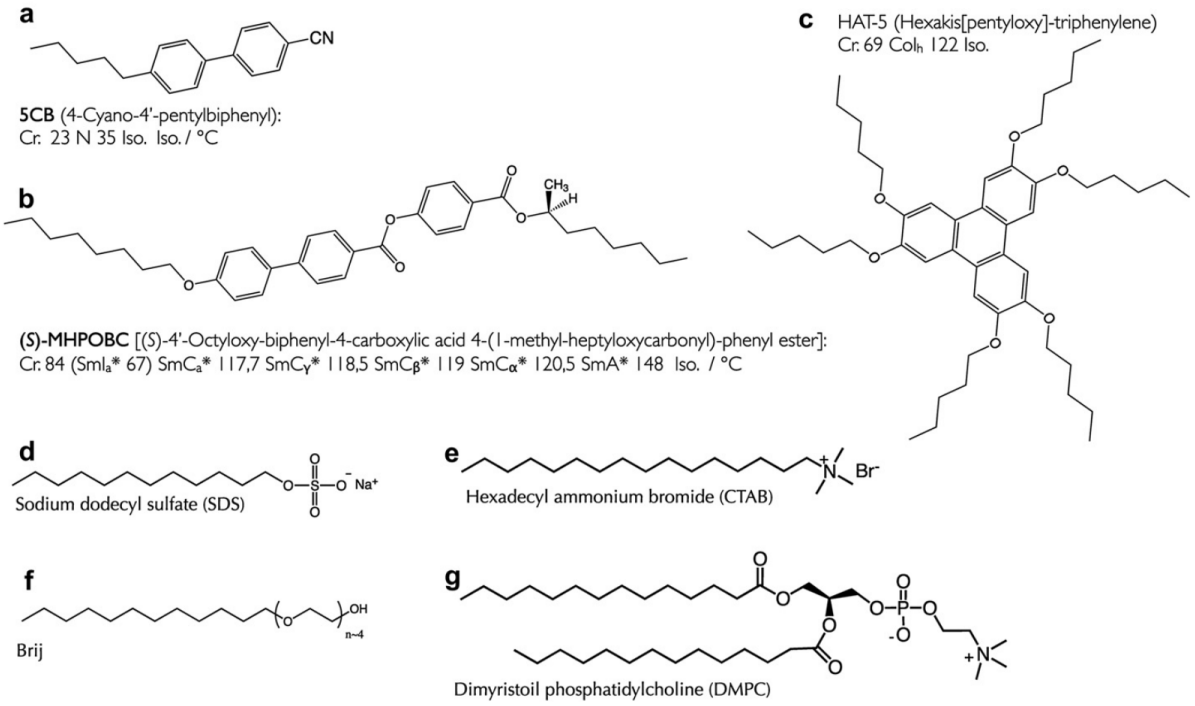

Figure 2.5: Chemical structure of common calamitic, discotic and amphiphilic mesogens [8]. Calamitic thermotropic mesogens are portrayed in **a** and **b**, a discotic mesogen is shown in **c** and **d**-**g** depict amphiphilic mesogens.

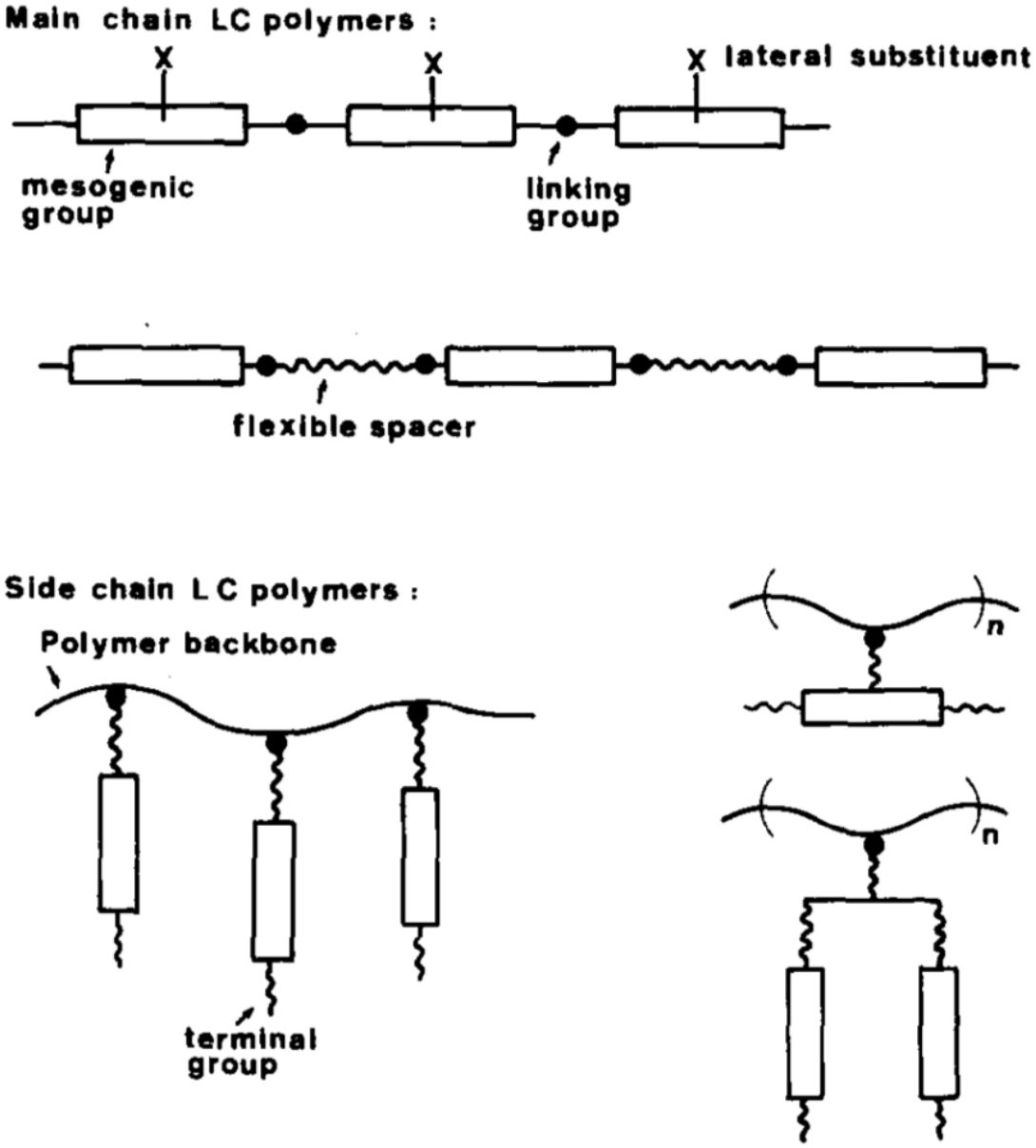

Figure 2.6: Schematics of repeating units of polymers with mesogenic groups [21].

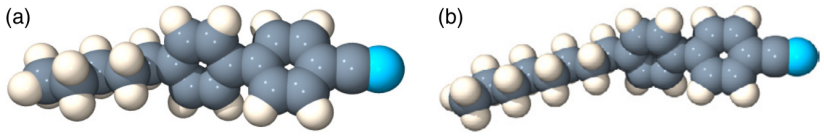

Figure 2.7: Representations of 5CB and 8CB calamitic thermotropic mesogens [15]. 5CB calamitic thermotropic mesogen is portrayed in *(a)* and 8CB in *(b)*.

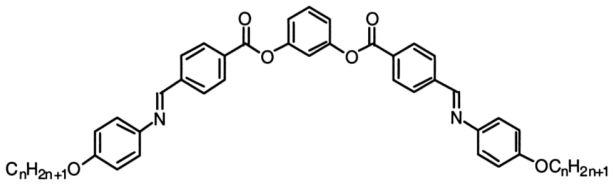

Figure 2.8: Chemical structure of a bent-core mesogen [22].

the cross product of two vectors yields the third vector, they are called "biaxial" rather than "triaxial". These mesogens are of great interest because they have two molecular axes that interact with light, and the rotation of the shorter axis is up to one order of magnitude faster than rotation of the longer axis [24]. Therefore, if this behaviour can be understood and incorporated into commercial devices, a disruptive technological development will be made. This hope is one of the main driving forces in the ongoing attempts to understand biaxial phases.

All four of the aforementioned mesogens form LC phases at certain temperatures, and therefore those phases are called "thermotropic" phases. However, amphiphilic molecules (see figure 2.5, **d**-**g**), most notably those with polar head groups and nonpolar carbohydrate tails (phospholipids) can also form anisotropic phases with liquid-like flow and solid-like properties combined. These phases are called lyotropic; the most important biological example of those is the phospholipid bilayer that comprises the membranes of living cells.

2.1.2 Types of Thermotropic LC Phases

As mentioned just above, when temperature is the key factor for formation of an LC phase, such a phase is classified as "thermotropic". Calamitic mesogens can form nematic and smectic phases depending on their chemical composition and the ambient temperature. Nematic LC phases possess no positional (translational) order, but only orientational order (represented by the director).

Smectic phases are those that have both positional and various degrees of orientational order. While orientational order arises due to the statistically preferred molecular directions, positional order is caused by the variation of the probability of finding molecular centres of mass along the director. In smectic phases, molecules are arranged into layers that are perpendicular to the director. The layer thickness tends to be slightly less than the molecular length due to the interdigitation of layers. For the smectic A phase, molecules are oriented perpendicular to the layers, while in the smectic C phase the molecules are tilted with respect to the layers. By geometric argument, as a result of the tilt layer thickness in the smectic C phase can be less than in the smectic A phase. Figure 2.9 contains simulation snapshots of different thermotropic liquid crystal phases formed by rod-like mesogens.

Discotic mesogens form nematic and columnar phases. In the former, there is only orientational order exhibited by the short axes of the molecules. In the latter, molecules arrange themselves into columns and thus positional order is born as well. In turn, columns pack in hexagonal arrangements. However, other than being arranged into columns and having a preferred orientation, there is no correlation of molecular position with respect to the long axis of the column.

If the mesogens are chiral (i.e. they lack inversion symmetry - their mirror images cannot be superimposed), then a chiral nematic, also called "cholesteric", phase will be formed [1]. In such a phase, the director rotates throughout the sample in a helical fashion [8]. Figure 2.10 depicts the molecular arrangements of such a phase, while figure 2.3 shows the texture of such a phase under polarized light microscope.

2.1.3 Types of Anchoring

When a liquid crystal cell is made for research or industrial purposes, the liquid crystal molecules are aligned with respect to the substrate in one of two ways: homeotropic (perpendicular) and planar (parallel). Both are shown in figure 2.11. Homeotropic anchoring of mesogens towards nanoparticles seems to be the real-world scenario since it is frequently reported in the publications of experimental work [25, 26, 27].

2.1.4 Measurements of Liquid Crystal Domain Order

The nematic (orientational) order parameter is defined [1] as the second order Legendre polynomial dependent upon the dot product ($cos\theta$) of the director $\hat{n}$ (a unit vector) and

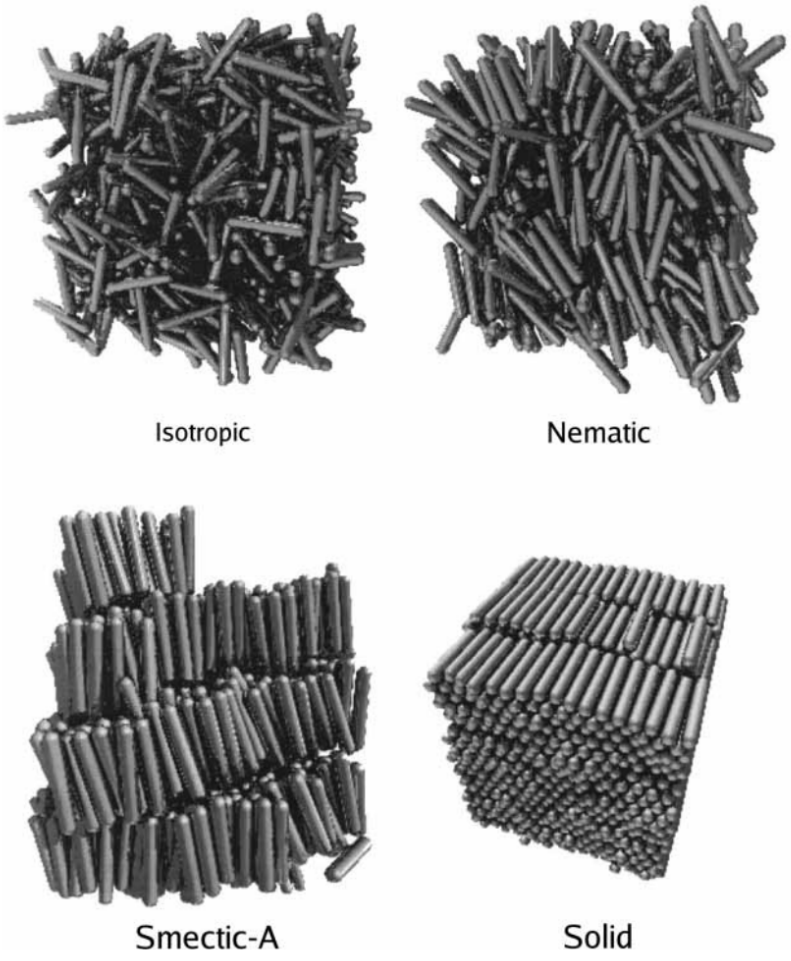

Figure 2.9: Simulation snapshots of thermotropic liquid crystal phases with rod-like mesogens [3]. Upon cooling, the liquid crystal transitions from isotropic liquid to the nematic phase, then to a smectic phase, and eventually freezes into a solid phase. Not all mesogens exhibit both nematic and smectic phases.

Figure 2.10: Molecular arrangements in a chiral nematic ("cholesteric") phase [8] formed by calamitic (left) and discotic (right) mesogens. Note that the drawing is not to scale - in a real system the degree of order would be lower and the pitch of helix-like rotation would be significantly longer.

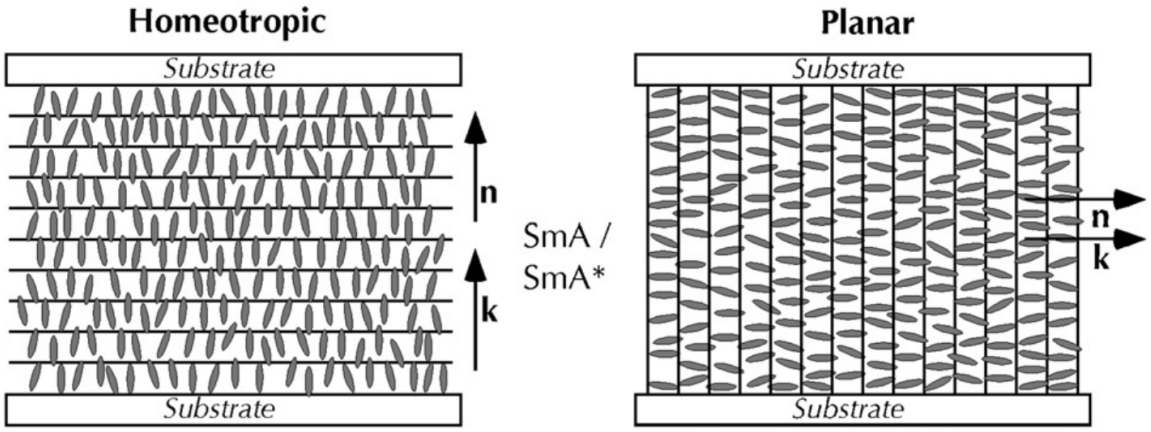

Figure 2.11: Schematic of homeotropic and planar anchoring of calamitic mesogens in the smectic A phase [8], where **n** is the liquid crystal phase director, while **k** is the vector normal to smectic layers. Light would enter perpendicular to one of the substrates. Note that the drawing is not to scale, in reality smectic layers are about 1000 times thinner than the distance between substrates.

each molecule's orientation vector (also a unit vector):

$$S = \langle P_2(cos\theta) \rangle = \left\langle \frac{3}{2} cos^2\theta - \frac{1}{2} \right\rangle \tag{2.1}$$

where the angular brackets represent ensemble averaging.

In order to find the director $\hat{n}$, it is necessary to construct and analyze the second-rank $\mathbf{Q}$ tensor [28]:

$$\mathbf{Q} = \frac{1}{N} \sum_{i=1}^{N} \left(\frac{3}{2} \hat{u}_i \otimes \hat{u}_i - \frac{\mathbf{I}}{2} \right) \tag{2.2}$$

where $\hat{u}_i$ is the orientational unit vector for mesogenic molecule i, N is the total number of mesogens, $\otimes$ is the dyadic product and $\mathbf{I}$ is the second-rank unit tensor.

Once the $\mathbf{Q}$ tensor is calculated, it has to be diagonalized, and the director $\hat{n}$ will be the eigen vector corresponding to the largest eigen value of $\mathbf{Q}$ [11].

2.2 Nanoparticles

Nanoparticles are the aggregates of atoms (e.g. metals) or chemical compounds (e.g. metallic oxides) with at least one of their dimensions being on the nano-scale [29]; they can be covered with various ligands, but are otherwise comprised of familiar materials such as gold, silver [30], CdTe [31] and others. They can be isotropic [32, 33] and anisotropic [29, 34, 35, 36]. Figure 2.12 illustrates the structure of an anisotropic gold nanorod. Nanoparticles are of great research interest because their nano-scale size gives rise to peculiar electronic, chemical and optical properties [37], such as quantized light absorption spectra.

2.3 Simulations of Liquid Crystals

There are several approaches to simulating LC phases, yet all are performed with one objective in mind: to calculate thermodynamic observables [38], such as the elastic constants [39, 40, 3] and other bulk properties, and compare to experimental data. In general, the approaches can be separated into three categories: continuum models, coarse-grained models and atomistic models (schematically depicted in figure 2.13).

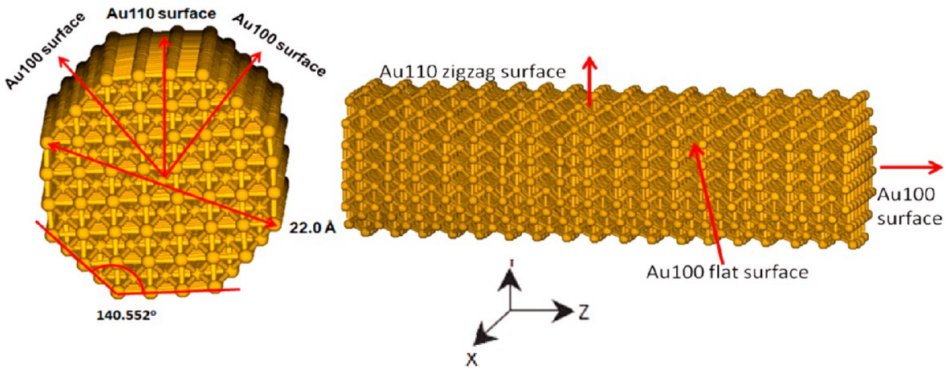

Figure 2.12: Structure and dimensions of an anisotropic gold nanorod [35].

2.3.1 Simulation Scales

Continuum models (e.g. [41]) treat the material as a continuous substance in order to obtain bulk properties, study defects and circumvent the computational limits where a limited number of particles can be simulated within a reasonable amount of time [38]. As per Appendix A, display pixels contain on the order of 10^{14} mesogenic molecules - molecular-scale simulations of such domain sizes remain unfeasible until today; continuum models are still quite valuable for research and industry.

Coarse-grained models discretize the material and consider it at the molecular scale, either treating the molecule as a single entity (for single-site potentials, as in [42, 11, 43] - see also figure 2.14) and keeping track of the molecular centre of mass, or as composed of several rigid units (for multi-site potentials, as in [44] and [45]). This multi-site coarse-grained approach seems to be the most reasonable compromise between computational complexity and realism, since real molecules also have both rigid parts and flexible parts, and rigid parts can rotate about certain axes. Therefore, such models allow researchers to simulate not only the temperature-induced transition between phases, but also the effects of packing efficiency on the density of the material. In contrast, the single-site coarse-grained approach omits these steric degrees of freedom and treats molecules as rigid units with static shapes. This simplifies the model and allows for simulation results to be obtained in a smaller amount of time. Additionally, an argument can be made that though simpler, this modelling technique would be sufficient for cases where molecules are indeed rigid units with shapes defined by their average electron densities.

Finally, atomistic models (of liquid crystals: [3]; and even of water: [46]) keep track of individual atoms in the simulation; interactions between them and the molecules they

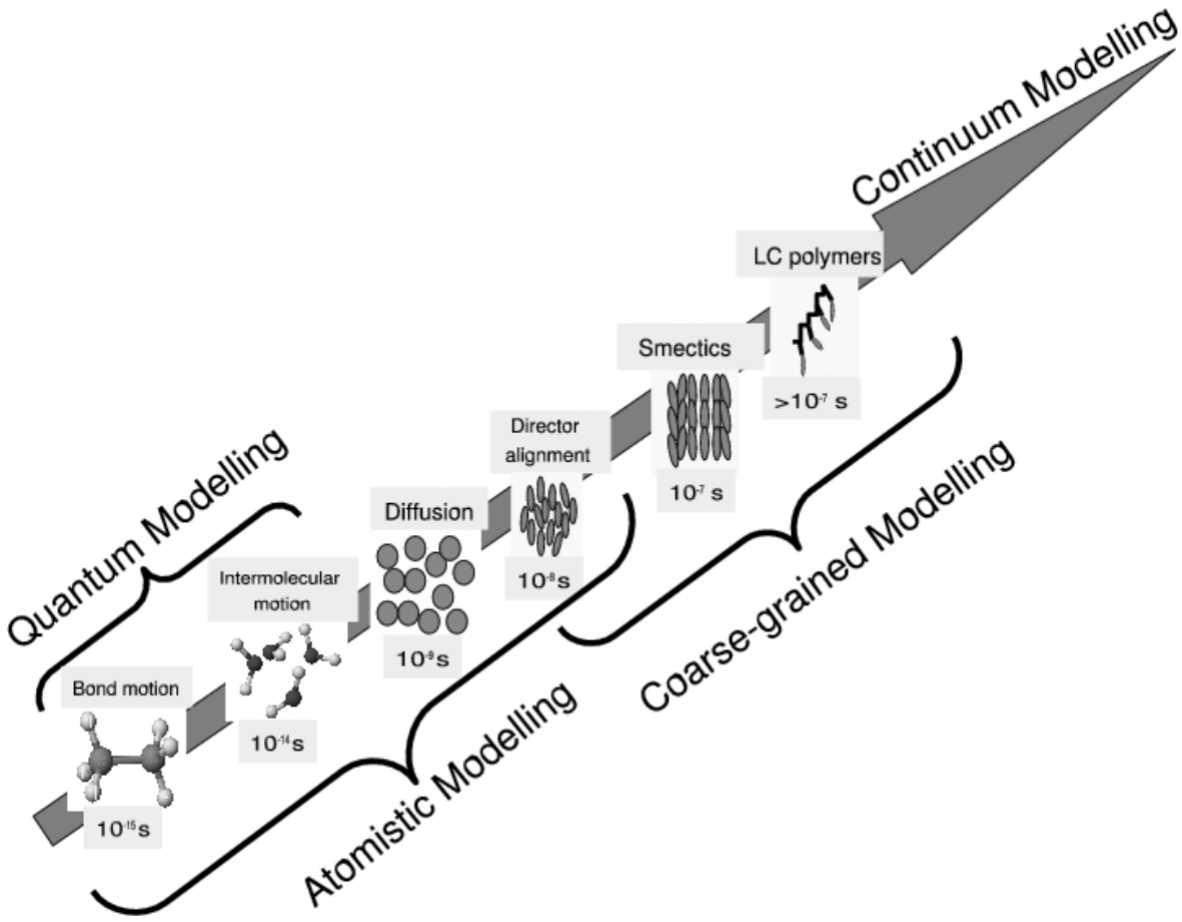

Figure 2.13: Schematic representation of different simulation scales [3].

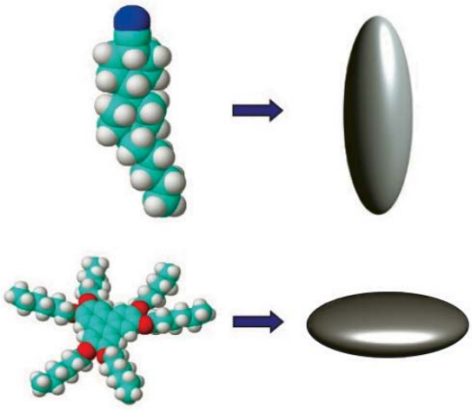

Figure 2.14: Schematic representation of coarse-graining calamitic and discotic mesogens [10] such that the model particles have a centre of mass and a direction vector (which corresponds to the long axis of the prolate ellipsoid (top) and to the short axis of the oblate ellipsoid (bottom)).

comprise are calculated by making use of force fields [3]. Atomistic models tend to rely very heavily on fitting their parameters to data from the density functional theory [47] simulations, also known as "DFT", which take into account actual electron density of molecules in question. Atomistic models undoubtedly retain the greatest amount of degrees of freedom, but the timescales that can be simulated are the shortest and domain sizes are the smallest due to computational complexity of the models. Thus, even though obtained results may be highly accurate, they will likely not be device-relevant, since a pixel of a liquid crystal display contains on the order of 10^{14} molecules or more (calculation provided in Appendix A) while a simulation of this sort will be limited to a number of molecules that is many orders of magnitude smaller, resulting in an unrealistically large surface area to volume ratio and thus unrealistically high boundary effects in the simulation.

2.3.2 "Hard" and "Soft" Particles

Particles in coarse-grained models can be considered either as "hard" [48, 49, 28] or "soft" [42, 50], with the former ones having only repulsive interactions and only when they come in contact [10], while the latter, more realistic case, considers particles to have short-range attractive and repulsive interactions that decay quickly with distance [10, 3, 51]. However, it is worth mentioning that the term "hard" does not necessarily imply that such particles are incompressible. Imposing sufficient pressures on domains with "hard" particles would

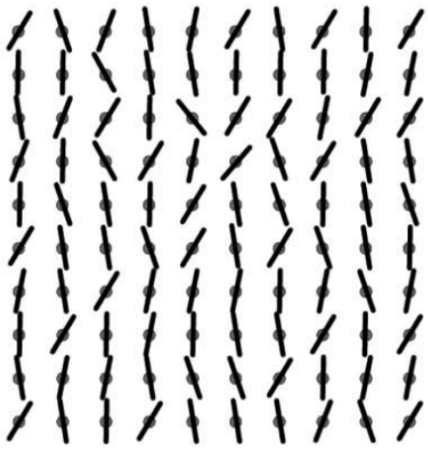

Figure 2.15: A 2D representation of a non polar on-lattice calamitic liquid crystal model [51].

cause them to pack more efficiently, just as in the case of "soft" particles. Depending on the implementation of repulsive forces between "hard" particles, they may be compressible.

2.3.3 "On-Lattice" and "Off-Lattice" Schemes

Finally, simulations can be conducted according to on-lattice [52, 53, 29] or off-lattice [42] schemes. In the former, the molecules are assumed to occupy specific sites within a lattice, which simplifies calculation of neighbors for every particle (since location of sites is fixed and known). However, this is also highly unrealistic for liquid crystals, since they possess liquid-like flow and the positional order of different phases varies (but is always less than in a solid); as a result, off-lattice schemes are used now that computational resources for finding nearest neighbors of a molecule are no longer an issue (which they were some 40 years ago). Figure 2.15 gives a 2D representation of a non polar on-lattice calamitic liquid crystal model. Off-lattice representations can be observed in figures 2.9 and 2.19.

2.4 Pairwise Intermolecular Potentials

If, in some cataclysm, all of scientific knowledge were to be destroyed, and only one sentence passed on to the next generations of creatures, what state-

> ment would contain the most information in the fewest words? I believe it is the atomic hypothesis (or the atomic fact, or whatever you wish to call it) that all things are made of atoms - little particles that move around in perpetual motion, *attracting each other when they are a little distance apart*, but *repelling upon being squeezed into one another*. In that one sentence, you will see, there is an enormous amount of information about the world, if just a little imagination and thinking are applied... (Richard Feynman, *Six Easy Pieces*, p.4; *emphasis added*)

In coarse-grained simulations, particles are treated as single units with centres of mass and orientation vectors [11], or as being comprised of several large units with each having its own centre of mass and orientation vector [54]. In either case, pairwise potentials are commonly employed to calculate the energy of interaction (the Hamiltonian) between the units. Intermolecular energy is directly related to force, where the latter is the spatial derivative of the former. By convention, negative value of the intermolecular force indicates attraction and positive value of the force represents repulsion between particles. At short intermolecular distances repulsive forces dominate the attractive forces to reflect the fact that matter cannot occupy the same space, and that positively charged nuclei and negatively charged electron clouds repel the nuclei and electron clouds of other molecules. However, at longer centre-to-centre distances attractive forces dominate to reflect the fact that positive nuclei of one molecule would attract negatively charged electron clouds of the other molecule, and vice versa. Both attractive and repulsive forces decay quite quickly with increasing separation distances.

2.4.1 Isotropic Potential - Lennard-Jones

Among the pairwise potentials currently used for simulating LC phases at the molecular resolution, it can be said that the vast majority of them has been influenced by the famous Lennard-Jones potential [55, 56, 57] developed in the 1920's:

$$U(r) = 4\epsilon \left[\left(\frac{\sigma}{r} \right)^{12} - \left(\frac{\sigma}{r} \right)^{6} \right] \tag{2.3}$$

in which ϵ is the strength parameter and reflects the strength of bonding, and σ is the range parameter that reflects the sum of the radii of two interacting spherical particles. Originally this potential was developed to describe the interactions of noble gas atoms, but its general form has proved to be quite useful in pairwise systems made up of molecules,

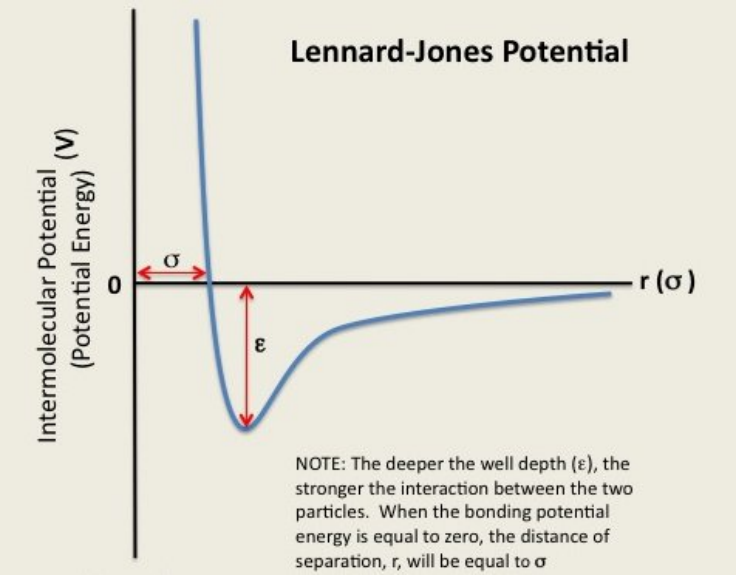

Figure 2.16: A typical plot of a Lennard-Jones interaction taken from [58].

not just atoms. The potential has repulsive and attractive components: the component raised to the power of 12 represents repulsive forces (that dominate at short distances and make the potential energy positive as the centre-to-centre distance decreases), while the component raised to the power of 6 indicates the attractive forces (that dominate the repulsive forces at longer distances and make the energy negative). The Lennard-Jones potential is symmetric (interacting particles have to be of the same type) and isotropic (particles have to be spherical, though they can be of different radii). A typical graph of a Lennard-Jones interaction can be seen in figure 2.16.

Thus, the only variable in the equation is the separation distance r between two molecular centres of mass. Constants σ and ϵ, which are the range and the strength parameters, are determined by the types of interacting particles. The strength parameter reflects the strength of the bond between the two particles, minimum value of potential energy is $-\epsilon$. The larger the value of ϵ, the stronger and more thermodynamically stable is the bond between the two particles. In practice, values for ϵ come from experiments or tables of measured values. This equilibrium bond length can be obtained by differentiating equation 2.3 with respect to r and setting the result to zero, upon which it becomes apparent that the equilibrium bond length (with energy equal to $-\epsilon$) is $\sqrt[6]{2}\sigma$.

The range parameter, σ, is the sum of the radii of the two interacting spherical particles. When the centre-to-centre distance is equal to σ, the potential energy is zero. It is also

worth mentioning that σ, being the sum of the radii of spherical particles, reflects the excluded volume between the two particles' centres of mass because of the centre-to-centre nature of its derivation (the potential is pairwise, hence σ is not based on one particle, but on two of them in the pair). If one particle is fixed in space and the other one is rotated around it by 2π radians in all possible planes, the shape of the excluded volume between the two particles will be spherical. This excluded volume has a radius equal to σ (the sum of the particles' radii) and thus contains the volume of the "stationary" particle as its "core" and the radius of the "moving" particle as the "shell" surrounding the "core"; the shape of the "stationary" particle can be obtained by subtracting the second particle's radius from all locations in the excluded volume (effectively "peeling off" the "shell").

2.4.2 Anisotropic Potential - Gay-Berne

Since the majority of interacting molecules have anisotropic shapes, it became necessary to develop potentials that would capture those interactions.

Developing on the ideas of the isotropic Lennard-Jones potential, an anisotropic potential would have to exhibit an anisotropic excluded volume, and the location and even the magnitude of the minimum potential energy would have to also depend on the relative orientation of the particles.

A step forward in the development of anisotropic potential was the derivation and tabulation of second virial coefficients for nine approximately cylindrical gases as early as 1948 [59]. However, it was still necessary to incorporate orientation dependence between two anisotropic particles. Several attempts have been made, but the most successful and widely used to date was by Gay and Berne [60]:

$$U(\hat{u}_i, \hat{u}_j, \underline{r}_{ij}) = \epsilon(\hat{u}_i, \hat{u}_j, \hat{r}_{ij}) \left[\left(\frac{\sigma_0}{r - \sigma\left(\hat{u}_i, \hat{u}_j, \hat{r}_{ij}\right) + \sigma_0} \right)^{12} - \left(\frac{\sigma_0}{r - \sigma\left(\hat{u}_i, \hat{u}_j, \hat{r}_{ij}\right) + \sigma_0} \right)^{6} \right] \tag{2.4}$$

The Gay-Berne potential is still in the Lennard-Jones form (equation 2.3) in that it has components raised to powers of 12 and 6, but now its range ($\sigma\left(\hat{u}_i, \hat{u}_j, \hat{r}_{ij}\right)$) and strength ($\epsilon\left(\hat{u}_i, \hat{u}_j, \hat{r}_{ij}\right)$) parameters depend on unit vectors of molecular orientations ($\hat{u}_i$,$\hat{u}_j$) and the unit vector $\hat{r}_{ij}$ which is pointing from the centre of molecule i to the centre of molecule j. Since the potential itself also depends on the separation distance r between molecular centres of mass, the intermolecular vector $\underline{r}_{ij}$ appears in $U(\hat{u}_i, \hat{u}_j, \underline{r}_{ij})$. The length scaling unit in this pairwise potential is defined as σ_0. Typical potential energy curves for the Gay-Berne potential can be seen in figure 2.17.

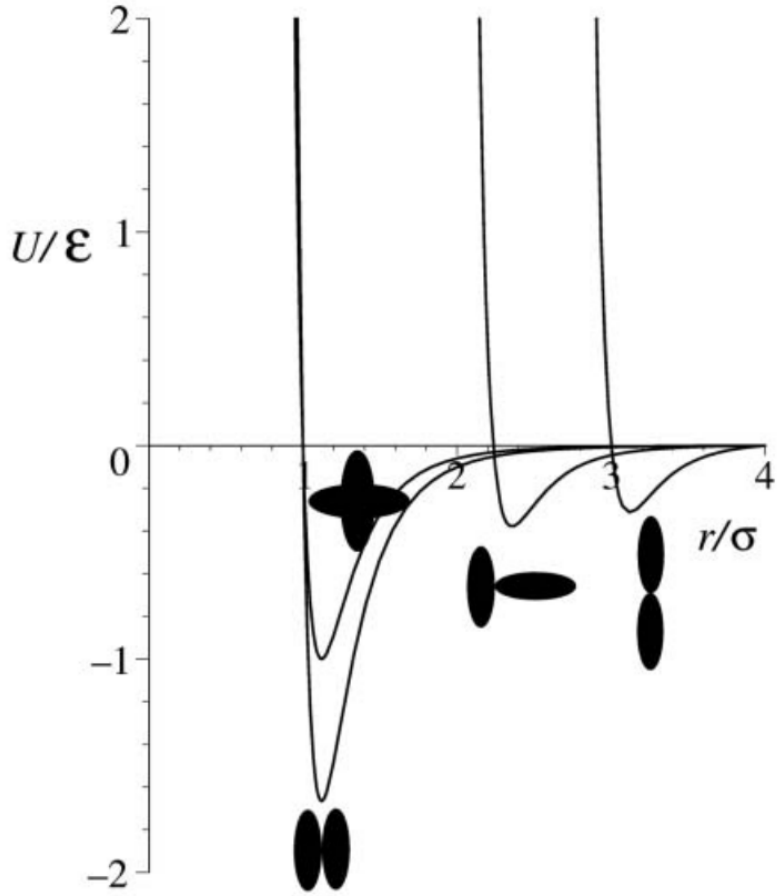

Figure 2.17: Typical potential curves of a Gay-Berne interaction [51]. Pairwise potential energy U and centre-to-centre separation distance r have been divided by the energy and length scaling units, respectively, to obtain dimensionless quantities. Relative orientations of mesogens are depicted by black solid ellipses. The configurations are commonly called, from left to right, "side-by-side" (this is also the most stable configuration with the lowest potential energy), "cross", "T" and "head-to-tail".

The range and strength parameters were given by a rather complicated set of expressions [60]. The strength parameter is a product of two components and uses parametrization constants ν and μ as powers of the components:

$$\epsilon(\hat{u}_i, \hat{u}_j, \hat{r}_{ij}) = \epsilon^{\nu}(\hat{u}_i, \hat{u}_j)\epsilon^{'\mu}(\hat{u}_i, \hat{u}_j, \hat{r}_{ij}) \tag{2.5}$$

The two components are:

$$\epsilon(\hat{u}_i, \hat{u}_j) = \epsilon_0 \left(1 - \chi^2(\hat{u}_i \cdot \hat{u}_j)^2\right)^{-1/2} \tag{2.6}$$

$$\epsilon^{'}(\hat{u}_i, \hat{u}_j, \hat{r}_{ij}) = 1 - \frac{\chi^{'}}{2}\left[\frac{(\hat{r}_{ij} \cdot \hat{u}_i + \hat{r}_{ij} \cdot \hat{u}_j)^2}{1 + \chi^{'}(\hat{u}_i \cdot \hat{u}_j)} + \frac{(\hat{r}_{ij} \cdot \hat{u}_i - \hat{r}_{ij} \cdot \hat{u}_j)^2}{1 - \chi^{'}(\hat{u}_i \cdot \hat{u}_j)}\right] \tag{2.7}$$

with ϵ_0 being the energy scaling unit.

The range parameter, which is the centre-to-centre distance at which the pair potential energy equals to zero, is given as:

$$\sigma(\hat{u}_i, \hat{u}_j, \hat{r}_{ij}) = \sigma_0 \left(1 - \frac{1}{2}\chi\left(\frac{(\hat{r}_{ij} \cdot \hat{u}_i + \hat{r}_{ij} \cdot \hat{u}_j)^2}{1 + \chi(\hat{u}_i \cdot \hat{u}_j)} + \frac{(\hat{r}_{ij} \cdot \hat{u}_i - \hat{r}_{ij} \cdot \hat{u}_j)^2}{1 - \chi(\hat{u}_i \cdot \hat{u}_j)}\right)\right)^{-1/2} \tag{2.8}$$

with σ_0 being the length scaling unit.

The two anisotropy parameters (χ,$\chi^{'}$) that appear in equations 2.6, 2.7 and 2.8 are defined as:

$$\chi = \frac{\sigma_{\parallel}^2 - \sigma_{\perp}^2}{\sigma_{\parallel}^2 + \sigma_{\perp}^2} \tag{2.9}$$

$$\chi^{'} = \frac{\epsilon_s^{1/\mu} - \epsilon_e^{1/\mu}}{\epsilon_s^{1/\mu} + \epsilon_e^{1/\mu}} \tag{2.10}$$

where $\sigma_{\parallel}$ is the length of the major axis of the ellipsoidal mesogen, $\sigma_{\perp}$ is the length of the minor axis of the ellipsoid, ϵ_s is the strength parameter value for the side-by-side configuration, ϵ_e is the value for the end-to-end configuration and μ is the parametrization constant used in equation 2.5. Figure 2.18 contains a schematic representation of the origin of the Gay-Berne mesogen - the ellipsoid was obtained from an integration over four joined Lennard-Jones spheres. Figure 2.19 depicts some thermotropic phases formed by simulations with the Gay-Berne mesogen.

Similar to the Lennard-Jones case, with Gay-Berne the potential energy is zero when $r = \sigma$. Note that the denominators in equation 2.4 are "shifted" - they are constructed in such a way that when $r = \sigma$ the denominator itself is not zero to preserve mathematical

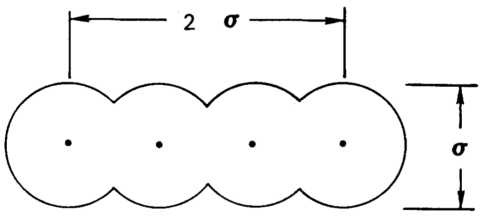

Figure 2.18: Schematic representation of the origin of the ellipsoidal Gay-Berne mesogen [60].

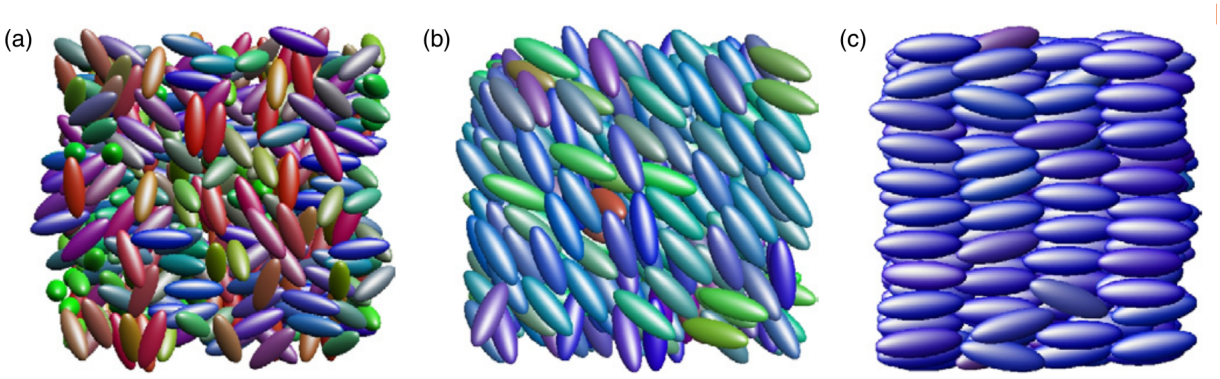

Figure 2.19: Snapshots of some thermotropic phases obtained with the Gay-Berne mesogen [15]. Isotropic (liquid) phase is shown in *(a)*, nematic liquid crystal phase in *(b)* and smectic liquid crystal phase in *(c)*. The colour of mesogens indicates the degree of alignment with the director.

sense. When implementing the potential in computer code, it is necessary to account for situations when $r - \sigma + \sigma_0 < 0$ with an "if" condition - this situation is not physically possible even though it is allowed by mathematics, therefore we must enforce a high positive potential energy when $r - \sigma + \sigma_0 < 0$ occurs. If this is not done, it may be possible for two particles to occupy the same space with a low potential energy value, thus violating the fact that matter cannot occupy the same space.

It is now important to note that the shape of the excluded volume can be obtained from plotting the range function as length from the origin of a coordinate system centred about one molecule as the other is rotated about it and the range function is recalculated at every molecular configuration [49]. In the case of Gay-Berne potential, the molecular shape that is obtained is an ellipsoid. The shape of a single particle can be obtained by "shrinking" the shape of the excluded volume to the dimensions set for the ellipsoid. An extensive study was conducted [61] for the purpose of finding out the closest possible distance of approach between ellipsoids that may not be identical to each other and as a result a new pair potential was written and compared to Gay-Berne, but clear advantages do not seem to have been gained. An efficient but non-trivial algorithm for calculating the possible contact distance has also been proposed in [62].

2.5 Metropolis Monte Carlo

A fairly comprehensive overview of different simulation methods can be found in [38] and [10]. However, two of the major simulation schemes used in computer experiments involving liquid crystals are Monte Carlo and Molecular Dynamics. There are vast differences between the two, most notable ones being that in Monte Carlo the equilibrium behaviour of the material is simulated, while in Molecular Dynamics, as the name implies, the dynamics of the system are the point of interest.

The Monte Carlo scheme (published in 1953 by Metropolis and coworkers [63]), relies on the thermodynamic principle that the system of interest will be found in a state that has the greatest multiplicity [64]. The scheme has been used in various scenarios since then (to point out a few: [52, 53, 48, 11, 65, 66]). Despite the fact that applications are and have been so numerous, the underlying principle has always remained the same: equilibrium behaviour is found through ensemble average. A system is set up with certain initial conditions, and it is then perturbed by random displacements of particles by a certain specified distance (which may be made to vary throughout the simulation if necessary), the Hamiltonian of the system is computed (using a pairwise potential from section 2.4, for example) and compared to the Hamiltonian before the perturbation. The probability

of accepting the new ensemble is dependent upon the ratio of multiplicities between the old and new states - if the new state is less likely to occur, it is less likely to be accepted during the simulation. However, it is not impossible for the less likely state to be accepted, which allows Monte Carlo schemes to overcome local minima of the Hamiltonian in the phase space and indeed converge to the global minimum given enough time [67]. The great advantage of the Monte Carlo scheme is the computational simplicity and the ability to obtain equilibrium behaviour of the system. However, the dynamics are completely ignored.

In contrast, the Molecular Dynamics scheme [67] (used in [39, 45, 24]) essentially simulates random Brownian motion of particles within the system during the simulation. This approach relies on calculating forces and torques [51] experienced by each molecule due to interactions with its neighbors and then using that information to displace particles according to Newtonian laws of motion. The Hamiltonian is then computed (using, for example, a pairwise potential, as described in an earlier section), and the process is repeated until the simulation converges. As a result of taking dynamics of the system into account, data about the response of material to an external perturbation can be obtained [24]. However, computational complexity of the system and the great number of degrees of freedom that have to be accounted for prevents us from accessing macroscopic time and length scales during simulations. Consequently, both Molecular Dynamics and Monte Carlo schemes are used - rather than compete, they complement each other.

As already described, Metropolis Monte Carlo samples the possible domain configurations while entirely ignoring the dynamics of their formation, and includes the more probable configurations in the calculation of thermodynamic observables based on a statistical criterion called the Boltzmann factor. In order to understand the rationale behind the seemingly simple Metropolis Monte Carlo simulation technique, it is necessary to examine a few concepts from statistical mechanics and thermal physics, such as microstates, macrostates and the multiplicity of a macrostate. In addition, it is necessary to dwell upon the concept of the constant-NPT ("isobaric-isothermal" [68, 69, 70, 67]) simulation ensemble, where the number of particles (N), pressure (P) and temperature (T) are held constant and the system's potential energy is allowed to vary.

A microstate of a thermodynamic system is a specific configuration of the system where the state of every particle (e.g. position and orientation) is known. While microstates are unique, they can correspond to the same macrostate (potential energy) of the system. The fundamental assumption of statistical thermodynamics postulates that for an isolated system, all accessible microstates are equally likely [64]. While the constant-NPT ensemble system is closed (number of particles is not exchanged with the surroundings), it is not isolated (the potential energy is not conserved - it is instead exchanged with the surround-

ings). However, the NPT system and its surroundings do form an isolated system, hence the fundamental assumption is still applicable. Even though all microstates are equally likely, all macrostates are not equally likely because multiple microstates can correspond to the same macrostate. In fact, one macrostate at a certain temperature tends to be far more likely than any others because it has the greatest multiplicity of states (i.e. the number of microstates that correspond to this macrostate is much greater than for any other macrostate).

However, the greatest multiplicity does not necessarily correspond to the lowest possible energy of the system under study. For instance, a perfect crystal lattice will have an enthalpy (assuming simulations in isobaric-isothermal ensemble) value lower than an isotropic liquid phase because when the pairwise potential is used to calculate the domain enthalpy, temperature is not included in the calculation and enthalpy depends solely on particle orientations and separation distances. However, above the melting temperature, it is the isotropic liquid state that will have the higher multiplicity, not the perfect crystal lattice. Thus, if the simulation temperature is set to above the melting point, the Monte Carlo algorithm will find the system state that is most likely to occur at that temperature, though it may not have the lowest enthalpy when compared to other possible states of the system.

The Boltzmann factor of a state s (equation 2.11, taken from [64]) corresponds in magnitude to the multiplicity of a given macrostate. Note that k_B is the Boltzmann constant ($1.3806 \times 10^{-23} \frac{J}{K}$), T is the temperature and E is the energy of state s_i.

$$\text{Boltzmann factor} = \exp(-E(s)/k_B T) \tag{2.11}$$

Defining $(k_B T)^{-1}$ as β, equation 2.11 can be rewritten as:

$$\text{Boltzmann factor} = \exp(-\beta E(s)) \tag{2.12}$$

Using the ratio of Boltzmann factors corresponding to the old and new states as the Metropolis Monte Carlo acceptance criterion essentially compares the probabilities of existence of each and shows which of the two is more likely to occur. This is the "importance sampling" of Metropolis Monte Carlo [67] - microstates that are most probable to occur are included when sampling the equilibrium ensemble and used when determining the average macroscopic quantities.

In order to ensure that the Monte Carlo sampling scheme is correct, "detailed balance", a sufficient but not necessary condition, should be satisfied. Since the fundamental

assumption of statistical thermodynamics postulated the equal likelihood of all microstates, it should be possible to return to the original microstate even after a new microstate has been accepted (in other words, it should be possible to undo any move, particle or volume, right after it was successfully accepted). This brings about another important nuance: the maximum values for particle moves and volume changes should be constant numerical values, and not be continuously calculated during the simulation. Otherwise, we may find the maximum allowed moves shrinking or expanding if they are determined based on, say, a percentage of the current volume of the simulation domain. This would prevent the Markov chain from remaining symmetric and Metropolis Monte Carlo results from being valid.

In order to understand the calculation of the probability of acceptance of a new microstate, let us denote the original positions and orientations of N particles in the domain as s^N and let s'^N represent the new positions and orientations after an attempted particle displacement and reorientation (i.e. "a particle move"). If, after an attempted particle move, the calculated domain internal energy $U(s'^N)$ is less than or equal to $U(s^N)$, this indicates that the state s'^N is either more stable or equivalent to state s^N, or in other words, the multiplicity of state s'^N is greater than or equal to that of state s^N, respectively; thus, the new state s'^N is accepted. In other cases, the new configuration s'^N cannot be accepted automatically. Instead, it is accepted with probability:

$$\exp\left\{-\beta\left[U(s'^N) - U(s^N)\right]\right\} \tag{2.13}$$

In the constant-NPT ensemble (isobaric-isothermal ensemble) [68, 69, 70, 67], only volume is allowed to vary to simulate a real experiment performed on a closed system at atmospheric pressure and ambient temperature. Let us denote the original volume by V and the new volume after an attempted perturbation (a "volume move") as V'. Similar to the particle moves, if $U(s^N, V')$ is equal to or less than $U(s^N, V)$, the new state (s^N, V') of the domain is accepted automatically. However, if the new state is less stable than the original state, the perturbation to the original state is accepted with probability:

$$\exp\{-\beta\left[U(s^N, V') - U(s^N, V) + P(V' - V) - N\beta^{-1}\ln(V'/V)\right]\} \tag{2.14}$$

When implementing these acceptance criteria in computer code, the results (i.e. Boltzmann factors) calculated using equations 2.13 and 2.14 are compared to a uniform random number on the interval $[0, 1)$ and new states are accepted if the result is greater than the random number because the probability that the Boltzmann factor is greater than the uniform random number between 0 and 1 is, in fact, equal to the Boltzmann factor.

It is important to note that for a volume move, reevaluation of free energy is simple and recalculating pairwise interactions is not necessary [67], decreasing the computational expense of this perturbation of the simulation domain. Denoting the original linear dimensions of the system by L and the new dimensions (after the attempted volume move) by L', the new free energy value $U(L')$ can be obtained by scaling the repulsive (power of 12) and attractive (power of 6) components of the original free energy as follows:

$$U(L') = \left(\frac{L}{L'}\right)^{12} U_{12}(L) - \left(\frac{L}{L'}\right)^{6} U_{6}(L) \tag{2.15}$$

Equation 2.15 has been employed in the NPT simulations performed in this thesis in order to decrease the computational expense incurred upon perturbing the domain volume.

Chapter 3

Literature Review

In this chapter an overview of relevant scientific literature is conducted. The review begins by discussing existing pairwise anisotropic potentials employed in the simulation of liquid crystal phases in section 3.1. Next, current experimental work on liquid crystal-nanoparticle mixtures is discussed in section 3.2. Finally, current simulation work on liquid crystal-nanoparticle mixtures is summarized in section 3.3.

3.1 Anisotropic Pairwise Potentials

Incorporation of anisotropy into pairwise potentials (attempted, for example, in 1980's [71, 60, 72, 73] and, of course, earlier [74, 75]) and representation of realistic molecular shapes have been areas of ongoing research for the last 60 years.

Capturing all features of a mesogen at the coarse-grained level is a difficult task. For instance, quite notable, and perhaps surprising, is the fact that in a liquid crystal it is not only the phase transition that depends on temperature, but also the shape of mesogens. In his 2007 review, Wilson wrote that in a real liquid crystal, the change in density at phase transition from liquid to liquid crystal is around 1 % whereas simulations using Gay-Berne mesogens exhibit a change of 10 %, which is an unrealistic value [51]. The discrepancy is attributed to the fact that in Gay-Berne simulations the shape of mesogens is independent of the temperature, whereas in a real material the shape changes. Muccioli and Zannoni attempted to account for that in their publication [50], but their work was focused on cylindrically symmetric particles. Nevertheless, they found that nematic-smectic transition temperature is dependent on fluctuations in molecular shape, while nematic-isotropic transition temperature was not sensitive to that.

Other than Gay-Berne, there are several other notable anisotropic pairwise potentials that exhibit liquid crystalline behaviour. Two of them are the Weeks-Chandler-Andersen potential [75] applied in [76, 77] to liquid crystal-nanoparticle mixtures (see section 3.3) and the Kihara potential [74], studied in [78, 79] (among other works) and applied to binary mixtures in [80] (see section 3.3).

The Weeks-Chandler-Andersen potential between a pair of particles with indeces i and j, in its purely repulsive form, was given in [76, 77] as:

$$U_{ij} = 4\epsilon_0 \left[\left(\frac{\sigma_0}{r'_{ij} - R_{ij}} \right)^{12} - \left(\frac{\sigma_0}{r'_{ij} - R_{ij}} \right)^{6} + \frac{1}{4} \right] \tag{3.1}$$

if $(r'_{ij} - R_{ij}) \leqslant \sqrt[6]{2}\sigma_0$ and $U_{ij} = 0$ otherwise. In the formulation, σ_0 and ϵ_0 were the length and energy scales, respectively. The distance between particles was r'_{ij}, but the definition varied based on particle pair: for two spherical particles, r'_{ij} was between the centres of mass; for the rod-sphere pair, r'_{ij} was the shortest distance between the sphere's centre of mass and the axis of the rod-like particle; for the rod-rod pair, r'_{ij} was the distance of closest approach between the rod-like particles. The constant R_{ij} depended on the particle pair (e.g. rod-rod, rod-sphere). Orientational dependence of the potential energy was included through r'_{ij}, which changed depending on the relative positions of two interacting particles.

The Kihara potential, also purely repulsive, was given in [80] as:

$$U_{ij} = 4\epsilon_{ij} \left[\left(\frac{\sigma_{ij}}{d_m} \right)^{12} - \left(\frac{\sigma_{ij}}{d_m} \right)^{6} + \frac{1}{4} \right] \tag{3.2}$$

if $d_m \leqslant \sqrt[6]{2}\sigma_{ij}$ and $U_{ij} = 0$ otherwise. Particle indeces are given by i and j, d_m is the minimum distance between particle cores (the axis of the rod-like particle and the centre of mass of the spherical particle), σ_{ij} is the half of the sum of the interacting particles' diameters and ϵ_{ij} is the energy parameter, which may be set to the same constant (ϵ_0) for all particle pairs. The value of d_m for the rod-rod pair had to be computed via a non-trivial algorithm, defined in [62].

In both the Weeks-Chandler-Andersen and the Kihara potentials, which are quite similar, the strength parameters ϵ_0 and ϵ_{ij} are independent of the orientation of the interacting particles. As discussed in section 2.4.2, the Gay-Berne potential accounted for that issue, but not without imperfections, since it is restricted to ellipsoidal mesogens. The realism of the ellipsoidal shape has been questioned [11, 81], since ellipsoids may produce too much interdigitation between the layers of a liquid crystal. The reason why the shape of simulated mesogens is a concern is because liquid crystal phase formation depends on molecular

shape [22] and packing. Thus, relevance of simulation data to experimental results also depends on accurate representation of shape.

Attempts have been made to alter the Gay-Berne potential's range and strength parameters to reflect more realistic shapes in the works of Zewdie [11, 81] and quite a few other researchers have built on Zewdie's approach [82, 10, 49, 83]. In all of those works the potentials remained in the Gay-Berne form, but the shape and interactions of the mesogens have been captured through different range and strength functions, respectively. In Zewdie's work [11, 81], a modified version of the Corner potential [59] was employed:

$$U(\hat{u}_i, \hat{u}_j, \underline{r}_{ij}) = 4\epsilon(\hat{u}_i, \hat{u}_j, \hat{r}_{ij}) \left[\left(\frac{\sigma_0}{r - \sigma\left(\hat{u}_i, \hat{u}_j, \hat{r}_{ij}\right) + \sigma_0} \right)^{12} - \left(\frac{\sigma_0}{r - \sigma\left(\hat{u}_i, \hat{u}_j, \hat{r}_{ij}\right) + \sigma_0} \right)^{6} \right] \tag{3.3}$$

with ϵ being the strength parameter, σ being the range (or "shape") parameter, σ_0 being the contact distance between two rod-like particles in their side-by-side configuration, and r representing the centre-to-centre separation distance (for homogeneous and heterogeneous particle pairs). Molecular orientation unit vectors were $\hat{u}_i$ and $\hat{u}_j$, and the intermolecular vector from particle i to particle j was $\underline{r}_{ij}$ with the corresponding unit vector being $\hat{r}_{ij}$. The range and strength parameters were formulated through expansion in terms of orthogonal basis "S" functions [84] ("rotational invariants", as they are called in [10, 85, 86] and other publications) dependent upon dot products of molecular orientation unit vectors and the intermolecular unit vector $\hat{r}_{ij}$:

$$\sigma(\hat{u}_i, \hat{u}_j, \hat{r}_{ij}) = \sigma_0 \sum_{L_i L_j J} \sigma_{L_i L_j J} S_{L_i L_j J}\left(\hat{u}_i, \hat{u}_j, \hat{r}_{ij}\right) \tag{3.4}$$

$$\epsilon(\hat{u}_i, \hat{u}_j, \hat{r}_{ij}) = \epsilon_0 \sum_{L_i L_j J} \epsilon_{L_i L_j J} S_{L_i L_j J}\left(\hat{u}_i, \hat{u}_j, \hat{r}_{ij}\right) \tag{3.5}$$

where ϵ_0 is the energy scaling unit. The expansion coefficients were found by fitting to the calculated values of σ and ϵ from other potentials. The approach in [11] is able to capture complicated shapes with appropriate expansion coefficients and number of terms in the expansion, but only cylindrically symmetric particles have been demonstrated to date (spherocylindrical shapes in [11], disk-like shapes in [85] and pear-shaped/"tapered" particles in [82, 10, 49, 83]). This illustrates that the representation of biaxial (non cylindrically symmetric) shapes is a rather complicated and challenging task.

The promise behind simulation and development of biaxial liquid crystals lies in predictions that upon the application of external electric field the response from the rotation of the minor axis can be up to an order of magnitude faster than the long axis [24], which

means that displays employing this technology would surpass the image quality of current products. Equipment for computer networks that utilizes liquid crystals would certainly benefit from faster switching times as well.

When it comes to modelling biaxial mesogens, the increase in complexity should not be surprising - just like the simulations of cylindrically symmetric particles are more challenging than simulations of spherically symmetric particles, simulations of biaxial particles are more challenging than of cylindrically symmetric particles. In the former case, anisotropy is added as the complicating factor, while in the latter the dependence of intermolecular interactions on orientation of molecules is even greater than before, since rotating a molecule about its long axis will no longer create equivalent interactions for a biaxial molecule unlike for the case of a cylindrically symmetric molecule.

This added complexity notwithstanding, the popular Gay-Berne potential has been adapted and used for simulations of biaxial molecules. One approach was through joining two [87] or three [54] ellipsoidal Gay-Berne mesogens together to resemble a bent-core shape and then simulating the equilibrium behaviour of 1000 of these bent-cores using Monte Carlo in the isobaric-isothermal ensemble. Other, more ubiquitous approaches [88, 10, 89, 23, 65, 90, 24, 91], involved altering the ellipsoidal mesogens to remove the cylindrical symmetry from their shapes; a dipole was frequently added in addition to shape modification. One unique paper [20] conducted experimental synthesis and analysis work as well as atomistic simulations of the "twist-bend" nematic bent-core mesogen and found a new nematic liquid crystal equilibrium symmetry to exist, which is a rare and important event in liquid crystal science.

The approach employed in this thesis to simulating rod-rod and rod-sphere interactions can be extended to biaxial shapes by including other terms in the orthogonal expansions of the range and strength parameters and fitting the range parameter to a banana-like shape.

To the extent of the knowledge gained after conducting the literature review, there has been only one published work [85] that used the S function [84] Corner potential [59] (originally proposed by Zewdie [11]) for studying any kind of mixtures. In [85], eight S functions (up to fourth order) were used to describe the shapes of two disk-like particles, one with a protuberance in the centre, another with a depression in the centre. The coefficients for the range parameter expansion in terms of the S functions were obtained by fitting to contact distances calculated for eight configurations of the heterogeneous particle pair and six configurations for the two pairs of identical particles. The coefficients were the solutions to linear systems built for each particle pair. The strength function was the same for both disks, but their shapes were different; hence, this study elucidated the effects of molecular shape on the phases that could be formed by the materials. Four sets

of simulations, two with pure substances and two with 2:1 mixtures of the two disk-like particles, were performed using Monte Carlo in the isobaric-isothermal ensemble, with a total of 648 and 5184 (8×648) particles in the domain. Variations of temperature by 0.1 (in reduced units) from 2.0 to 3.5 revealed that of the four systems of interest, only one domain exhibited a discotic nematic liquid crystal phase - it was composed entirely of disks with protuberance at the centre.

3.2 LC-NP Mixtures Experimental Work

Recently, with the growth of the field of nanotechnology there has been an increasing amount of interest in adding nanoparticles to liquid crystals in order to improve the existing or obtain new properties of liquid crystals and enable new technological applications [8].

In their excellent review paper, Lagerwall and Scalia [8] go over a large number of applications of liquid crystals. According to Lagerwall and Scalia, a possible application of liquid crystals is to position spherical nanoparticles (inorganic metal particles, for instance) and order anisotropic nanoparticles, such as carbon nanotubes. Currently, the progress in controlling the position of nanoparticles using liquid crystals has been slow and these systems need to be understood in more depth to achieve this goal. Significantly more success has been achieved in positioning micro-scale particles. When it comes to dispersions of inorganic nanoparticles in liquid crystals, according to the reviewers, these efforts are aimed at modifying the properties relevant to the display application of LCs, namely speeding up the switching time between the "on" and "off" states ("light allowed through" and "light blocked", respectively) or changing the type of alignment of the liquid crystal within a pixel. Dopant nanoparticles have also been used for improving electrooptical, dielectric and optical properties of the liquid crystal host [26, 92] and even for aligning the mesogenic molecules with respect to the liquid crystal cell substrate [93].

The inorganic nanoparticles added to liquid crystal hosts are usually metallic or metal oxides, e.g. Au, Ag, Pd, Pt, and ZnO, with diameters of 30 nm or less in most cases [94]. In addition, semiconducting nanoparticles, such as CdSe and CdTe (also called "quantum dots") have been added to liquid crystal hosts [26]. However, experiments utilizing gold nanoparticles are the most ubiquitous in literature [37, 95, 96, 33, 32, 97, 92, 26, 98, 99, 100, 101].

The effect of adding MgO particles (10 nm in size and their concentration being 0.1 $wt\%$) has been reported in [102]. Some of the industrial benefits of adding nanoparticles to liquid crystals were reported to be the reduced operating voltage and shortened response

time of Liquid Crystal Display cells due to the disruption of mesogenic alignment by the nanoparticles [102]. These effects would translate to lower power consumption and less image "ghosting" (appearance of multiple silhouettes of a moving object on the screen), especially at lower temperatures.

Similar improvements due to doping by nanoparticles have been reported for polymer-dispersed liquid crystals (PDLCs) [25]. More specifically, a higher contrast ratio, lower driving voltage and a reduced time response were obtained. In general, the doping concentrations were kept low (under 3 $wt\%$) in order to achieve a more even distribution of nanoparticles by keeping their inter-particle interaction forces low. Interestingly, in PDLCs it's the polymer matrix that is doped with nanoparticles rather than the liquid crystal droplets dispersed in the polymer, yet the improvements are similar to the direct doping of liquid crystal domains.

A study by Donnio and coworkers [32] reported on self-organization of ferromagnetic gold nanoparticles in a thermotropic cubic phase. The nanoparticles had an average diameter of 2.1 nm with a standard deviation of 0.5 nm and were spherical to a first approximation (actual shape was a polyhedron). Dendritic structures were grafted onto the Au nanoparticles and an interesting phase diagram was observed. It is important to point out that in this case a liquid crystal host was not necessary - combination of nanoparticles with the dendritic structures, which are not mesogenic by nature, caused a mesophase to assemble. The melting point was reported to be below 0 $^{\circ}C$, but an ordered cubic phase emerged again from isotropic phase at 75 ± 5 $^{\circ}C$.

Holt and coworkers [33] doped a discotic liquid crystal with 1 $wt\%$ of methylbenzene thiol coated gold nanoparticles. The nanoparticles had a mean diameter of 2.7 nm with a standard deviation of 0.5 nm. The authors reported an increase in the conductivity of the liquid crystal material by at least two orders of magnitude from the typical value on the order of 10^{-3} $cm^2V^{-1}s^{-1}$, and an even greater increase when an external electric field was applied, regardless of the phase of the thermotropic liquid crystal (the material was studied in its crystal, columnar and isotropic phases). Since the dopant concentration was low but the conductivity improvement was dramatic, it was postulated that the increase in conductivity was due to nanoparticles being organized into chains by the external field. The authors observed a similar effect when the nanoparticles were dispersed in hexadecane (which is not a mesogenic material), but only the LC-NP mixture preserved the improvement in conductivity upon cooling in the presence of the external field, whereas hexadecane-NP mixture did not.

Pratibha and coworkers [96] reported stable dispersions of colloidal gold nanoparticles (with 14 nm diameter) in smectic A phase of the 8CB liquid crystal, more stable in fact than

in the nematic phase of 8CB due to the layers present in the smectic phase and separation of nanoparticles from each other by these layers. Agglomeration was not observed in the study; separations between the nanoparticles remained larger than several nanoparticle diameters even for high concentrations of dopant in the dispersing medium.

Interesting results have been achieved by Oswald and coworkers [95] in using small concentrations (0.1 $wt\%$, 0.225 $wt\%$ and 0.65 $wt\%$) of gold nanoparticles (4.7 nm average diameter) to decrease the mobility of edge dislocations that exist between the layers of smectic A phase of 8CB liquid crystal. The composite material has been hardened in response to compressions perpendicular to the layers. Decreasing the mobility of these edge dislocations by using the nanoparticles as a dopant essentially mimicked the conventional alloy hardening widely used in the field of metallurgy. Oswald and coworkers suggested the study of aggregate formation and their effect on edge dislocation mobility is a possible direction for future work on their project.

Milette and various coworkers have reported on a number of experiments involving gold nanoparticle dispersions in liquid crystals. In [98], the methods and results of tuning miscibility of gold nanoparticles in a liquid crystal host were published. Using 4-5 nm diameter gold nanoparticles and various capping ligands, the researchers were able to achieve complete miscibility in the isotropic phase of 5CB liquid crystal with concentrations of up to 25 $wt\%$ Au nanoparticles. Miscibility and phase separation of Au NPs were inferred using Polarized Optical Microscopy and UV-Vis spectroscopy with the observation of absorption peak locations in the latter, which occurred due to the surface plasmon resonance phenomenon of gold nanoparticles. If the peaks shifted at different concentrations, it indicated a change in nanoparticle spacing, with "red" shifts being indicative of phase separation. Solubility of the nanoparticles was found to be very sensitive to the length of the ligands used to cover the nanoparticles. In [100], reversible formation of aggregates of gold nanoparticles (4.7 nm diameter, 1.0 $wt\%$ (0.05 % vol)) within a smectic phase of 8CB liquid crystal was observed using Polarized Optical Microscopy. Complete dispersion was observed in the isotropic phase, circular aggregates formed upon cooling to the nematic phase and linear arrays were formed upon a further decrease of temperature to the smectic phase with homeotropic boundary conditions (i.e. the mesogens were oriented perpendicular to the glass substrates confining the liquid crystal). The periodicity of the linear arrays was at the micron-scale. Cell geometry and boundary conditions were found to influence the geometry of the arrays formed by the nanoparticles in the smectic phase.

Formation of reversible long-range gold nanoparticle networks within 5CB and 8CB liquid crystals has been observed by Polarized Optical Microscopy in [99] at nanoparticle concentrations of 1 $wt\%$ and analyzed from a thermodynamic point of view in [101]. The nanoparticle diameters were 4-5 nm, and the networks were found to be stable in the ne-

matic phase of the liquid crystal host in excess of several weeks. The network features spanned hundreds of microns and the network topology was preserved upon cooling down to the crystalline state and heating back up to the nematic phase. When the samples were heated to isotropic state, the nanoparticles completely dispersed. Upon cooling, networks of gold nanoparticles formed once more. Theoretical analysis in [101] concluded that the balance of entropic forces and excluded volume effects, in addition to interactions between nanoparticles, capping ligands and host mesogens, was responsible for the formation of networks. In addition, it was postulated that the nematic-to-isotropic transition temperature decreases with greater concentration of gold nanoparticles in the host.

Based on the conducted literature review of the experimental work, it can be concluded that gold nanoparticles with diameters under 5 nm (which is comparable to mesogenic molecules' dimensions) dispersed at concentrations of up to 25 $wt\%$ in 5CB and 8CB hosts are the most popular and well-studied systems to date. Since experimental work has shown good dispersion of nanoparticles in nematic and even smectic phases (with some aggregate formation in the latter) with a proper choice of capping ligands and "survival" of those phases even at high concentrations of nanoparticles [94], it can be postulated that simulations of LC-NP mixtures may also show good dispersion for at least a few concentrations of nanoparticles in the LC domain with appropriate settings for LC-NP mixing rules. It can also be expected that the liquid crystal to isotropic transition temperatures will decrease as the dopant concentration increases [101]. However, since the simulations in this thesis were conducted at molecular ("nano") scales, it is unlikely that nanoparticle network formation can be captured accurately, since in real samples the networks extended over hundreds of microns.

3.3 LC-NP Mixtures Simulation Work

The literature review summarized in this section was conducted in order to gain a better understanding of what simulations have been done in the past with liquid crystal-nanoparticle mixtures at the molecular scale.

Soulé, Reven and Rey [103] used a mean-field continuum thermodynamic model to study phase behaviour of thermotropic nematic liquid crystal-nanoparticle mixtures with varying temperatures and nanoparticle radii. It was found that small nanoparticles (with diameters on the same order of magnitude as the length of calamitic mesogens) affected the nematic-isotropic transition temperature significantly by lowering it with increasing nanoparticle volume fractions. However, systems with large nanoparticles mixed in the liquid crystal host exhibited phase behaviour very similar to that of the pure liquid crystal. Moreover,

both small and large nanoparticles were found to be more miscible with the liquid crystal than those with intermediate sizes due to the balance of entropic and enthalpic effects on miscibility. However, the existence of homogeneous nematic, isotropic and crystalline states (and coexistence of any two of the former) was not a simple function of nanoparticle radius, but a delicate balance of temperature, nanoparticle volume fraction and nanoparticle-liquid crystal interactions. Soulé, Milette, Reven and Rey [104] have successfully used the published model [103] to analyze experimental results of dispersing gold nanoparticles in the 5CB nematic liquid crystal and the phase equilibrium behaviour of the mixtures.

Continuum theories have long been used for understanding LC phases and designing devices that benefit from the unique properties of LCs. Some have been quite successful even in predicting the properties of liquid crystal cells doped with nanoparticles [27]. However, continuum theories may ignore the effects and phenomena present at molecular resolution. These molecular scale properties may no longer be negligible when nanoparticles (NPs) are added to LC phases. The growing development of devices that utilize nanotechnology in general and NPs in particular requires a better understanding of the structure of both pure LC phases and LC-nanoparticle mixtures at the molecular resolution. [8] To this end, models that provide molecular resolution of liquid crystal-nanoparticle mixtures can be quite beneficial, despite the fact that they can capture domains containing significantly less molecules than would be in a continuum model.

Krasna, Cvetko and Ambrozic [29] used an on-lattice model [52] to study mixtures of nematic liquid crystals and anisotropic magnetic nanoparticles. Homeotropic anchoring of liquid crystal molecules towards the nanoparticles was assumed. A domain of $80 \times 80 \times 80$ sites was quenched from an isotropic state with all particles having random directions. Upon cooling, nematic domains emerged and nanoparticles acted as stabilizers for the domain orientation patterns. The nanoparticles were also found to cause biaxiality in the domain orientation.

Tian, Smith and Glaser performed molecular dynamics simulations of nanoparticles in a nematic liquid crystal host [76]. The simulations were conducted in a cubic simulation box with periodic boundary conditions using a purely repulsive pairwise Weeks-Chandler-Andersen potential [75]. The domains consisted of 40000 and for some simulations 120000 soft spherocylinders, with nanoparticle volume fractions below 0.2 % for all but one case with larger diameter particles in the domain. The authors reported that their nematogens exhibited a tendency for planar anchoring towards the nanoparticles, while other studies (which used variations of the Gay-Berne [60] potential) showed a tendency for homeotropic anchoring [105, 106]). The researchers also found that the size of nanoparticles strongly affected the phases that could be formed by the originally nematogenic domain; moreover, mesogens exhibited a preference for planar anchoring towards larger nanoparticles. Thus,

the presence of smaller nanoparticles caused a greater disruption of local orientational order than large nanoparticles since the anchoring preference for smaller nanoparticles tended to homeotropic rather than planar. Finally, it was reported that the liquid crystal matrix induced long-range repulsion between the nanoparticles when the diameter of the nanoparticle was comparable to the length of mesogenic molecules.

Tian and Smith conducted further investigations [77] for the case when nematogen length was similar to nanoparticle diameter in order to see how the liquid-crystal-matrix-induced long-range repulsive forces between nanoparticles affected the dispersion of the dopant in the dense nematic host. The molecular dynamics simulations were conducted in the NPT ensemble with domains consisting of 10000 soft spherocylinders for investigating the phase diagram of pure liquid crystal and 120000 soft spherocylinders and 10 to 6000 nanoparticles (nanoparticle volume fractions ranged from 0.0009 to 0.1620) for observing the effect of dopants on the phase transitions in the composite material. The simulations revealed that higher pressures resulted in greater domain order, i.e. increasing the pressure would cause the system to transition from an isotropic phase to the nematic phase. It was found that dispersion of the nanoparticles was maintained even at high dopant concentrations and phase separation did not occur. This finding was contrary to the expectations that may have been formed based on observed behaviour for binary mixtures of spherical particles in nematic hosts with large differences in the sizes of dopants and mesogens. Moreover, it was found that the addition of nanoparticles to the LC domain required higher pressures to be imposed on the simulation domain in order to maintain the same value of the nematic-isotropic transition temperature.

Note that for the above two publications [76, 77] errata have been also been published [107]. Based on the discovered and corrected errors, it was concluded that the dispersion of nanoparticles in the isotropic liquid crystal matrix was solely due to short range interactions [108].

Building upon [76, 77, 107], Xu, Bedrov, Smith and Glaser [108] conducted molecular dynamics simulations in the isobaric-isothermal (NPT) ensemble with 10000 soft spherocylinders (SSCs) and hard spherical nanoparticles (NPs) where SSC length was equal to NP diameter. The purpose of the study was to investigate the phase behaviour of the mixture at varying NP concentrations (from 0 to 500 NPs) with planar or homeotropic LC anchoring towards the NPs. Pressure was used as the driving force of phase transitions for a given NP concentration. Low concentrations of NPs did not disturb the nematic phase and NPs did not aggregate; high concentrations of NPs prevented the formation of a nematic phase. Some aggregation was observed even with 10 NPs in 10000 SSCs, and significant aggregation was reported at concentrations with more than 100 NPs in 10000 SSCs. With increasing NP concentrations, the isotropic-nematic transition pressure also

increased. It was found that with planar LC-NP anchoring (which was naturally preferred by the model potential due to entropic effects), the nanoparticles were dispersed in the isotropic SSC matrix, while at higher pressures phase separation into NP-poor nematic and NP-rich isotropic phases occurred. With homeotropic LC-NP anchoring, aggregation of NPs was observed even at the lowest concentrations. This was contrary to the expectation that the strong mid-range LC matrix-induced repulsion between NPs would maintain the nanoparticles in their dispersed state.

Cuetos and coworkers [109] have extended the Onsager and Parsons-Lee theories in order to study binary mixtures of hard spheres (used to model nanoparticles) and hard spherocylinders (used to represent mesogens). Both theories originally postulated that the free energy of the system composed of anisotropic spherocylinders depends on the relative orientation of the spherocylinders to the nematic director. The authors incorporated the dependence of free energy on the concentration of spherical particles and the excluded volume between nanoparticles and spherocylinders. The expressions employed in modelling the system using the Monte Carlo technique were rather complex. The study showed some differences between the two extended theories, especially the fact that the Onsager theory was accurate for mesogenic molecules with aspect ratios of 100 or greater while the extended Parsons-Lee theory remained qualitatively correct for rod-like particles with aspect ratios between 5 and 20. Among other conclusions, it was found that the extended theories gave results in harmony, at least qualitatively, with experimental data: introduction of spherical particles into the domain composed of rod-like mesogens disturbed the nematic order, larger volume fractions occupied by spheres resulted in phase separation and relative sizes of rod-like and spherical particles played an important role in uniformity of the mixture.

Peroukidis, Vanakaras and Photinos [110] conducted simulations to study nematic and demixing behaviour in binary mixtures of rods and spheres, plates and spheres, and rods and plates. For the purposes of this literature review, binary mixtures of rods and spheres were the most relevant. Rods were represented as linear strings of cubes, while spheres were represented as $3 \times 3 \times 3$ collection of cubes with the middle cube serving as the centre of the particle and other 26 cubes being the soft shell of the particle. The entire domain was represented as a cubic lattice consisting of such rods and spheres. The free energy of the system was minimized in order to find the phase behaviour as a function of pressure and concentration of spherical particles. It was found that at low pressures the system was isotropic, while at higher pressures nematic and smectic phases were formed. In the smectic phase, the majority of the spheres was found between the smectic layers, resulting in a "lamellar" phase. The spacing between the layers of mesogens decreased with higher pressures and higher concentrations of rod-like particles. Higher anisometry of rod-like particles was found to stabilize the nematic phase. Finally, of the three possible

thermodynamically stable phases, isotropic, nematic and lamellar, coexistence was found for all possible combinations of two out of the three phases. The authors suggested that since the model qualitatively reproduced results from experimental publications despite the very simple shapes employed in representation of particles, phase behaviour may be controlled simply by shape anisometry of mesogens and the relative sizes of mesogens and dopants.

Avendaño and coworkers [111] performed Monte Carlo simulations in the NVT ensemble of binary mixtures of 1020 charged hard spherocylinders and 1020 charged hard spheres. The Wolf procedure was employed in order to account for long-range Coulombic interactions within the simulation domain. The spherocylinders had a length-to-diameter aspect ratio of 5.0, and the diameters of the spheres were two times less than the diameters of the spherocylinders. Two models were considered, with charges of the spherocylinders being located at their ends and at their centres. For both models, temperature variations induced the transition from isotropic to nematic phase. However, for the case where the charges of the spherocylinders were at their ends, a nematic-smectic A phase transition was also observed, while for the second model a columnar phase was found in addition to the nematic phase.

Piedrahita, Cuetos and Martinez-Haya [80] studied the diffusion of spherical particles through smectic layers of rods using a purely repulsive shifted and truncated Kihara potential and a Brownian Dynamics model. In their study, the algorithm for calculation of the closest distance of approach [62] between pairs of particles interacting via the Kihara potential was rather non-trivial for rod-rod and rod-sphere pairs. The diameters of spheres and rods were set to be equal, but in different studies the rods had varying anisotropies - length to diameter ratios were 4, 5 and 7. The Monte Carlo technique was employed in the NPT ensemble to find an equilibrium configuration of the binary mixtures of rods and spheres (at least 2000 particles in total) with molar fractions of spheres being 0.01, 0.1 and 0.5. The equilibrium phases turned out to be lamellar, with alternating layers of rods and spheres (which was similar to the results reported in [90]). After the equilibrium configurations were established, Brownian Dynamics was applied to study diffusion of spherical particles through the material. It was found that the transport of spheres was anisotropic - they accumulated between the smectic layers of rods and diffusion of a sphere within a layer of spheres was much faster than diffusion across (through) the layers of rods. Interestingly, when one sphere would penetrate a rod layer, it effectively opened up a channel and caused collective diffusion of other spheres through the channel. Increasing the packing fraction or the length of rods caused the transport of spheres to become even more directional because the diffusion through the smectic layers was diminished.

In this thesis, work has been done on simulating liquid crystal-nanoparticle mixtures

using the S function [84] Corner potential [59], originally proposed by Zewdie [11]. To the extent of the author's knowledge gained after examining all the literature that cited the foundational work [84, 11, 81] and some of the work [82, 85, 86] that built upon the foundation, this potential has not been used until present for simulating liquid crystal-nanoparticle mixtures.

Chapter 4

The Development and Behaviour of the Pairwise Potential

In this chapter, a number of important results are presented. First, there is a thorough discussion in section 4.1 of the procedure employed in fitting the range and strength parameters. This discussion finishes by presenting the resulting mesogen shape in figure 4.2 and the potential curves in figure 4.3. Next, sections 4.2.2 and 4.2.3 present and discuss the results of two studies conducted with the fitted mesogens and potential energy formulation. Both the thermodynamic observables and the domain snapshots are employed in the discussion of results.

4.1 Fitting of the Range and Strength Parameters

In order to conduct the simulations in this thesis, an approach similar to the one proposed by Zewdie [11, 81] was taken to derive the expressions for the range and strength parameters of our pairwise potential. However, Zewdie chose the shape anisotropy to be a fixed value, and did the fit only to one shape. Similarly, Zewdie fit the strength parameter to an existing parametrization of the Gay-Berne potential [11]. We decided to derive the expression for the shape symbolically, so that upon the variation of parameter values in the expressions for expansion coefficients different shape anisotropies could be captured without the need to go through the fitting procedure again. We followed the same rationale and methodology to derive an expression for the interaction strengths between different particle pairs in terms of parameters rather than fixed values.

4.1.1 Fitting the Range Parameter

In order to find an expansion of the range parameter (general form given in equation 3.4), we included only those S functions published by Stone [84] that did not change when the orientation of molecular direction vectors $\hat{u}_i$ and $\hat{u}_j$ and the intermolecular vector $\hat{r}_{ij}$ changed by 180°. This selection of S functions was made because the mesogens in this thesis were taken as nonpolar molecules. When a mesogen is represented by a centre of mass and an orientation vector, the assignment of direction is mandatory. However, since the molecules are nonpolar, parallel and antiparallel configurations of the molecules are absolutely equivalent. In addition, the particles we are considering are axially symmetric, which means that only the S functions with even indices are appropriate. As a result, the chosen S functions [84] (equations 4.1-4.8) and the expression for the range parameter scaled by σ_0 (equation 4.9) were as follows:

$$S_{000} = 1 \tag{4.1}$$

$$S_{202} = \frac{1}{2\sqrt{5}}\big(3(\hat{u}_i \cdot \hat{r}_{ij})^2 - 1\big) \tag{4.2}$$

$$S_{022} = \frac{1}{2\sqrt{5}}\big(3(\hat{u}_j \cdot \hat{r}_{ij})^2 - 1\big) \tag{4.3}$$

$$S_{220} = \frac{1}{2\sqrt{5}}\big(3(\hat{u}_i \cdot \hat{u}_j)^2 - 1\big) \tag{4.4}$$

$$\begin{aligned} S_{222} = \frac{1}{\sqrt{70}}\big(2 - 3(\hat{u}_i \cdot \hat{r}_{ij})^2 - 3(\hat{u}_j \cdot \hat{r}_{ij})^2 - 3(\hat{u}_i \cdot \hat{u}_j)^2 + \\ 9(\hat{u}_i \cdot \hat{r}_{ij})(\hat{u}_j \cdot \hat{r}_{ij})(\hat{u}_i \cdot \hat{u}_j)\big) \end{aligned} \tag{4.5}$$

$$S_{404} = \frac{1}{24}\big(35(\hat{u}_i \cdot \hat{r}_{ij})^4 - 30(\hat{u}_i \cdot \hat{r}_{ij})^2 + 3\big) \tag{4.6}$$

$$S_{044} = \frac{1}{24}\big(35(\hat{u}_j \cdot \hat{r}_{ij})^4 - 30(\hat{u}_j \cdot \hat{r}_{ij})^2 + 3\big) \tag{4.7}$$

$$S_{440} = \frac{1}{24}\big(35(\hat{u}_i \cdot \hat{u}_j)^4 - 30(\hat{u}_i \cdot \hat{u}_j)^2 + 3\big) \tag{4.8}$$

$$\begin{aligned} \frac{\sigma(\hat{u}_i, \hat{u}_j, \hat{r}_{ij})}{\sigma_0} = \big(\sigma_{000}S_{000} + \sigma_{202}S_{202} + \sigma_{022}S_{022} + \sigma_{220}S_{220} + \\ \sigma_{222}S_{222} + \sigma_{404}S_{404} + \sigma_{044}S_{044} + \sigma_{440}S_{440}\big) \end{aligned} \tag{4.9}$$

#	Configuration	$\hat{u}_i \cdot \hat{u}_j$	$\hat{u}_i \cdot \hat{r}_{ij}$	$\hat{u}_j \cdot \hat{r}_{ij}$	Value of $\sigma(\hat{u}_i, \hat{u}_j, \hat{r}_{ij})/\sigma_0$
1	cross	0	0	0	$2r_c$
2	side-by-side	1	0	0	$2r_c$
3	T configuration	0	1	0	$L_h + r_c$
4	T configuration	0	0	1	$L_h + r_c$
5	head-to-tail	1	1	1	$2L_h$
6	$cos^{-1}(\hat{u}_i \cdot \hat{r}_{ij}) = 60°$	1	0.5	0.5	$2r_c/\sqrt{1-0.5^2}$

Table 4.1: Constraints of the range parameter for cylinder-cylinder particle pair obtained by geometric arguments. For configuration #2 (side-by-side), $cos^{-1}(\hat{u}_i \cdot \hat{r}_{ij}) = 90°$, so configuration #6 is simply a variation of the side-by-side configuration. Note that two "T" configurations (#3 and #4) had to be used to ensure that the interactions within the cylinder-cylinder pair were symmetric and that cylinder "i" is interchangeable with cylinder "j". Consult figure 4.3 for a visualization of the configurations.

#	Constraint
7	$\sigma_{202} = \sigma_{022}$
8	$\sigma_{404} = \sigma_{044}$
9	$\sigma_{000} = (L_h + r_c)/2$

Table 4.2: Additional constraints for the cylinder-cylinder particle pair. Constraints #7 and #8 were obtained by symmetry argument, while constraint #9 was *ad hoc* (employed specifically for this problem in order to obtain a solution).

Representing the calamitic mesogen as a cylinder and taking L_h as 1/2 of the full length of the cylinder and r_c as the radius of the cylinder, the values of equation 4.9 (i.e. the distances between the two cylinders' centres) were found for specific combinations of $(\hat{u}_i \cdot \hat{u}_j)$, $(\hat{u}_i \cdot \hat{r}_{ij})$ and $(\hat{u}_j \cdot \hat{r}_{ij})$ (or in other words, specific configurations of the two cylinders) and recorded in table 4.1.

As one can easily see, table 4.1 contains less configurations than the total number of unknown σ coefficients in equation 4.9, resulting in an underdetermined linear system of equations. Therefore, it was necessary to impose additional constraints on the system, summarized in table 4.2.

The following system of linear equations had to be solved for the column vector of σ coefficients (exponent signifies the number (#) of the constraint from tables 4.1 and 4.2):

$$\begin{bmatrix} S^1_{000} & S^1_{202} & S^1_{022} & \dots & S^1_{044} & S^1_{440} \\ S^2_{000} & S^2_{202} & S^2_{022} & \dots & S^2_{044} & S^2_{440} \\ \vdots & \vdots & \vdots & \ddots & \vdots & \vdots \\ S^9_{000} & S^9_{202} & S^9_{022} & \dots & S^9_{044} & S^9_{440} \end{bmatrix} \begin{bmatrix} \sigma_{000} \\ \sigma_{202} \\ \vdots \\ \sigma_{044} \end{bmatrix} = \begin{bmatrix} \sigma^1(\hat{u}_i, \hat{u}_j, \hat{r}_{ij})/\sigma_0 \\ \sigma^2(\hat{u}_i, \hat{u}_j, \hat{r}_{ij})/\sigma_0 \\ \vdots \\ \sigma^9(\hat{u}_i, \hat{u}_j, \hat{r}_{ij})/\sigma_0 \end{bmatrix}$$

We used a symbolic mathematics library for the Python programming language, called "SymPy", to define the symbolic variables with the "symbols" function, form the equations with the "Eq" function and obtain an algebraic solution [85, 86] to the system with the "solve" function. The final expressions for σ coefficients on the right hand side of equation 4.9 were obtained in terms of L_h and r_c and summarized in table 4.3.

Having obtained the solution for the cylinder-cylinder particle pair, we used the same methodology to find the solutions to expansion coefficients for cylinder-sphere, sphere-cylinder and sphere-sphere range parameters in terms of L_h, r_c and r_s, where the latter is the radius of the spherical particle. In order to get a set of coefficients for the above three particle pairs that would be consistent with the coefficients for the cylinder-cylinder pair, we continued using equation 4.9 without any modifications to its form. Consideration of both sphere-cylinder and cylinder-sphere pairs was essential to ensuring that the interactions between a sphere and a cylinder-like particle were the same regardless of which of the two particles corresponded to index i and index j in our formulation.

However, for a sphere, the direction vector is undefined. Consequently, for sphere-cylinder, cylinder-sphere and sphere-sphere pairs, when an S function depended on the direction vector that would belong to a sphere, the corresponding expansion coefficient had to be constrained to zero. The sphere-sphere case was particularly simple - both particles were isotropic, so only the coefficient corresponding to the isotropic component of the range parameter expansion (σ_{000}) was allowed to be nonzero, and the interactions reduced from the Zewdie S function potential (equation 3.3) to the well-known Lennard-Jones potential (equation 2.3), with the range parameter $\sigma(\hat{u}_i, \hat{u}_j, \hat{r}_{ij})/\sigma_0$ set to always be equal to $2r_s$ because the spherical particles were identical.

Particle configurations and additional constraints on the system of linear equations for sphere-cylinder and cylinder-sphere pairs are summarized in tables 4.4-4.7 and the final solutions for the expansion coefficients of range parameters for the remaining three particle pairs are summarized in tables 4.8-4.10.

Based on these results, it was now possible to visualize the shape of the excluded volume between all particle pairs. However, only the cylinder-cylinder and cylinder-sphere shapes were of particular interest, because the excluded volume for sphere-cylinder pair is the

Coefficient	Solution
σ_{000}	$0.5 \times L_h + 0.5 \times r_c$
σ_{202}	$1.207 \times L_h - 1.031 \times r_c$
σ_{022}	$1.207 \times L_h - 1.031 \times r_c$
σ_{220}	$0.302 \times L_h - 2.250 \times r_c$
σ_{222}	0.0
σ_{404}	$0.914 \times L_h - 1.480 \times r_c$
σ_{044}	$0.914 \times L_h - 1.480 \times r_c$
σ_{440}	$-0.971 \times L_h + 7.246 \times r_c$

Table 4.3: Solutions for the expansion coefficients of the range parameter (equation 4.9) for cylinder-cylinder pair in terms of L_h and r_c.

#	Configuration	$\hat{u}_i \cdot \hat{u}_j$	$\hat{u}_i \cdot \hat{r}_{ij}$	$\hat{u}_j \cdot \hat{r}_{ij}$	Value of $\sigma(\hat{u}_i, \hat{u}_j, \hat{r}_{ij})/\sigma_0$
1	sphere-at-side	undefined	undefined	0	$r_s + r_c$
2	sphere-at-end	undefined	undefined	1	$r_s + L_h$
3	$cos^{-1}(\hat{u}_j \cdot \hat{r}_{ij}) = 60°$	undefined	undefined	0.5	$(r_s + r_c)/\sqrt{1 - 0.5^2}$

Table 4.4: Constraints of the range parameter for sphere-cylinder particle pair obtained by geometric arguments. Particle i corresponds to a sphere with radius r_s, particle j to a cylinder with radius r_c and half length L_h. Consult figure 4.3 for a visualization of the configurations. Additionally, consult section 2.1.3 and figure 2.11 of this thesis, since the "sphere-at-side" configuration corresponds to planar anchoring of mesogens towards nanoparticles and "sphere-at-end" corresponds to homeotropic anchoring. Note that configuration #3 represents a modification to configuration #1, where in the latter the sphere was exactly at the side of the cylinder-like particle.

Coefficient	Value
σ_{202}	0.0
σ_{220}	0.0
σ_{222}	0.0
σ_{404}	0.0
σ_{440}	0.0

Table 4.5: Additional constraints for the sphere-cylinder particle pair. These had to be imposed because here the sphere corresponded to particle index i; thus, the S functions complementary to the coefficients in this table would depend on molecular orientation vector $\hat{u}_i$, which is undefined for a sphere.

#	Configuration	$\hat{u}_i \cdot \hat{u}_j$	$\hat{u}_i \cdot \hat{r}_{ij}$	$\hat{u}_j \cdot \hat{r}_{ij}$	Value of $\sigma(\hat{u}_i, \hat{u}_j, \hat{r}_{ij})/\sigma_0$
1	sphere-at-side	undefined	0	undefined	$r_s + r_c$
2	sphere-at-end	undefined	1	undefined	$r_s + L_h$
3	$cos^{-1}(\hat{u}_j \cdot \hat{r}_{ij}) = 60°$	undefined	0.5	undefined	$(r_s + r_c)/\sqrt{1 - 0.5^2}$

Table 4.6: Constraints of the range parameter for cylinder-sphere particle pair obtained by geometric arguments. Particle i corresponds to a cylinder with radius r_c and half length L_h, particle j corresponds to a sphere with radius r_s. Consult figure 4.3 for a visualization of the configurations.

Coefficient	Value
σ_{220}	0.0
σ_{022}	0.0
σ_{222}	0.0
σ_{440}	0.0
σ_{044}	0.0

Table 4.7: Additional constraints for the cylinder-sphere particle pair. These had to be imposed because here the sphere corresponded to particle index j; thus the S functions complementary to the coefficients in this table would depend on molecular orientation vector $\hat{u}_j$, which is undefined for a sphere.

Coefficient	Solution
σ_{000}	$0.156 \times L_h + 0.954 \times r_c + 1.110 \times r_s$
σ_{202}	0.0
σ_{022}	$1.207 \times L_h - 1.031 \times r_c + 0.176 \times r_s$
σ_{220}	0.0
σ_{222}	0.0
σ_{404}	0.0
σ_{044}	$0.914 \times L_h - 1.480 \times r_c - 0.566 \times r_s$
σ_{440}	0.0

Table 4.8: Solutions for the expansion coefficients of the range parameter (equation 4.9) for the sphere-cylinder pair in terms of L_h, r_c, and r_s.

Coefficient	Solution
σ_{000}	$0.156 \times L_h + 0.954 \times r_c + 1.110 \times r_s$
σ_{202}	$1.207 \times L_h - 1.031 \times r_c + 0.176 \times r_s$
σ_{022}	0.0
σ_{220}	0.0
σ_{222}	0.0
σ_{404}	$0.914 \times L_h - 1.480 \times r_c - 0.566 \times r_s$
σ_{044}	0.0
σ_{440}	0.0

Table 4.9: Solutions for the expansion coefficients of the range parameter (equation 4.9) for the cylinder-sphere pair in terms of L_h, r_c, and r_s.

Coefficient	Solution
σ_{000}	$2 \times r_s$
σ_{202}	0.0
σ_{022}	0.0
σ_{220}	0.0
σ_{222}	0.0
σ_{404}	0.0
σ_{044}	0.0
σ_{440}	0.0

Table 4.10: Solutions for the expansion coefficients of the range parameter (equation 4.9) for the sphere-sphere pair in terms of r_s.

same as for cylinder-sphere pair, while the shape of the excluded volume between the two spheres was simply a sphere.

Figure 4.1 depicts the shape of the xy plane cross section of the excluded volume between the centres of cylinder-cylinder and cylinder-sphere particle pairs for $L_h = 2.5$, $r_c = 0.5$ and $r_s = 0.5$. To create that figure, the centre of particle i (cylinder) was fixed at the origin and its axis was oriented parallel to the z axis, and the second particle in the pair (cylinder or sphere) was rotated around the cylinder-like particle in the xy plane. In the case of cylinder-cylinder pair (blue line of figure 4.1), both cylinders were at all times oriented parallel to the z axis (directions of $\hat{u}_i$ and $\hat{u}_j$ were fixed). In the case of cylinder-sphere pair, the sphere did not have a direction (and thus all the terms of equation 4.9 that required $\hat{u}_j$ were eliminated by setting appropriate coefficients to zero, as per table 4.9). The rotation in the xy plane was accomplished by rotating the intermolecular vector $\hat{r}_{ij}$ in the xy plane for both particle pairs, since that was the only vector whose direction was allowed to vary. For each configuration of cylinder-cylinder and cylinder-sphere pairs (i.e. for each $\hat{r}_{ij}$ vector), the value of $\sigma(\hat{u}_i, \hat{u}_j, \hat{r}_{ij})/\sigma_0$ was calculated using equation 4.9 and coefficients of tables 4.3 and 4.9, respectively. Finally, for each configuration the length of the unit vector $\hat{r}_{ij}$ was multiplied by the value of $\sigma(\hat{u}_i, \hat{u}_j, \hat{r}_{ij})/\sigma_0$ and the x and y coordinates of the points to which the resulting vectors were pointing have been plotted in figure 4.1 as blue and red lines for cylinder-cylinder and cylinder-sphere pairs, respectively. Thus, when examining the lines plotted in figure 4.1, one should be mindful that the centre of one cylindrical particle is always at the origin in the figure and the centre of the other particle, whether a cylinder or a sphere, is located at any point on the blue (for cylinder-cylinder pair) and red (cylinder-sphere) lines. The reason why mesogens with smaller

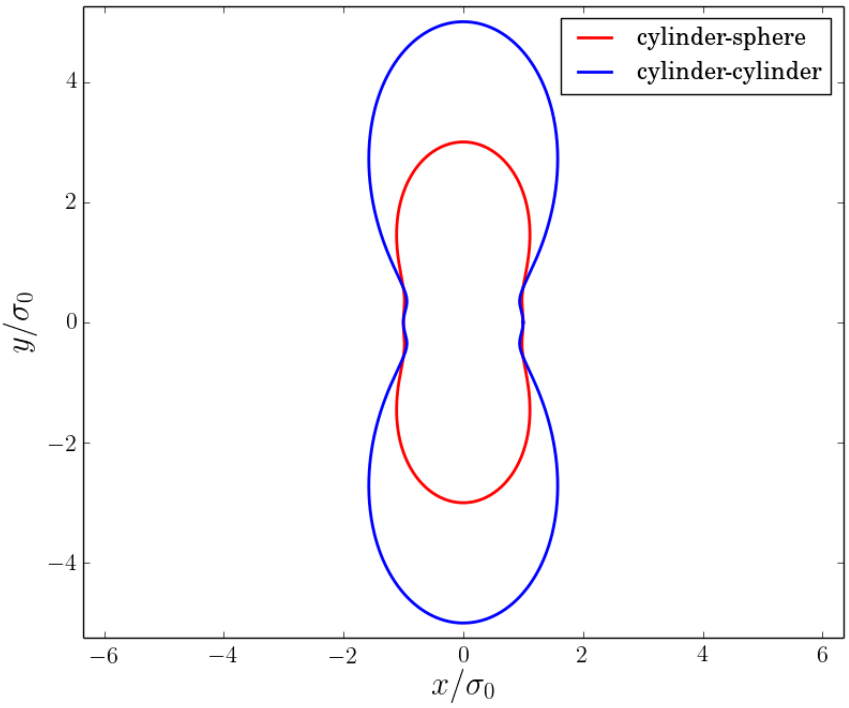

Figure 4.1: Cross section in the xy plane of the excluded volumes between cylinder-cylinder and cylinder-sphere particle pairs for $L_h = 2.5$, $r_c = 0.5$ and $r_s = 0.5$

L_h values have not been shown in this thesis is because during preliminary simulations conducted with mesogens of lower shape anisotropies ($2L_h/2r_c = 3.0$ and $2L_h/2r_c = 3.5$) no mesophase formation was observed.

Figure 4.2 was derived from figure 4.1 and it shows the shape of the cylinder-like particle ($L_h = 2.5$, $r_c = 0.5$) obtained by subtracting the contribution of particle j (cylinder with $L_h = 2.5$ and $r_c = 0.5$ or sphere with $r_s = 0.5$) from the excluded volume between the centres of mass of the two particles in the ij pair. For the cylinder-cylinder case, dividing every calculated value of $\sigma(\hat{u}_i, \hat{u}_j, \hat{r}_{ij})/\sigma_0$ by 2 before obtaining the x and y coordinates of the points and plotting them in the same way as described for figure 4.1 (i.e. through scaling the unit vector $\hat{r}_{ij}$ by $\sigma(\hat{u}_i, \hat{u}_j, \hat{r}_{ij})/2\sigma_0$) was all that was necessary to obtain the shape of the cylinder fixed at the origin (particle i), because the shape of the excluded volume between two identical cylinders is directly related to the shape of one cylinder-like molecule (through shrinking the former by a factor of 2 one can obtain the latter).

For the cylinder-sphere case, it was required first to subtract the radius of the sphere ($r_s = 0.5$) from every calculated $\sigma(\hat{u}_i, \hat{u}_j, \hat{r}_{ij})/\sigma_0$ and then find the x and y coordinates (through scaling the unit vector $\hat{r}_{ij}$ by the $(\sigma(\hat{u}_i, \hat{u}_j, \hat{r}_{ij})/\sigma_0 - r_s)$ value) and plot the results as described in figure 4.1. This result for cylinder-sphere was the same for different values of r_s as long as L_h and r_c values were kept constant.

Figure 4.2 made it apparent that the resulting particle was cylinder-like with $L_h = 2.5$ and $r_c = 0.5$ and had a dumbbell shape (and it was very similar to Zewdie's results [11] except that Zewdie used a shape anisotropy of 3 and we had it equal to 5). However, as in [11], the particle was not exactly a spherocylinder (a spherocylinder is a cylinder capped with a hemisphere at each of its ends), being wider than the specified diameter of $(2r_c = 1.0)$ in most points along the long axis. These imperfections in the fit can be attributed to the small number of terms included in the range parameter expansion; more terms would be necessary to obtain a more accurate representation of a spherocylinder. We considered the number of terms in the expansion and the result sufficient for the time being, similar to the path taken in [11, 81, 85].

Figure 4.2 also showed that there was a slight discrepancy between the cylinder-like particle's shape when it was deduced from cylinder-cylinder and cylinder-sphere particle pairs. When verifying Zewdie's results [11] in preparation for conducting the work described herein, the same methodology as proposed for creating figure 4.2 was used to plot the shape of the rod-like particle reported in [11], and a very similar discrepancy was found. Since we already imposed a sufficient number of constraints to solve the linear system composed of different values of S functions and $\sigma(\hat{u}_i, \hat{u}_j, \hat{r}_{ij})/\sigma_0$, we attribute the discrepancy to an insufficient number of terms in the expansion. Finally, since the excluded volumes between different particles will also be different, and since the definition of shape at the nanoscale is not the same as what it would be at the macroscale, perhaps it should not be surprising that the shape of particle i "seen" by different particles j would change slightly depending on the type of the probing particle j. The study of matter at the nanoscale, whether by experiment or simulation, is notorious for convoluting the properties of the observed system with the properties of the probe.

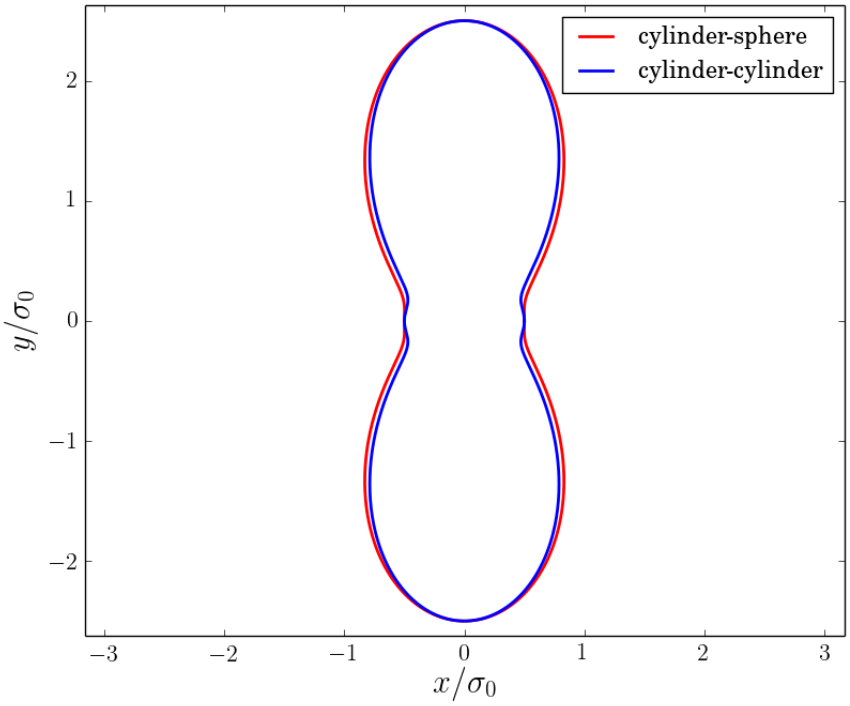

Figure 4.2: Cross section in the xy plane of the shape of the cylinder-like particle ($L_h = 2.5$, $r_c = 0.5$) obtained from the cylinder-cylinder and cylinder-sphere pairs.

4.1.2 Fitting the Strength Parameter

Using an isotropic strength parameter independent of cylinder-like particles' relative orientations did not result in formation of liquid crystal phases during preliminary runs of domains composed entirely of cylinder-like particles. Thus, it became apparent that it was necessary to fit the strength parameter to a set of values that depended on the relative orientation of the anisotropic mesogens.

Moreover, in order to increase the stability range of nematic phases, it is necessary to differentiate between "side-by-side" and "head-to-tail" configurations (see figure 4.3) of cylinder-like particles: the "side-by-side" configuration should be more made more stable than the "head-to-tail" configuration. This is common practice in literature [60, 11, 82, 3, 51] and was therefore implemented in this work. Additionally, in literature it is common practice to have the "T" and "cross" configurations less stable than the "side-by-side" configuration. Taking all of the above into account, we decided to use $\epsilon_{\parallel}$ and $\epsilon_{\perp}$ as the variables in terms of which to derive the strength parameter expansion coefficients. Since in "side-by-side" and "head-to-tail" configurations the particles are parallel to each other, we used $\epsilon_{\parallel}$ as the variable for these pairs' interaction strengths. Similarly, we used $\epsilon_{\perp}$ for "cross" and "T" configurations, since the particles there are perpendicular to each other. Again, doing the parametric fit allowed us to arrive at different strength parameter expansion coefficients without performing the fitting procedure - changing the values of $\epsilon_{\parallel}$ and $\epsilon_{\perp}$ was sufficient.

For simplicity, we decided to include terms of only up to second order in the proposed expression for the strength parameter expansion 4.10. The S functions were again chosen such that rotating the vectors $\hat{u}_i$, $\hat{u}_j$ and $\hat{r}_{ij}$ by 180° would not affect the results since the mesogens were considered to be nonpolar.

$$\frac{\epsilon(\hat{u}_i, \hat{u}_j, \hat{r}_{ij})}{\epsilon_0} = \left(\epsilon_{000}S_{000} + \epsilon_{202}S_{202} + \epsilon_{022}S_{022} + \epsilon_{220}S_{220} + \epsilon_{222}S_{222}\right) \tag{4.10}$$

The chosen constraints for equation 4.10 and the resulting solutions are summarized in tables 4.11 and 4.12, respectively. At this stage in our research, it was not deemed necessary to have the strength of interactions between cylinder-like and spherical particles depend on the orientation of the cylinder-like particle and the intermolecular vector. We postulated that the arrangement of spherical particles around the mesogens (or vice versa) would be controlled through the anisotropy of the excluded volume between them, somewhat similar to the reasoning employed in [85], where the same strength parameter was used to study disk-like particles of different shapes and the shapes alone had a profound effect

#	Configuration	$\hat{u}_i \cdot \hat{u}_j$	$\hat{u}_i \cdot \hat{r}_{ij}$	$\hat{u}_j \cdot \hat{r}_{ij}$	Value of $\epsilon(\hat{u}_i, \hat{u}_j, \hat{r}_{ij})/\epsilon_0$
1	side-by-side	1	0	0	$\epsilon_\parallel$
2	head-to-tail	1	1	1	$0.25\epsilon_\parallel$
3	cross	0	0	0	$\epsilon_\perp$
4	T configuration	0	1	0	$0.5\epsilon_\perp$
5	T configuration	0	0	1	$0.5\epsilon_\perp$

Table 4.11: Constraints of the strength parameter (equation 4.10) for the cylinder-cylinder particle pair. Note the usage of two "T" configurations once again, due to the same rationale as when deriving the range parameter expansion coefficients for this particle pair (to ensure that the cylinder-like particles are interchangeable - see table 4.1).

Coefficient	cylinder-cylinder	other pairs
ϵ_{000}	$0.25 \times \epsilon_\parallel + 0.444 \times \epsilon_\perp$	1.0
ϵ_{202}	$-0.373 \times \epsilon_\parallel - 0.248 \times \epsilon_\perp$	0.0
ϵ_{022}	$-0.373 \times \epsilon_\parallel - 0.248 \times \epsilon_\perp$	0.0
ϵ_{220}	$1.118 \times \epsilon_\parallel - 0.994 \times \epsilon_\perp$	0.0
ϵ_{222}	$-0.697 \times \epsilon_\parallel + 0.930 \times \epsilon_\perp$	0.0

Table 4.12: Solutions for the expansion coefficients of the strength parameter (equation 4.10) for all four particle pairs in terms of $\epsilon_\parallel$ and $\epsilon_\perp$. Note that "other pairs" denotes sphere-cylinder, cylinder-sphere and sphere-sphere particle pairs. Interaction strengths for these three pairs were chosen to be identical.

on mesophase formation. Thus, in table 4.12 the last column represents solutions for all of the remaining particle pairs. Experiments [25, 26, 27] show that mesogens tend to orient themselves homeotropically with respect to the dopant nanoparticles, but conducting investigations into this matter via simulations was left outside the scope of this thesis due to time constraints.

At this point, having obtained solutions for the range and strength parameter expansion coefficients for all particle pairs, it was possible to visualize the potential energy curves between them, similar to how it has been done in figure 2.17. Figure 4.3 contains these results.

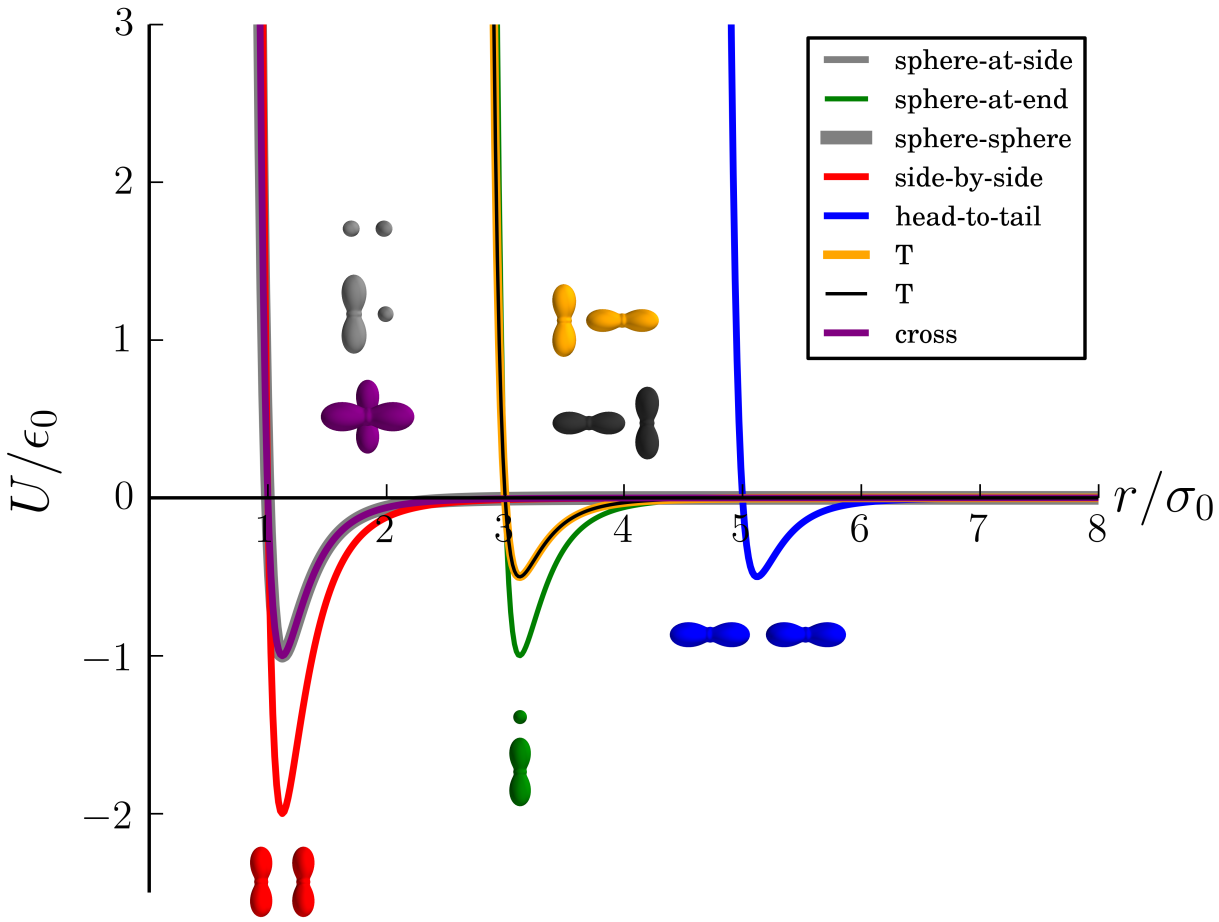

Figure 4.3: These curves represent the potential energy between different particle pairs and particle configurations at varying separation distances. The curves and the corresponding particle pairs have been portrayed using the same colours. Half-length L_h of the cylinder-like particle was set to 2.5, radius r_c of the cylinder-like particle was set to 0.5 and radius r_s of the spherical particle was also set to 0.5 (similar to one of the cases studied in [80]). In order to mimic the relative potential well depths of the Gay-Berne potential depicted in figure 3a of [3] and figure 3 of [51] (which is figure 2.17 of this thesis), $\epsilon_{\parallel}$ was set to 2.0 and $\epsilon_{\perp}$ was set to 1.0

4.2 Simulation Studies of Pure LC Domains

4.2.1 Simulation Conditions

To mitigate the issue of introducing a truncation error into simulations by using a cutoff radius for the pair potential, the cutoff was chosen to be sufficiently large so that the potential energy at that separation would be very close to zero (the same approach has been taken in [82], as indicated in figure 2 of that paper). Thus, the cutoff radius of $7.0\sigma_0$ was chosen for the simulations described in this thesis since it satisfied the aforementioned requirement, as can be observed in figure 4.3 (when $r/\sigma_0 = 7.0$, U/ϵ_0 is essentially zero). However, having the cutoff radius of $7.0\sigma_0$ implied that the smallest possible simulation domain size at any point in the simulation (and not only at the start, since the isobaric-isothermal NPT ensemble allows domain volume to vary) would need to be greater than $14.0\sigma_0$ in every dimension in order for us to be able to use periodic boundary conditions and avoid infinite summations [67].

The initial simulation domain needed to be fully occupied by the particles since a non-optimal fill would result in a gap between the particles and at least one of the faces of the cubic domain, and using periodic boundary conditions would cause the gap to also be periodic. Such an initial configuration would not be physical and had to be avoided. Since the rod-like particles had the length $2L_h = 5.0\sigma_0$ and the diameter $2r_c = 1.0\sigma_0$, simulation domain size in every dimension had to be a multiple of $5.0\sigma_0$ (and greater than $14.0\sigma_0$). To make sure that the domain, even if it decreased in volume, would never become smaller than $14.0\sigma_0 \times 14.0\sigma_0 \times 14.0\sigma_0$, a domain with dimensions of $25.0\sigma_0 \times 25.0\sigma_0 \times 25.0\sigma_0$ was used, with $N = 3125$ particles ($25 \times 25 \times 5$ particles, all initially arranged on a perfect lattice and oriented in the z direction, in order to achieve the optimal fill). Throughout all simulations presented in this thesis the domain was kept cubic and the maximum change in domain volume that was accepted or rejected via the Monte Carlo algorithm (described in section 2.5) was $781.25\sigma_0^3$, which comprised 5% of the initial domain volume. Every simulation presented herein was started from this perfect crystal arrangement and "melted" to find an equilibrium configuration at the preset temperature.

On every domain sweep, $N+1$ attempts were made to alter the domain, where N is the number of particles. On every attempt, a random integer greater than zero and less than or equal to $N + 1$ was obtained and if it was between 1 and N, inclusive, it was used as the index of the particle that was subsequently displaced and reoriented in the attempted Monte Carlo move. If the integer was $N+1$, a domain volume perturbation was performed as described above (and domain energy was rescaled as per equation 2.15). Making the

choice of the type of move (volume or particle) and the particle index random allowed our simulations to obey the "detailed balance" condition (discussed in section 2.5).

Verlet lists [67] were utilized in order to keep track of each particle's neighbours in the pairwise potential energy calculation. In particle moves, particles could be displaced by up to 0.25 in each of x, y, z directions, and their orientations were perturbed by $\pi/8$ radians in a random direction. The latter restriction on reorientation was implemented in an attempt to increase the low acceptance ratio by preventing large overlaps between cylinder-like particles from occurring due solely to reorientation.

The equilibrium of the NPT Metropolis Monte Carlo simulations performed herein was ensured through a visual inspection of the energy, volume and nematic order parameter evolution plots. All of those plots exhibited asymptotic convergence behaviour, and after the simulation has been running for a sufficiently long time (a few days to a week) and the plateau regions were reached on all of the aforementioned plots, the simulations were stopped and their results were processed. The code was set to print out simulation data (domain energy and volume values, as well as domain configuration snapshots) after every 1000 domain sweeps (the sweeps were described earlier). The energy value at a certain temperature and pressure was calculated by taking the last 5 data points printed out by the simulation and averaging them. The same procedure was applied to find the domain volume at a certain temperature and pressure. For the nematic order parameter, the last 5 domain snapshots were analyzed separately and nematic order parameters were calculated for them separately, after which these 5 values were averaged and reported as the order parameter at a given temperature and pressure. When the simulation domain was comprised of a mixture of mesogens and spherical particles, only the mesogens were considered when calculating the nematic order parameter value.

One of the challenges that has not been truly overcome in this work (even with the restricted rotation of particles) was the low acceptance ratio of particle moves, which extended the CPU time needed to obtain results. The ratio varied from 0.7 % to 10 % for pure mesogenic domain, increasing at higher temperatures (indicative of a less ordered phase existing at those conditions than at lower temperatures). However, in all simulations having approximately 9×10^6 accepted particle moves for $N = 3125$ was more than sufficient to observe the convergence of the domain enthalpy (i.e. domain energy at constant pressure and variable volume calculated using the pair potential), domain volume and domain order parameter values.

In order to define the values for reduced temperature and pressure at which to conduct the simulations, length and energy scaling parameters had to be decided upon. Length scaling of $\sigma_0 = 5.0\times10^{-10}\ m$ was chosen, as in [82] and [91], since it is to a good approxima-

tion the diameter of the benzene rings in the rigid core of calamitic mesogens such as 5CB and 8CB. The diameter of the benzene ring corresponds to the diameter of the cylinder-like shape used to represent these mesogens when performing coarse-graining. Energy scaling of $\epsilon_0 = 4.0 \times 10^{-21}\ J$ was used in the simulations presented in this thesis. It is on the same order of magnitude as in [82, 91] and other published work, and it also allowed us to arrive at reasonable physical values that would correspond to the reduced temperature and pressure (the discussion in Appendix B contains more information regarding this matter). Based on these chosen scaling units, reduced pressure of 0.003125 corresponded to 1 *bar* as per equation B.1 in Appendix B. Reduced temperature $T^* = 0.7$ corresponded to real temperature $T = 202.8\ K$ $(-70.3\ ^\circ C)$, 1.4 to $405.6\ K$ $(132.5\ ^\circ C)$, and 1.7 to $492.5\ K$ $(219.4\ ^\circ C)$, as per equation B.2 in Appendix B. The first study (section 4.2.2) was done with a domain comprised purely of 3125 mesogens at reduced temperatures ranging from 0.7 to 1.4, inclusive, in increments of 0.05. The second study (section 4.2.3) was conducted with 3125 mesogens at the reduced temperatures between 0.7 and 1.7, inclusive, again in increments of 0.05. The temperature range was extended for the latter study because a liquid crystal to isotropic liquid transition was not clearly observed in the former study.

4.2.2 The Behaviour Exhibited by the Potential Upon Variation of the Strength Parameter Expansion Coefficients

The study conducted in this section was performed in order to observe the phases that could be exhibited by the potential we have developed. The results of these simulations would also be highly beneficial for selecting a set of parameters at which to conduct simulations of liquid crystal-nanoparticle (LC-NP) mixtures.

Of particular interest was the effect of the strength parameter on the phases exhibited by the potential. In order to examine the effect, $\epsilon_\perp$ was fixed to 1.0 and $\epsilon_\parallel/\epsilon_\perp$ ratio was varied from 1.0 to 2.0 in increments of 0.25. The strength parameter expansion coefficients were calculated as summarized in table 4.12 for each $\epsilon_\parallel/\epsilon_\perp$ ratio. Please refer to figure 4.3 for potential energy plots between cylinder-like particles when $\epsilon_\parallel/\epsilon_\perp$ ratio = 2.00 and to figures C.1-C.4 in Appendix C for the cases when $\epsilon_\parallel/\epsilon_\perp$ ratios are between 1.00 and 1.75, inclusive.

Figures 4.4-4.6 summarize the results obtained from conducting the simulations. The domain energy calculated between all particle pairs using the pair potential in its dimensionless form (i.e. equation 3.3 divided by ϵ_0) was averaged between the last 5 ensembles and divided by the number of mesogens (N) in the domain to arrive at a quantity referred to hereafter as "enthalpy per particle" (h^*). The number density ρ^* was calculated by

dividing N by the ensemble-averaged domain volume V^*, where the average was again taken between the last 5 ensembles (note that the asterisk indicates reduced units and dimensionless quantities). Finally, the nematic order parameter s was calculated according to equation 2.1 for the last 5 ensembles of each simulation and averaged.

In general terms, the trends in h^* (figure 4.4), ρ^* (figure 4.5) and s (figure 4.6) were as expected. Enthalpy per particle became less negative with greater temperatures, indicating a less stable phase. The number density diminished with rising temperature. Nematic order decreased with greater temperature, as expected for liquid crystals. However, because of the fluctuations in s it was not clear at which temperature the nematic-isotropic transition occurred. Also, the number density decreased linearly with increasing temperature, exhibiting a behaviour resembling a gas rather than a liquid.

In addition, it can be observed from all three figures that increasing the $\epsilon_{\parallel}/\epsilon_{\perp}$ ratio has a stabilizing effect on the simulated substance. At higher ratios enthalpy is more negative, number density decreases to a lesser extent (indicating greater intermolecular attraction) and the order parameter has higher values at low temperatures (showing that orientational ordering is preferred to disorder). The value of s for greater $\epsilon_{\parallel}/\epsilon_{\perp}$ ratios also continues to be higher than for lesser $\epsilon_{\parallel}/\epsilon_{\perp}$ ratios as temperature rises.

The simulations with $\epsilon_{\parallel}/\epsilon_{\perp}$ ratio of 2.0 exhibited a behaviour in ρ^* and s that appeared to differ from other simulation sets. The drop in the number density was the smallest for $\epsilon_{\parallel}/\epsilon_{\perp} = 2.0$, with ρ^* staying fairly constant up to $T^* = 0.9$ in figure 4.5 and then proceeding to decline at a steady rate. $T^* = 0.9$ was also the point after which in figure 4.6 the decline in s became less rapid at subsequent temperatures for the data set with $\epsilon_{\parallel}/\epsilon_{\perp} = 2.0$.

Based on the aforementioned observations, it was decided to use the potential with $\epsilon_{\parallel}/\epsilon_{\perp} = 2.0$ as the basis for conducting simulations of LC-NP mixtures. It appeared that this $\epsilon_{\parallel}/\epsilon_{\perp}$ ratio exhibited a phase transition on the selected temperature range because it had the greatest decrease in the nematic order parameter and a peculiar behaviour of number density switching from being constant up to $T^* = 0.9$ to steadily decreasing afterwards.

It is worth mentioning that $\epsilon_{\parallel}/\epsilon_{\perp} = 2.0$ yielded a potential that is quite similar in appearance to a commonly reported parametrization of the Gay-Berne potential (compare figure 4.3 to figure 2.17).

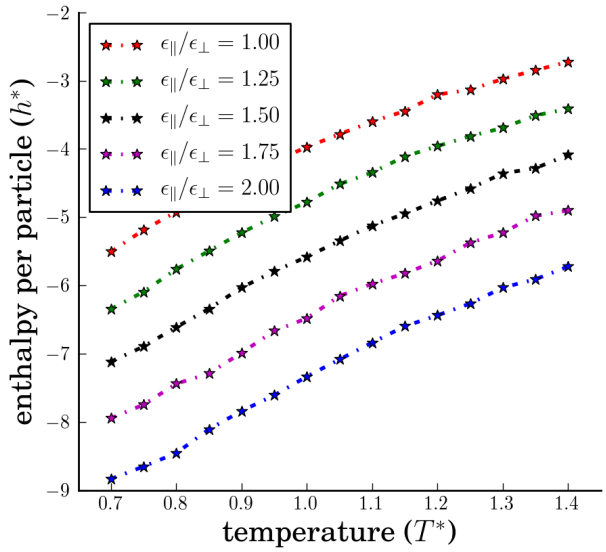

Figure 4.4: The effect of varying $\epsilon_\parallel/\epsilon_\perp$ ratio and temperature on the enthalpy per particle for pure LC domain ($L_h = 2.5$, $r_c = 0.5$, $N = 3125$, $P = 0.003125$)

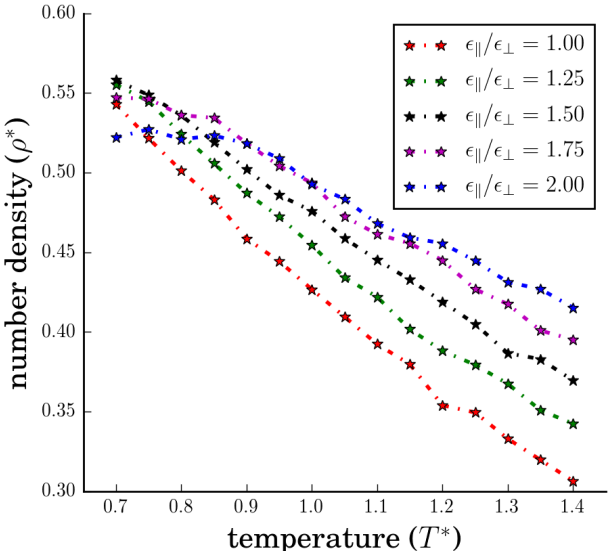

Figure 4.5: The effect of varying $\epsilon_\parallel/\epsilon_\perp$ ratio and temperature on the number density for pure LC domain ($L_h = 2.5$, $r_c = 0.5$, $N = 3125$, $P = 0.003125$)

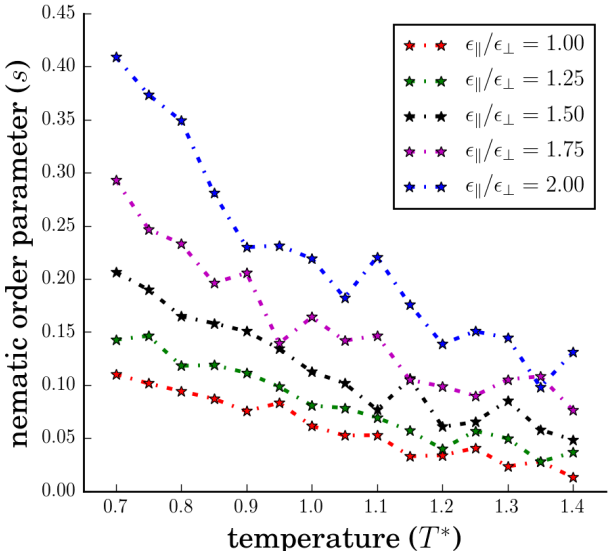

Figure 4.6: The effect of varying $\epsilon_\parallel/\epsilon_\perp$ ratio and temperature on the nematic order parameter s for pure LC domain ($L_h = 2.5$, $r_c = 0.5$, $N = 3125$, $P = 0.003125$)

4.2.3 The Behaviour of the Pairwise Potential with $\epsilon_\parallel = 2.0$ and $\epsilon_\perp = 1.0$ Upon T^* Variation

The potential with $\epsilon_\parallel/\epsilon_\perp = 2.0$ was used to conduct simulations of pure LC on an expanded temperature range from 0.7 to 1.7, inclusive, and the resulting data was analyzed in greater detail with the intention of observing the possible phase transitions. Enthalpy per particle h^* was once again calculated according to the same ensemble averaging procedure as described in sections 4.2.1 and 4.2.2, but now for temperatures of up to 1.7 (in reduced units). The trend of h^* becoming less negative with rising T^* continued, as can be seen from figure 4.7. However, no sudden changes in enthalpy per particle were observed except for a very small jump between $T^* = 0.85$ and $T^* = 0.9$, showing that a phase transition likely did not occur.

The statement about peculiar domain behaviour at $T^* = 0.9$ is supported by the behaviour of ρ^* in figure 4.8 (note the change at $T^* = 0.9$ from a plateau to a steady decline) and the change in behaviour of s in figure 4.10 (the decline in s seems to have become less rapid after $T^* = 0.9$), but this is not evidence enough to conclude that a phase transition occurred at that temperature.

Additionally, by inspecting snapshots in figures 4.11 (taken at $T^* = 0.85$) and 4.12 (taken at $T^* = 1.1$) it can be observed qualitatively that there is a decrease in orientational order from the former figure to the latter, since there are more particles out of alignment with the director (indicated by darker colours) in figure 4.12. Clearly, the order in the domain decreases with temperature, but there was no temperature that triggered a sudden transition. Instead, a gradual decline has been found. Moreover, the radial distribution function plot (figure 4.9) also exhibits a change because of the presence of sharp peaks at $r \approx 1.0$, $r \approx 3.0$ and $r \approx 10.0$ prior to $T^* = 0.9$ and somewhat less pronounced peaks at those locations at higher temperatures. Interestingly, the first peak location approximately corresponds to $2r_c$ (contact distance for two cylinder-like particles in the "side-by-side" configuration), the second peak is roughly $r_c + L_h$ (the contact distance in a "T" configuration) and the last peak corresponds to $2(2L_h)$, which is twice the length of the cylinder-like mesogen. The fact that the peaks at these values of r, especially at $r \approx 1.0$ and $r \approx 10.0$, are quite pronounced at lower temperatures is strong indication of long-range order and thus the possible formation of a smectic phase at those temperatures.

It is notable that even at the temperature of 1.7 there are weak peaks in the radial distribution function (figure 4.9) at $r \approx 3.0$ and $r \approx 10.0$. This indicates that even at this relatively high temperature the domain is not in a completely isotropic phase regardless of the fact that the orientational order parameter s (figure 4.10) has decreased substantially from its maximum value. Increasing the temperature further is necessary to make the domain fully isotropic, but it was not done in this study due to time limitations.

Finally, the nematic order parameter s was expected to provide deeper insight into the phase transitions, but unfortunately it did not give clear indication of the former. The orientational order parameter s was calculated according to the equation 2.1 and the ensemble averaging procedure described in sections 4.2.1 and 4.2.2. It can be observed that the order parameter s fluctuated with rising temperature (figure 4.10). These fluctuations are indicative of finite size effects; in fact, s cannot be zero even when the domain is in the isotropic phase because of finite size effects [85]. Another possible cause for fluctuations of s may be due to how the simulations were conducted: instead of finding an equilibrium configuration at a particular temperature and then using it as an initial condition for a simulation at a successive temperature, each simulation was started from a perfect crystal that "melted" due to the imposed ambient temperature. It would likely be beneficial to use the successive heating or cooling approach instead of starting from the perfect crystal to the end of obtaining data with lower fluctuations of s.

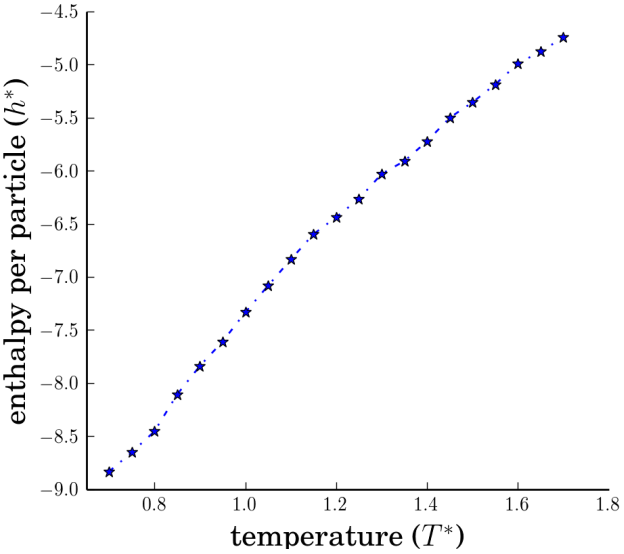

Figure 4.7: The effect of varying simulation temperature on the enthalpy per particle for pure LC domain ($L_h = 2.5$, $r_c = 0.5$, $N = 3125$, $\epsilon_{\parallel}/\epsilon_{\perp} = 2.0$, $P = 0.003125$)

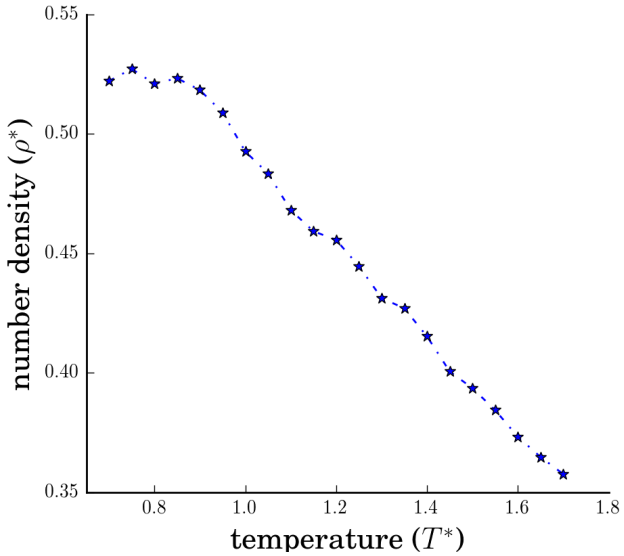

Figure 4.8: The effect of varying simulation temperature on the number density for pure LC domain ($L_h = 2.5$, $r_c = 0.5$, $N = 3125$, $\epsilon_{\parallel}/\epsilon_{\perp} = 2.0$, $P = 0.003125$)

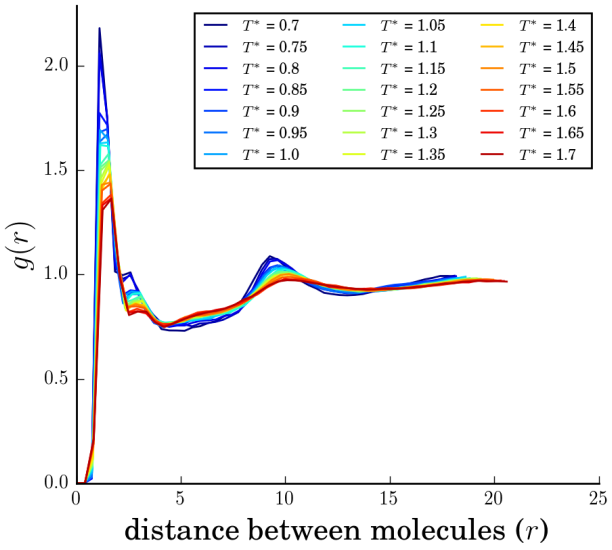

Figure 4.9: The effect of varying simulation temperature on the radial distribution function $g(r)$ for pure LC domain ($L_h = 2.5$, $r_c = 0.5$, $N = 3125$, $\epsilon_{\|}/\epsilon_{\perp} = 2.0$, $P = 0.003125$)

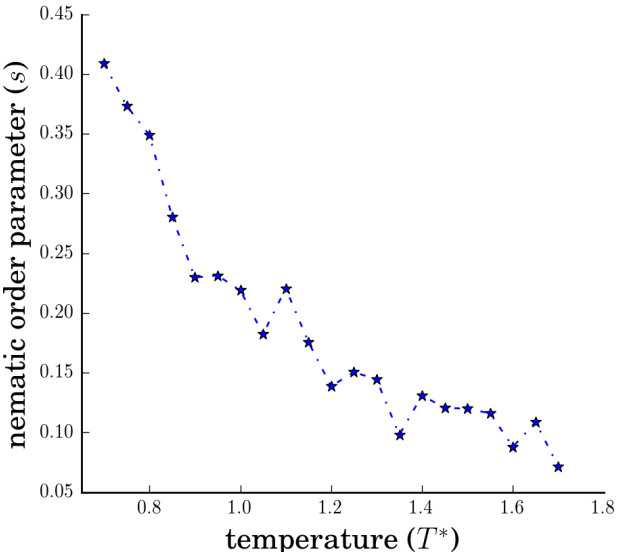

Figure 4.10: The effect of varying simulation temperature on the nematic order parameter s for pure LC domain ($L_h = 2.5$, $r_c = 0.5$, $N = 3125$, $\epsilon_{\|}/\epsilon_{\perp} = 2.0$, $P = 0.003125$)

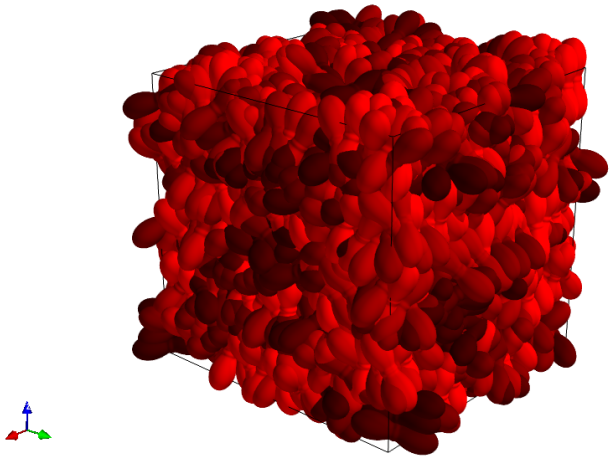

Figure 4.11: Snapshot of pure LC domain at $T^* = 0.85$ ($L_h = 2.5$, $r_c = 0.5$, $N = 3125$, $\epsilon_{\parallel}/\epsilon_{\perp} = 2.0$, $P = 0.003125$)

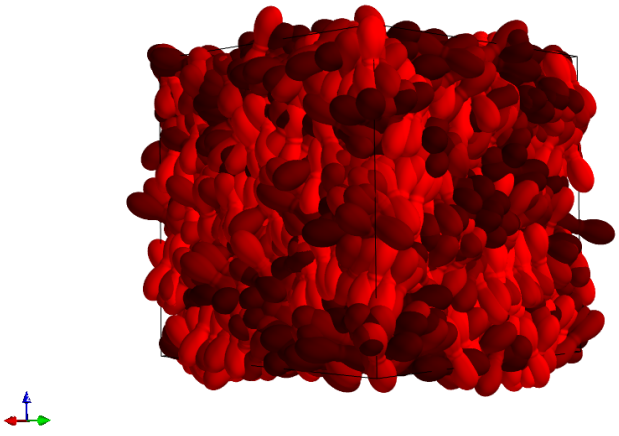

Figure 4.12: Snapshot of pure LC domain at $T^* = 1.1$ ($L_h = 2.5$, $r_c = 0.5$, $N = 3125$, $\epsilon_{\parallel}/\epsilon_{\perp} = 2.0$, $P = 0.003125$)

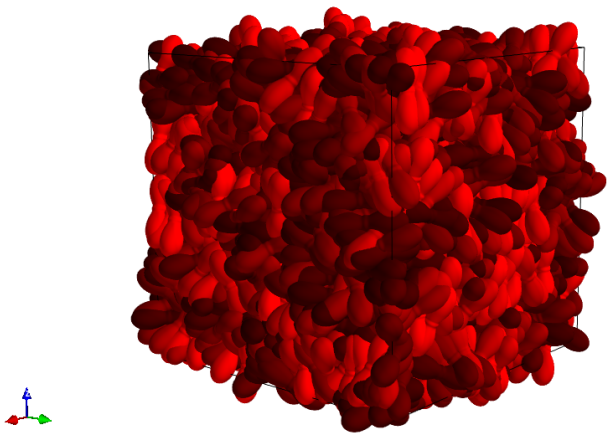

Figure 4.13: Snapshot of pure LC domain at $T^* = 1.7$ ($L_h = 2.5$, $r_c = 0.5$, $N = 3125$, $\epsilon_{\parallel}/\epsilon_{\perp} = 2.0$, $P = 0.003125$)

Chapter 5

Simulations of LC-NP Mixtures

In this chapter the results of the studies of liquid crystal-nanoparticle mixtures are presented and discussed. Section 5.1 examines the phase diagram with the nematic order parameter calculated at various temperatures and nanoparticle number fractions. Section 5.2 examines the heterogeneous radial distribution function plots and the corresponding snapshots for the same simulation data as discussed in section 5.1.

5.1 The Resulting Phase Diagrams

Using the same simulation conditions as for the pure LC domain studied in section 4.2.3 and the potential energy formulation as shown in figure 4.3, simulations were conducted where spherical particles with $r_s = 0.5$ were substituted for the cylinder-like particles in the domain of 3125 total particles. For each simulation, the initial configuration of the domain consisted of cylinder-like particles arranged in a perfect lattice with their long axes oriented along the z direction, with the spherical particles dispersed randomly throughout the domain. The number fractions (f) of spheres (simulated nanoparticles, "NPs" for short) ranged from 0.0 to 0.65 in increments of 0.05 between simulation sets.

A phase diagram has been constructed using colour to represent the values of the order parameter s. For the phase diagram, the order parameter s has been multiplied by the number density of mesogens (N_{LC}/V^*, where V^* is the ensemble averaged domain volume in reduced units) to account for the fact that a domain with a lower number fraction of mesogens will exhibit less overall order than a pure LC domain.

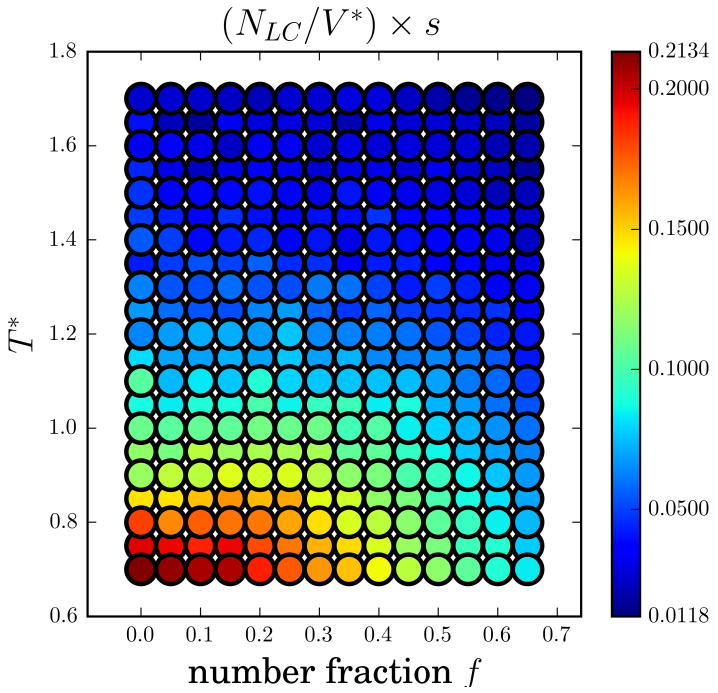

Figure 5.1: The effect of varying simulation temperature T^* and nanoparticle number fraction f on $(N_{LC}/V^*) \times s$ for LC-NP mixture ($L_h = 2.5$, $r_c = 0.5$, $r_s = 0.5$, $N = 3125$, $\epsilon_{\parallel}/\epsilon_{\perp} = 2.0$, $P = 0.003125$).

Construction of the nematic phase diagram (figure 5.1) revealed an interesting aspect of these LC-NP mixtures: even though higher NP number fractions serve to decrease orientational order in general, there appears to be some stabilizing effect on the nematic order at T^* ranging from 0.85 to 0.9 and f between 0.05 and 0.25, inclusive. If one were to fix the T^* value at 0.85 or 0.9 and follow on figure 5.1 in the direction of increasing f, it appears that there is an increase in s before it eventually decreases at $f > 0.25$. A possible explanation of this is formation of clusters with strong orientational order due to micro phase separation between mesogens and nanoparticles.

5.2 The Resulting Radial Distribution Functions and Domain Snapshots

In an attempt to further elucidate the behaviour of LC-NP mixtures, "heterogeneous" RDF plots were constructed between only mesogens (LC-LC), mesogens and nanoparticles (LC-NP), and only nanoparticles (NP-NP), similar to the ideas presented in [77, 108]. It was hypothesized that multiple peaks in the LC-LC radial distribution function ($g(r)$) would imply smectic layering of the liquid crystal. It was also put forth that multiple peaks in the NP-NP $g(r)$ would indicate phase separation and agglomeration of NPs at certain distances within the domain.

Indeed, figures 5.2, 5.4 and 5.6 indicate multiple peaks in each of LC-LC, LC-NP and NP-NP curves. Interestingly, it seems that the peaks and valleys in the three curves of each plot complement each other. When one curve has a depression, another exhibits a peak, indicating that where space has been vacated by, for instance, mesogens, it has been filled by nanoparticles (and vice versa).

It appears that all LC-NP curves have a smaller peak at $r \approx 2.5$ and a larger peak at $r \approx 6.0$. The location of these peaks does not seem to be influenced by f or T^*, possibly indicating preferred locations of clusters of spheres around the mesogens within the domain. Since f does not shift the location of the peaks, though it does alter their shape by widening the peaks at higher f values, it may be indicative of nanoparticle cluster growth at the same locations.

Based on observations of domain snapshots in figures 5.3, 5.5 and 5.7, the hypothesis that NPs were not mixing with the mesogens was corroborated by qualitative appearance of the domains. An explanation of this behaviour can be found in figure 4.3. It appears that this phase separation occurs because the mesogens are much more stable when close to each other in a side-by-side configuration than in any other configuration with each other or with a spherical nanoparticle. Consequently, in order to increase the solubility of nanoparticles in the liquid crystal it would be necessary to increase the ϵ_{000} coefficient of the strength parameter expansion for sphere-cylinder, cylinder-sphere and sphere-sphere pairs from 1.0 as it is in table 4.12 to a greater value, for instance 2.0, to match the stability of cylinder-cylinder pair in the side-by-side configuration.

Keeping in mind that the domain size is quite small when compared to macroscopic scales (see Appendix A for a more in-depth discussion), it can only be concluded that micro phase separation has been observed. If the domain were simply duplicated to match macroscopic scales, most likely it would appear as a uniform mixture of mesogens and nanoparticles without any macro scale phase separation.

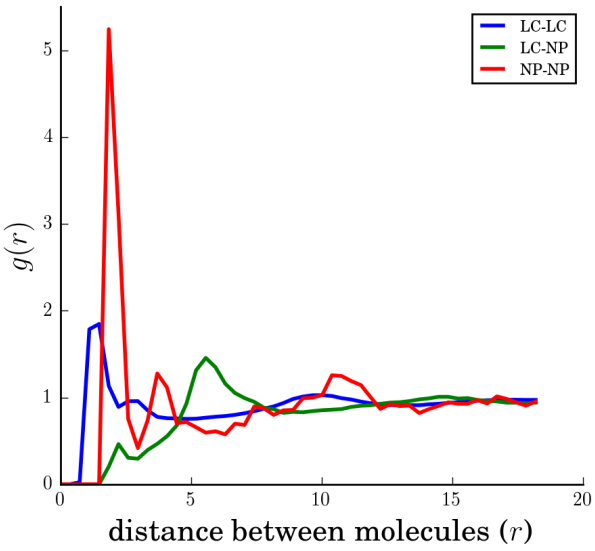

Figure 5.2: Heterogeneous radial distribution function for LC-NP domain at $T^* = 0.85$ and $f = 0.05$ ($L_h = 2.5$, $r_c = 0.5$, $r_s = 0.5$, $\epsilon_{\parallel}/\epsilon_{\perp} = 2.0$, $N = 3125$, $P = 0.003125$)

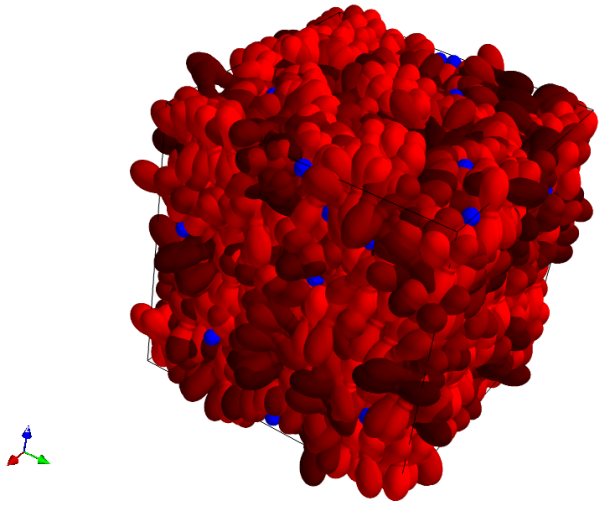

Figure 5.3: Snapshot of LC-NP domain at $T^* = 0.85$ and $f = 0.05$ ($L_h = 2.5$, $r_c = 0.5$, $r_s = 0.5$, $\epsilon_{\parallel}/\epsilon_{\perp} = 2.0$, $N = 3125$, $P = 0.003125$)

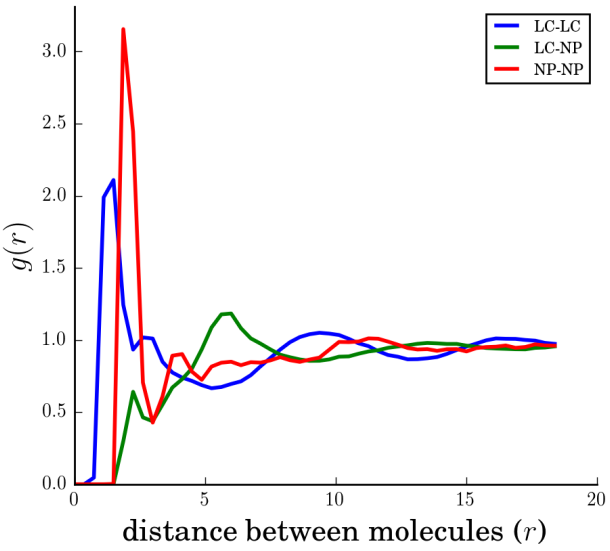

Figure 5.4: Heterogeneous radial distribution function for LC-NP domain at $T^* = 0.9$ and $f = 0.25$ ($L_h = 2.5$, $r_c = 0.5$, $r_s = 0.5$, $\epsilon_{\parallel}/\epsilon_{\perp} = 2.0$, $N = 3125$, $P = 0.003125$)

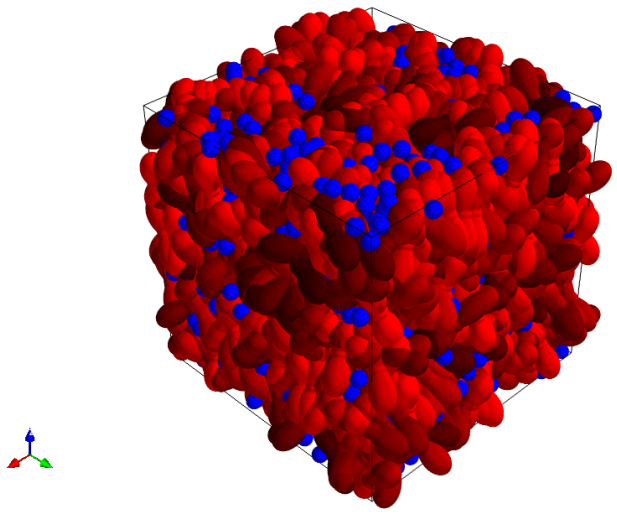

Figure 5.5: Snapshot of LC-NP domain at $T^* = 0.9$ and $f = 0.25$ ($L_h = 2.5$, $r_c = 0.5$, $r_s = 0.5$, $\epsilon_{\parallel}/\epsilon_{\perp} = 2.0$, $N = 3125$, $P = 0.003125$)

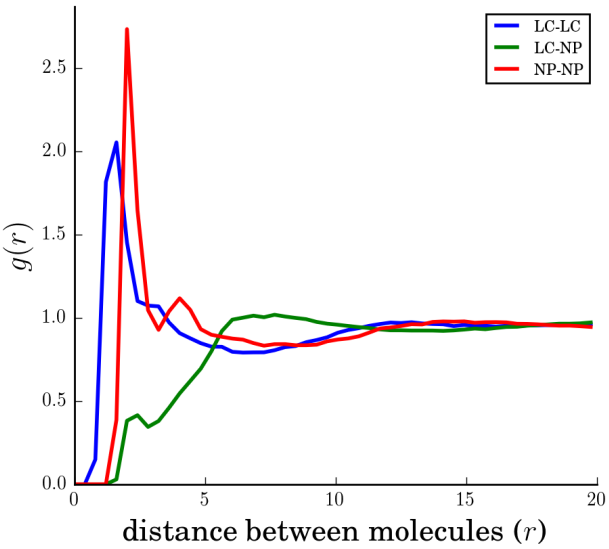

Figure 5.6: Heterogeneous radial distribution function for LC-NP domain at $T^* = 1.7$ and $f = 0.65$ ($L_h = 2.5$, $r_c = 0.5$, $r_s = 0.5$, $\epsilon_{\parallel}/\epsilon_{\perp} = 2.0$, $N = 3125$, $P = 0.003125$)

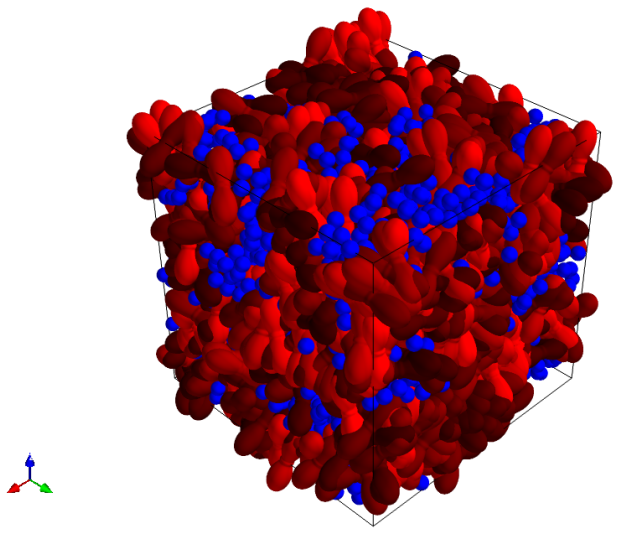

Figure 5.7: Snapshot of LC-NP domain at $T^* = 1.7$ and $f = 0.65$ ($L_h = 2.5$, $r_c = 0.5$, $r_s = 0.5$, $\epsilon_{\parallel}/\epsilon_{\perp} = 2.0$, $N = 3125$, $P = 0.003125$)

Chapter 6

Conclusions and Recommendations

6.1 Conclusions

In this work an anisotropic Lennard-Jones type molecular interaction potential, the so-called *Zewdie-Corner* potential [11], was used in conjuction with the Metropolis Monte Carlo (MMC) method to simulate liquid crystal phases and liquid crystal/nanoparticle mixtures. This molecular coarse-grained interaction potential has significant advantages compared to past approaches in that it expresses range (length scale) and strength (energy scale) parameters as expansions of an appropriate orthogonal basis set of functions in order to capture mesogen-mesogen and mesogen-nanoparticle interactions. The overall conclusions are:

1. MMC simulations showed promising results for both pure nematic and nematic/ nanoparticle mixtures with both orientational order (nematics), and in some cases, translational order (smectics).

2. The usage of simulation conditions from past published research was found to result in unphysical pressure values which, in turn, explained simulation results of seemingly second order nematic transitions and linear variation of density with respect to temperature.

3. Increasing the number density of nanoparticles in LC/nanoparticle mixtures resulted in an overall decrease in orientational order throughout the domain at higher nanoparticle number fractions, as expected. For a narrow range of temperatures and number

fractions the presence of nanoparticles seems to have stabilized nematic ordering due to micro phase separation and formation of well-ordered clusters of mesogens.

4. Finite size effects seemed to be difficult to avoid for simulation domains with computationally feasible numbers of molecules, for example, with a domain with $N = 3125$ finite size effects where still present, to a small degree, in calculations of the nematic order parameter s.

6.2 Recommendations

1. Given the difficulties in identifying LC phases and transitions from simulation data, future work should implement additional methods for quantifying LC order, specifically smectic order, and the presence of phase transitions. Implementing the calculation of structure factors as in [111] would be one beneficial approach towards distinguishing between smectic and nematic phases.

2. In order to accurately capture translational ordering, allowing the simulation domain scale and shape (e.g. cubic to parallelepiped) to change should be implemented, but if nematic phases are of interest where positional order exists, this is not important.

3. The properties of LC/nanoparticle mixtures is an area of current interest; many experimental results could be better understood through the usage of the presented method in the simulation of several experimentally observed phenomena:

   (a) For LC/nanoparticle mixtures with larger nanoparticles ($>$ 10nm), simulation studies could be conducted with preferred homeotropic alignment of the mesogenic molecules at the interface with the nanoparticles. This scenario has been reported in recent experimental studies [25, 26, 27].

   (b) Performing simulations with nanoparticle diameters on the order of the mesogen length should also be considered. The effect of varying nanoparticle diameter on phase separation would then be studied, similar to the work in [76, 77] and [32, 33].

   (c) Nanoparticle shape should also be varied; in some experimental studies cubic and polyhedron shapes have been used [29, 34, 35, 36].

4. Finally, optimization and acceleration of the developed code would enable simulation of larger domains and shorter simulation times:

(a) Implementation of a combined Cell and Verlet list [67] neighbour solver would significantly decrease the computational expense involved in tracking particle neighbours and computing the interaction energy. Alternatively, linked lists may be used instead, since in [85] it is claimed that this method is better suited for larger domains than the Verlet list algorithm.

(b) Optimization of the evaluation of Zewdie-Corner pairwise potential is another area that would benefit from significant optimization, especially given the likelihood of including higher order terms in future work. Complex high-order expressions can be pre-tabulated and evaluated in constant time as is done with special functions in math libraries.

(c) The use of NPT simulations, while needed to determine correct volumes initially, is not needed for repeated simulations using the same conditions. Once the thermodynamically stable density is known, less computationally complex NVT simulations could be used to speed up computation.

Appendices

Appendix A

Approximating the Number of Mesogenic Molecules in a Pixel of a Liquid Crystal Display

In order to approximate the number of mesogenic molecules in a pixel, it is necessary to know the density of mesogens and the volume of the pixel.

An example of a typical mesogen is E7, a biphenyl with the chemical formula $C_{12}H_{10}$.

$$\rho_{E7} = 1.04\ g/cm^3$$
$$M_{E7} = 154.21\ g/mol$$
$$\frac{\rho_{E7}}{M_{E7}} = 6.74 \times 10^{-3}\ \frac{mol}{cm^3}$$
$$\frac{\rho_{E7}}{M_{E7}} \times N_A = 6.74 \times 10^{-3}\ \frac{mol}{cm^3} \times 6.02 \times 10^{23}\ \frac{molecules}{mol} = 4.06 \times 10^{21}\ \frac{molecules}{cm^3}$$

Now, assuming a pixel density of 220 pixels per inch (which was almost the state-of-the-art for a laptop display in spring 2014) and display thickness of 5 μm:

$$\left(\frac{220\ ppi}{2.54\ cm/inch}\right)^2 \times 5 \times 10^{-4}\ cm = 1.50 \times 10^7\ \frac{pixels}{cm^3}$$

Therefore,

$$\frac{4.06 \times 10^{21}\ \frac{molecules}{cm^3}}{1.50 \times 10^7\ \frac{pixels}{cm^3}} = 2.71 \times 10^{14}\ \frac{molecules}{pixel}$$

Obviously, the obtained result is a very large number approximately equal to 100 trillion. Thus, it becomes apparent why it is not feasible to use coarse-grained Molecular Dynamics or Monte Carlo simulations to simulate domains with as many mesogens as there would be in a real pixel. Consequently, continuum models continue to be useful for industrial applications. However, while these statements are true in the year 2015 they may not remain such forever, considering the enormous increase in scientific knowledge even in the last 100 years.

Appendix B

Reduced Units for Pressure and Temperature Employed in Some Scientific Publications

Conversion to reduced ("dimensionless") values for pressure and temperature are given in literature [82, 85, 54, 108] as:

$$P^* = \frac{P\sigma_0^3}{\epsilon_0} \tag{B.1}$$

$$T^* = \frac{k_B T}{\epsilon_0} \tag{B.2}$$

where ϵ_0 is the energy scaling unit, σ_0 is the length scaling unit and k_B is the Boltzmann constant ($1.3806 \times 10^{-23}\ \frac{J}{K}$).

Note that in [91] there appears to be a typo in the formula for conversion to reduced pressure (equation B.1 in this thesis), since the factor multiplying P (i.e. $\sigma_0^3\epsilon_0^{-1}$) is incorrectly written in its inverted form in that published work.

Values accepted as reasonable for ϵ_0 and σ_0 for low molecular mass mesogens are on the order of $10^{-21}\ J$ and $10^{-10}\ m$, respectively. In [82], $\epsilon_0 = 1.85\times10^{-21}\ J$ and $\sigma_0 = 5\times10^{-10}\ m$. In [91], $\epsilon_0 = 1.4\times10^{-21}\ J$ and $\sigma_0 = 5\times10^{-10}\ m$. It is interesting to note that $5\times10^{-10}\ m$ is the diameter of a benzene ring. Since calamitic mesogens usually have at least two benzene rings as their rigid cores, using this value for σ_0 is reasonable - it would be the diameter of the rod-like shape that approximates coarse-grained mesogens.

In [82] $P^* = 8$ and $T^* \in [1.5, 3.5]$; these values for reduced pressure and temperature translate to

$$P = \frac{P^*\epsilon_0}{\sigma_0^3} = \frac{8 \times 1.85 \times 10^{-21}\ J}{(5 \times 10^{-10}\ m)^3} \times \frac{1\ atm}{101325\ Pa} = 1168.5\ atm \tag{B.3}$$

$$T(T^* = 1.5) = \frac{T^*\epsilon_0}{k_B} = \frac{1.5 \times 1.85 \times 10^{-21}\ J}{1.3806 \times 10^{-23}\ \frac{J}{K}} = 201.00\ K = -72.15\ ^\circ C \tag{B.4}$$

$$T(T^* = 3.5) = \frac{T^*\epsilon_0}{k_B} = \frac{3.5 \times 1.85 \times 10^{-21}\ J}{1.3806 \times 10^{-23}\ \frac{J}{K}} = 469.00\ K = 195.85\ ^\circ C \tag{B.5}$$

The mesogens studied in [82] are tapered rod-like particles. Therefore, we can compare the temperatures used in [82] for investigating the existence of liquid crystal phases to those reported for real calamitic mesogens in textbooks such as [1]. The temperature range of the simulation, though apparently quite wide (as shown by equations B.4 and B.5), is reasonable. The upper bound for temperature ($T^* = 3.5,\ T = 195.85\ ^\circ C$) is on the same order of magnitude as the higher values reported for liquid crystal-isotropic transition temperature of various calamitic mesogens (see chapter 3, section 3.2 of [1]), and the lower bound ($T^* = 1.5,\ T = -72.15\ ^\circ C$) is below the minimum temperature at which nematic phases exist for different calamitic mesogens (which can be as low as $-25\ ^\circ C$ - see, for instance, page 56, Figure 3.8 in [1]). However, $P^* = 8$ in reduced units corresponding to $P = 1168.5\ atm$ in real units is a very high value that does not appear physical.

In [91], reduced pressure P^* was also set to 8 and reduced temperature T^* range was $[2.6, 3.6]$. Using the energy and length scaling units given in this paper, we can obtain the following physical values for pressure and temperature:

$$P = \frac{P^*\epsilon_0}{\sigma_0^3} = \frac{8 \times 1.4 \times 10^{-21}\ J}{(5 \times 10^{-10}\ m)^3} \times \frac{1\ atm}{101325\ Pa} = 884.3\ atm \tag{B.6}$$

$$T(T^* = 2.6) = \frac{T^*\epsilon_0}{k_B} = \frac{2.6 \times 1.4 \times 10^{-21}\ J}{1.3806 \times 10^{-23}\ \frac{J}{K}} = 263.65\ K = -9.50\ ^\circ C \tag{B.7}$$

$$T(T^* = 3.6) = \frac{T^*\epsilon_0}{k_B} = \frac{3.6 \times 1.4 \times 10^{-21}\ J}{1.3806 \times 10^{-23}\ \frac{J}{K}} = 365.06\ K = 91.91\ ^\circ C \tag{B.8}$$

Based on the argument above, the reduced temperature range is fairly reasonable, but once again the chosen value for reduced pressure is quite high compared to physical values. Hence, for the simulations conducted in this thesis the value for reduced pressure was chosen such that when translated into physical units using the appropriate scaling factors (described in section 4.2.1) it would be equivalent to 1 *bar* (approximately 1 *atm*).

Appendix C

Plots of Other Potentials Employed in Section 4.2.2

Attached are the plots complementary to section 4.2.2 and figure 4.3. The plots depict potential energy curves between cylinder-like particles with $\epsilon_{\parallel}/\epsilon_{\perp}$ ratios between 1.00 and 1.75, inclusive, with a step of 0.25. Note the simultaneous increase in the stability of "side-by-side" configurations (red curves) and "head-to-tail" configurations (blue curves) upon the increase in $\epsilon_{\parallel}/\epsilon_{\perp}$ ratios.

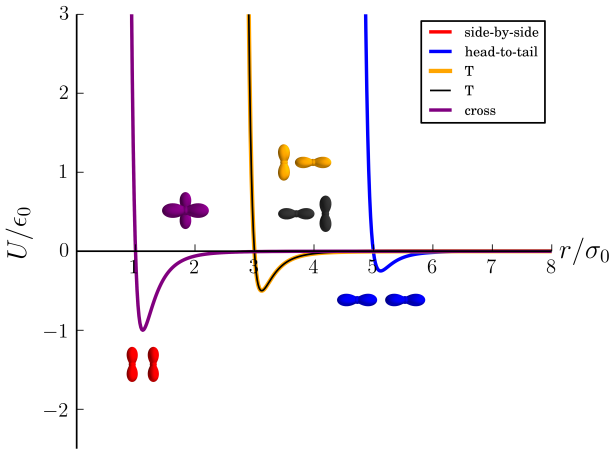

Figure C.1: Cylinder-cylinder potential energy curves with $\epsilon_\parallel/\epsilon_\perp = 1.00$, $L_h = 2.5$ and $r_c = 0.5$. Note that the "side-by-side" (red) and "cross" (purple) curves overlap completely.

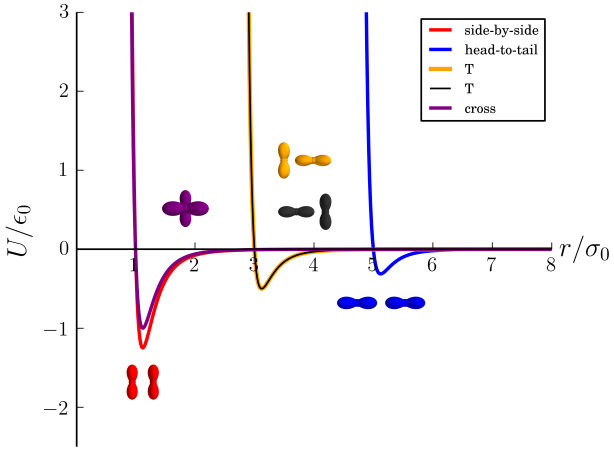

Figure C.2: Cylinder-cylinder potential energy curves with $\epsilon_\parallel/\epsilon_\perp = 1.25$, $L_h = 2.5$ and $r_c = 0.5$. Note the simultaneous change in the stability of "side-by-side" (red) and "head-to-tail" (blue) configurations upon the increase of $\epsilon_\parallel/\epsilon_\perp$ as compared to figure C.1.

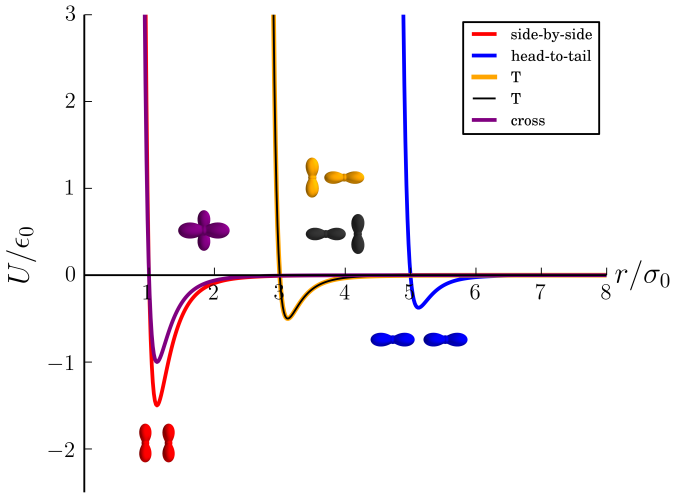

Figure C.3: Cylinder-cylinder potential energy curves with $\epsilon_\parallel/\epsilon_\perp = 1.50$, $L_h = 2.5$ and $r_c = 0.5$

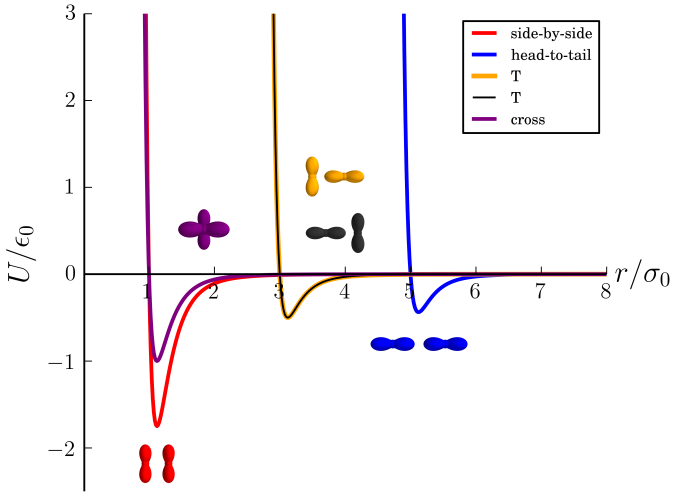

Figure C.4: Cylinder-cylinder potential energy curves with $\epsilon_\parallel/\epsilon_\perp = 1.75$, $L_h = 2.5$ and $r_c = 0.5$

References

[1] Peter J. Collings and Michael Hird. *Introduction to Liquid Crystals: Chemistry and Physics*. Taylor & Francis, 1997.

[2] H. Finkelmann, A. Greve, and M. Warner. The elastic anisotropy of nematic elastomers. *The European Physical Journal E - Soft Matter*, 5(3):281–293, 2001.

[3] Mark Richard Wilson. Progress in computer simulations of liquid crystals. *International Reviews in Physical Chemistry*, 24(3-4):421–455, July 2005.

[4] J. W. G. Goodby. *Ferroelectric liquid crystals: principles, properties, and applications*. Taylor & Francis, 1991.

[5] Francesca Serra, Marco Buscaglia, and Tommaso Bellini. The emergence of memory in liquid crystals. *Materials Today*, 14(10):488 – 494, 2011.

[6] S. Kralj and S. Žumer. Saddle-splay elasticity of nematic structures confined to a cylindrical capillary. *Physical Review E*, 51(1):366–379, January 1995.

[7] P.G. de Gennes and J Prost. *The Physics of Liquid Crystals*. Oxford University Press, New York, second edition, 1995.

[8] Jan P. F. Lagerwall and Giusy Scalia. A new era for liquid crystal research : Applications of liquid crystals in soft matter nano- , bio- and microtechnology. *Current Applied Physics*, 12(6):1387–1412, 2012.

[9] Daan Frenkel and Berend Smit. *Understanding Molecular Simulation From Algorithms to Applications*. Academic Press, San Diego, California, 2nd edition, 2002.

[10] Claudio Zannoni. Molecular design and computer simulations of novel mesophases. *Journal of Materials Chemistry*, 11:2637–2646, 2001.

[11] H. Zewdie. Computer simulation studies of liquid crystals: A new corner potential for cylindrically symmetric particles. *The Journal of Chemical Physics*, 108:2117, 1998.

[12] J. W. Goodby. Optical Activity and Ferroelectricity in Liquid Crystals. *Science*, 231(4736):350–355, 1986.

[13] Takashi Kato. Self-Assembly of Phase-Segregated Liquid Crystal Structures. *Science*, 295(5564):2414–2418, 2002.

[14] Takashi Kato, Norihiro Mizoshita, and Kenji Kishimoto. Functional liquid-crystalline assemblies: self-organized soft materials. *Angewandte Chemie (International ed. in English)*, 45(1):38–68, December 2005.

[15] C. M. Care and D. J. Cleaver. Computer simulation of liquid crystals. *Reports on Progress in Physics*, 68(11):2665–2700, November 2005.

[16] Alejandro D. Rey and Edtson E. Herrera-Valencia. Liquid Crystal Models of Biological Materials and Silk Spinning. *Biopolymers*, 97(6):374–396, 2011.

[17] Mirko Cestari. *Atomistic modelling of liquid crystal materials properties: a theoretical and computational methodology*. PhD thesis, University of Padova, 2008.

[18] Valery Petrovich Shibaev. Liquid Crystals - the "Centaurs" of Nature. *Priroda*, 1, 2012.

[19] Claudio Zannoni. Distribution Functions and Order Parameters. In *The Molecular Physics of Liquid Crystals*, pages 51–83. 1979.

[20] Dong Chen, Jan H. Porada, Justin B. Hooper, Arthur Klittnick, Yongqiang Shen, Michael R. Tuchband, Eva Korblova, Dmitry Bedrov, David M. Walba, Matthew A. Glaser, Joseph E. Maclennan, and Noel A. Clark. Chiral heliconical ground state of nanoscale pitch in a nematic liquid crystal of achiral molecular dimers. *Proceedings of the National Academy of Sciences of the United States of America*, 110(40):15931–15936, October 2013.

[21] Claudine Noël and Patrick Navard. Liquid Crystal Polymers. *Progress in Polymer Science*, 16:55–110, 1991.

[22] J. W. Goodby. Mesogenic molecular crystalline materials. *Current Opinion in Solid State and Materials Science*, 4(4):361–368, August 1999.

[23] A. G. Vanakaras, M. A. Bates, and D. J. Photinos. Theory and simulation of biaxial nematic and orthogonal smectic phases formed by mixtures of board-like molecules. *Physical Chemistry Chemical Physics*, 5:3700–3706, July 2003.

[24] Roberto Berardi, Luca Muccioli, and Claudio Zannoni. Field response and switching times in biaxial nematics. *The Journal of Chemical Physics*, 128(2):024905, January 2008.

[25] M. Jamil, Farzana Ahmad, J. T. Rhee, and Y. J. Jeon. Nanoparticle-doped polymer-dispersed liquid crystal display. *Current Science*, 101(12):1544–1552, December 2011.

[26] Javad Mirzaei, Martin Urbanski, Heinz-S. Kitzerow, and Torsten Hegmann. Synthesis of Liquid Crystal Silane-Functionalized Gold Nanoparticles and Their Effects on the Optical and Electro-Optic Properties of a Structurally Related Nematic Liquid Crystal. *ChemPhysChem*, 15:1381–1394, 2014.

[27] Martin Urbanski, Javad Mirzaei, Torsten Hegmann, and Heinz-S. Kitzerow. Nanoparticle Doping in Nematic Liquid Crystals: Distinction between Surface and Bulk Effects by Numerical Simulations. *ChemPhysChem*, 15:1395–1404, 2014.

[28] Guadalupe Jiménez-Serratos, Carlos Avendaño, Alejandro Gil-Villegas, and Enrique González-Tovar. Computer simulation of charged hard spherocylinders at low temperatures. *Molecular Physics*, 109(1):27–36, January 2011.

[29] Marjan Krasna, Matej Cvetko, and Milan Ambrozic. Symmetry breaking and structure of a mixture of nematic liquid crystals and anisotropic nanoparticles. *Beilstein Journal of Organic Chemistry*, 6(74), July 2010.

[30] Elisa Spinozzi and Alessandro Ciattoni. Ultrathin optical switch based on a liquid crystal/silver nanoparticles mixture as a tunable indefinite medium. *Optical Materials Express*, 1(4):732–741, July 2011.

[31] A. Sinyagin, A. Belov, and N. Kotov. Monte Carlo simulation of linear aggregate formation from CdTe nanoparticles. *Modelling and Simulation in Materials Science and Engineering*, 13:389–399, March 2005.

[32] Bertrand Donnio, Patricia García-Vázquez, Jean-Louis Gallani, Daniel Guillon, and Emmanuel Terazzi. Dendronized Ferromagnetic Gold Nanoparticles Self-Organized in a Thermotropic Cubic Phase. *Advanced Materials*, 19:3534–3539, 2007.

[33] Lucy A. Holt, Richard J. Bushby, Stephen D. Evans, Andrew Burgess, and Gordon Seeley. A 10^6-fold enhancement in the conductivity of a discotic liquid crystal doped with only 1 % (w / w) gold nanoparticles. *Journal of Applied Physics*, 103(6):063712:1–7, 2008.

[34] Vlad Popa-Nita, Matej Cvetko, and Samo Kralj. *Electronic Properties of Carbon Nanotubes*, chapter Liquid Crystal - Anisotropic Nanoparticles Mixtures, pages 645–664. InTech, 1 edition, July 2011. Available from: http://www.intechopen.com/books/electronic-properties-of-carbon-nanotubes/liquid- crystal-anisotropic-nanoparticles-mixtures.

[35] Hang Hu, Linda Reven, and Alejandro Rey. First-Principles Density Functional Theory (DFT) Study of Gold Nanorod and Its Interaction with Alkanethiol Ligands. *The Journal of Physical Chemistry*, 117:12625–12631, October 2013.

[36] Héloïse Thérien-Aubin, Ariella Lukach, Natalie Pitch, and Eugenia Kumacheva. Coassembly of Nanorods and Nanospheres in Suspensions and in Stratified Films. *Angewandte Chemie International Edition*, 54:5618–5622, 2015.

[37] Amit Choudhary, Gautam Singh, and Ashok M. Biradar. Advances in gold nanoparticle-liquid crystal composities. *Nanoscale*, 6:7743–7756, 2014.

[38] Claudio Zannoni. Computer Simulations. In *The Molecular Physics of Liquid Crystals*, pages 191–220. 1979.

[39] Michael P. Allen, Mark A. Warren, Mark Richard Wilson, Alain Sauron, and William Smith. Molecular dynamics calculation of elastic constants in Gay-Berne nematic liquid crystals. *The Journal of Chemical Physics*, 105(7):2850–8, 1996.

[40] C. Chiccoli, S. Guzzetti, P. Pasini, and Claudio Zannoni. Computer Simulations of Nematic Displays. *Molecular Crystals and Liquid Crystals*, 360:119–129, 2001.

[41] Mojca Čepič and Boštjan Žekš. Orihara-Ishibashi Continuous Model of Antiferroelectric Liquid Crystals. *Ferroelectrics*, 349(1):21–32, April 2007.

[42] Gaia Valeria Paolini, Giovanni Ciccotti, and Mauro Ferrario. Simulation of site-site soft-core liquid crystal models. *Mol. Phys.*, 80(2):297–312, 1993.

[43] ZhanWei Li, YuHua Liu, YingTao Liu, and ZhongYuan Lu. A single-site anisotropic soft-core model for the study of phase behavior of soft rodlike particles. *Science China*, 54(9):1474–1483, September 2011.

[44] S. L. Price and A. J. Stone. A six-site intermolecular potential scheme for the azabenzene molecules, derived by crystal structure analysis. *Molecular Physics*, 51:569–583, 1984.

[45] Hiroo Fukunaga, Jun-ichi Takimoto, and Masao. Doi. Molecular dynamics simulation study on the phase behavior of the Gay-Berne model with a terminal dipole and a flexible tail.allen. *J. Chem. Phys.*, 120:7792–7800, 2004.

[46] Robert Bukowski, Krzysztof Szalewicz, Gerrit C Groenenboom, and Ad van der Avoird. Predictions of the properties of water from first principles. *Science (New York, N.Y.)*, 315(5816):1249–52, March 2007.

[47] Axel D. Becke. Perspective: Fifty years of density-functional theory in chemical physics. *The Journal of Chemical Physics*, 140(18):18A301, May 2014.

[48] G. Jacucci. Monte Carlo calculation of the free energy difference between hard and soft core diatomic liquids. *Molecular Physics*, 40(4):1005–1009, 1980.

[49] F. Barmes, M. Ricci, Claudio Zannoni, and D. Cleaver. Computer simulations of hard pear-shaped particles. *Physical Review E*, 68(2):021708, August 2003.

[50] Luca Muccioli and Claudio Zannoni. A deformable Gay-Berne model for the simulation of liquid crystals and soft materials. *Chemical Physics Letters*, 423(1-3):1–6, May 2006.

[51] Mark Richard Wilson. Molecular simulation of liquid crystals: progress towards a better understanding of bulk structure and the prediction of material properties. *Chemical Society Reviews*, 36:1881–1888, 2007.

[52] P. A. Lebwohl and G. Lasher. Nematic-Liquid-Crystal Order - A Monte Carlo Calculation. *Physical Review A*, 6(1):426–9, 1972.

[53] P. A. Lebwohl and G. Lasher. Nematic-Liquid-Crystal Order - a Monte Carlo Calculation (errata). *Physical Review A*, 7(6):2222, 1973.

[54] Silvia Orlandi, Roberto Berardi, Joachim Steltzer, and Claudio Zannoni. A Monte Carlo study of the mesophases formed by polar bent-shaped molecules. *The Journal of Chemical Physics*, 124:124907, 2006.

[55] J. E. Lennard-Jones. On the Determination of Molecular Fields . II. From the Equation of State of a Gas. *Proceedings of the Royal Society of London . Series A, Containing Papers of a Mathematical and Physical Character*, 106(738):463–477, 1924.

[56] J. E. Lennard-Jones. On the Forces between Atoms and Ions. *Proceedings of the Royal Society of London. Series A, Containing Papers of a Mathematical and Physical Character1*, 109(752):584–597, 1925.

[57] J. E. Lennard-Jones and P. A. Taylor. Some Theoretical Calculations of the Physical Properties of Certain Crystals. *Proceedings of the Royal Society of London. Series A, Containing Papers of a Mathematical and Physical Character*, 109(751):476–508, 1925.

[58] Rabia Naeem. Lennard-Jones Potential, 2013. UC Davis STEMWiki Hyperlibrary - collaborative Open Access textbook environment. Available from http://chemwiki.ucdavis.edu.

[59] J. Corner. The Second Virial Coefficient of a Gas of Non-Spherical Molecules. *Proceedings of the Royal Society of London. Series A, Mathematical and Physical Sciences*, 192(1029):275–292, 1948.

[60] J. G. Gay and B. J. Berne. Modification of the overlap potential to mimic a linear sitesite potential. *The Journal of Chemical Physics*, 74(6):3316–9, 1981.

[61] Leonid Paramonov and Sophia N. Yaliraki. The directional contact distance of two ellipsoids: coarse-grained potentials for anisotropic interactions. *The Journal of Chemical Physics*, 123(19):194111, November 2005.

[62] Alejandro Cuetos and Bruno Martinez-Haya. Columnar phases of discotic spherocylinders. *The Journal of Chemical Physics*, 129:214706, 2008.

[63] Nicholas Metropolis, Arianna W. Rosenbluth, Marshall N. Rosenbluth, Augusta H. Teller, and Edward Teller. Equation of State Calculations by Fast Computing Machines. *The Journal of Chemical Physics*, 21(6):1087–1092, 1953.

[64] Daniel V. Schroeder. *An Introduction to Thermal Physics*. Addison-Wesley, 2000.

[65] M. A. Bates and G. R. Luckhurst. Biaxial nematics: computer simulation studies of a generic rod-disc dimer model. *Physical Chemistry Chemical Physics*, 7:2821–2829, June 2005.

[66] Claire Rist and Alexandre Faure. A Monte Carlo error estimator for the expansion of rigid-rotor potential energy surfaces. *Journal of Mathematical Chemistry*, 50(3):588–601, May 2011.

[67] Daan Frenkel and Berend Smit. *Understanding Molecular Simulation From Algorithms to Applications*. Academic Press, San Diego, California, 2nd edition, 2002.

[68] W. W. Wood. Monte Carlo Calculations for Hard Disks in the Isothermal-Isobaric Ensemble. *The Journal of Chemical Physics*, 48(1):415–434, January 1968.

[69] I. R. McDonald. Monte Carlo Calculations for One- and Two-Component Fluids in the Isothermal-Isobaric Ensemble. *Chemical Physics Letters*, 3(4):241–243, April 1969.

[70] I. R. McDonald. NpT-ensemble Monte Carlo calculations for binary liquid mixtures. *Molecular Physics*, 23(1):41–58, 1972.

[71] S. L. Price and A. J. Stone. Evaluation of anisotropic model intermolecular pair potentials using an ab initio SCF-CI surface. *Molecular Physics*, 40(4):805–822, 1980.

[72] S. L. Price and A. J. Stone. The anisotropy of the Cl2-Cl2 pair potential as shown by the crystal structure: Evidence for intermolecular bonding or lone pair effects? *Molecular Physics*, 47(6):1457–1470, 1982.

[73] S. L. Price, A. J. Stone, and M. Alderton. Explicit formulae for the electrostatic energy, forces and torques between a pair of molecules of arbitrary symmetry. *Molecular Physics*, 52(4):987–1001, 1984.

[74] T. Kihara. Convex Molecules in Gaseous and Crystalline States. *Advances in Chemical Physics*, 5:147–188, 1963.

[75] John D. Weeks, David Chandler, and Hans C. Andersen. Role of Repulsive Forces in Determining the Equilibrium Structure of Simple Liquids. *The Journal of Chemical Physics*, 54(12):5237–5247, June 1971.

[76] Pu Tian, Grant D. Smith, and Matthew Glaser. Molecular dynamics simulations studies of nanoparticles in an isotropic liquid crystal matrix: Single particle behavior and pairwise interactions. *The Journal of Chemical Physics*, 124:161101, April 2006.

[77] Pu Tian and Grant D. Smith. Molecular dynamics simulations of nanoparticles in dense isotropic nematogens: The role of matrix-induced long-range repulsive interactions. *The Journal of Chemical Physics*, 124:184701, May 2006.

[78] Alejandro Cuetos, Bruno Martinez-Haya, S. Lago, and L. F. Rull. Liquid crystal behavior of the Kihara fluid. *Physical Review E: Statistical, Nonlinear, and Soft Matter Physics*, 68:011704, July 2003.

[79] Alejandro Cuetos, Bruno Martinez-Haya, S. Lago, and L. F. Rull. Parsons-Lee and Monte Carlo Study of Soft Repulsive Nematogens. *Journal of Physical Chemistry B*, 109:13729–13736, Juny 2005.

[80] Mauricio Piedrahita, Alejandro Cuetos, and Bruno Martinez-Haya. Transport of spherical colloids in layered phases of binary mixtures with rod-like particles. *Soft Matter*, 11:3432–3440, March 2015.

[81] H. Zewdie. Computer-simulation studies of diskotic liquid crystals. *Physical Review E*, 57(2):1793–1805, February 1998.

[82] Roberto Berardi, Matteo Ricci, and Claudio Zannoni. Ferroelectric Nematic and Smectic Liquid Crystals from Tapered Molecules. *ChemPhysChem*, (7):443–447, 2001.

[83] Roberto Berardi, Matteo Ricci, and Claudio Zannoni. Ferroelectric and Structured Phases from Polar Tapered Mesogens. *Ferroelectrics*, 309(1):3–12, January 2004.

[84] A. J. Stone. The description of bimolecular potentials, forces and torques: the S and V function expansions. *Molecular Physics*, 36(1):241–256, 1978.

[85] Giorgio Cinacchi and Alessandro Tani. Computer simulations of pure and mixed systems of disklike particles interacting with the S-function Corner potential. *The Journal of Chemical Physics*, 117(24):11388–11395, December 2002.

[86] Giorgio Cinacchi, Giovanni La Penna, and Angelo Perico. Anisotropic Internucleosome Interactions and Geometrical Constraints in the Organization of Chromatin. *Macromolecules*, 40(26):9603–9613, December 2007.

[87] R. Memmer. Liquid crystal phases of achiral banana-shaped molecules: a computer simulation study. *Liquid Crystals*, 29(4):483–496, 2002.

[88] Roberto Berardi, C. Fava, and Claudio Zannoni. A generalized Gay-Berne intermolecular potential for biaxial particles. *Chemical Physics Letters*, 236(4):462–468, 1995.

[89] Roberto Berardi and Claudio Zannoni. Biaxial Discotic Gay-Berne Mesogens and Biaxial Nematics. *Mol. Cryst. Liq. Cryst.*, 396:177–186, 2003.

[90] Giorgio Cinacchi. Ordering of biaxial solutes in a smectic solvent. *Chemical Physics Letters*, 416(4-6):238–245, December 2005.

[91] Lara Querciagrossa, Matteo Ricci, Roberto Berardi, and Claudio Zannoni. Mesogen polarity effects on biaxial nematics. Centrally located dipoles. *Physical Chemistry Chemical Physics*, 15:19065–19072, 2013.

[92] R. K. Shukla, X. Feng, S. Umadevi, T. Hegmann, and W. Haase. Influence of different amount of functionalized bulky gold nanorods dopant on the electrooptical, dielectric and optical properties of the FLC host. *Chemical Physics Letters*, 599:80–85, April 2014.

[93] Mitya Reznikov, Anshul Sharma, and Torsten Hegmann. Ink-Jet Printed Nanoparticle Alignment Layers: Easy Design and Fabrication of Patterned Alignment Layers for Nematic Liquid Crystals. *Particle and Particle Systems Characterization*, 31:257–265, 2014.

[94] Sarmenio Saliba, Christophe Mingotaud, Myrtil L. Kahn, and Jean-Daniel Marty. Liquid crystalline thermotropic and lyotropic nanohybrids. *Nanoscale*, 5:6641–6661, 2013.

[95] P. Oswald, J. Milette, S. Relaix, L. Reven, A. Dequidt, and L. Lejcek. Alloy hardedning of a smectic A liquid crystal doped with gold nanoparticles. *EPL (Europhysics Letters)*, 103:46004, August 2013.

[96] R. Pratibha, W. Park, and I. I. Smalyukh. Colloidal gold nanosphere dispersions in smectic liquid crystals and thin nanoparticle- decorated smectic films. *Journal of Applied Physics*, 107(6):063511:1–6, 2010.

[97] S. Umadevi, H. C. Lee, V. Ganesh, X. Feng, and T. Hegmann. A versatile, one-pot synthesis of gold nanostars with long, well-defined thorns using a lyotropic liquid crystal template. *Liquid Crystals*, 41(3):265–276, 2014.

[98] Jonathan Milette, Violeta Toader, Linda Reven, and R. Bruce Lennox. Tuning the miscibility of gold nanoparticles dispersed in liquid crystals via the thiol-for-DMAP reaction. *Journal of Materials Chemistry*, 21:9043–9050, May 2011.

[99] Jonathan Milette, Stephen J. Cowling, Violeta Toader, Cyrille Lavigne, Isabel M. Saez, R. Bruce Lennox, John W. Goodby, and Linda Reven. Reversible long range network formation in gold nanoparticle - nematic liquid crystal composites. *Soft Matter*, 8:173–179, 2012.

[100] Jonathan Milette, Sabrina Relaix, Cyrille Lavigne, Violeta Toader, Stephen J. Cowling, Isabel Saez, R. Bruce Lennox, John W. Goodby, and Linda Reven. Reversible long-range patterning of gold nanoparticles by smectic liquid crystals. *Soft Matter*, 8:6593–6598, 2012.

[101] Jonathan Milette, Violeta Toader, Ezequiel R. Soulé, R. Bruce Lennox, Alejandro D. Rey, and Linda Reven. A Molecular and Thermodynamic View of the Assembly of Gold Nanoparticles in Nematic Liquid Crystal. *Langmuir*, 29:1258–1263, January 2013.

[102] Satoru Sano, Tomohiro Miyama, Kohki Takatoh, and Shunsuke Kobayashi. Enhancement of the characteristics of LCDs by doping nanoparticles: reduction of the operating voltage, viscosity, and response times. *Proceedings of SPIE-The International Society for Optical Engineering*, page 613501, February 2006.

[103] Ezequiel R. Soulé, Linda Reven, and Alejandro D. Rey. Thermodynamic Modelling of Phase Equilibrium in Nanoparticles - Nematic Liquid Crystals Composites. *Molecular Crystals and Liquid Crystals*, 553(1):118–126, 2012.

[104] Ezequiel R. Soulé, Jonathan Milette, Linda Reven, and Alejandro D. Rey. Phase equilibrium and structure formation in gold nanoparticles-nematic liquid crystal composites: experiments and theory. *Soft Matter*, 8:2860–2866, 2012.

[105] Denis Andrienko, Guido Germano, and Michael P. Allen. Computer simulation of topological defects around a colloidal particle or droplet dispersed in a nematic host. *Physical Review E: Statistical, Nonlinear, and Soft Matter Physics*, 63:041701, March 2001.

[106] Evelina B. Kim, Orlando Guzmán, Sylvain Grollau, Nicholas L. Abbott, and Juan J. de Pablo. Interactions between spherical colloids mediated by a liquid crystal: A molecular simulation and mesoscale study. *The Journal of Chemical Physics*, 121(4):1949–1961, July 2004.

[107] Pu Tian, Grant D. Smith, and Matthew Glaser. Erratum: "Molecular dynamics simulations studies of nanoparticles in an isotropic liquid crystal matrix: Single particle behavior and pairwise interactions" [J. Chem. Phys.124, 161101 (2006)] and "Molecular dynamics simulations of nanoparticles in dense isotropic nematogens: The role of matrix-induced long-range repulsive interactions" [J. Chem. Phys.124, 184701 (2006)]. *The Journal of Chemical Physics*, 128:159901, April 2008.

[108] Jianqing Xu, Dmitry Bedrov, Grant D. Smith, and Matthew A. Glaser. Molecular dynamics simulation study of spherical nanoparticles in a nematogenic matrix: Anchoring, interactions and phase behavior. *Physical Review E*, 79:011704, January 2009.

[109] Alejandro Cuetos, Bruno Martinez-Haya, Santiago Lago, and Luis F. Rull. Use of Parsons-Lee and Onsager theories to predict nematic and demixing behavior in binary mixtures of hard rods and hard spheres. *Physical Review E: Statistical, Nonlinear, and Soft Matter Physics*, 75:061701, 2007.

[110] Stavros D. Peroukidis, Alexandros G. Vanakaras, and Demetri J. Photinos. Liquid crystalline phases and demixing in binary mixtures of shape-anisometric colloids. *Journal of Materials Chemistry*, 20:10495–10502, 2010.

[111] Carlos Avendaño, Alejandro Gil-Villegas, and Enrique González-Tovar. A Monte Carlo simulation study of binary mixtures of charged hard spherocylinders and charged hard spheres. *Chemical Physics Letters*, pages 67–71, January 2009.